

379
N81d
no. 3938

NONLINEAR DYNAMICS OF SEMICONDUCTOR DEVICE CIRCUITS AND
CHARACTERIZATION OF DEEP ENERGY LEVELS IN HgCdTe
BY USING MAGNETO-OPTICAL SPECTROSCOPY

DISSERTATION

Presented to the Graduate Council of the
University of North Texas in Partial
Fulfillment of the Requirements
For the Degree of

DOCTOR OF PHILOSOPHY

By

Zhi Yu, B.S., M.S.,
Denton, Texas
May, 1994

379
N81d
no. 3938

NONLINEAR DYNAMICS OF SEMICONDUCTOR DEVICE CIRCUITS AND
CHARACTERIZATION OF DEEP ENERGY LEVELS IN HgCdTe
BY USING MAGNETO-OPTICAL SPECTROSCOPY

DISSERTATION

Presented to the Graduate Council of the
University of North Texas in Partial
Fulfillment of the Requirements
For the Degree of

DOCTOR OF PHILOSOPHY

By

Zhi Yu, B.S., M.S.,

Denton, Texas

May, 1994

Yu, Zhi, Nonlinear dynamics of semiconductor device circuits and characterization of deep energy levels in HgCdTe by using magneto-optical spectroscopy. Doctor of philosophy (Physics), May, 1994, 199pp., 9 tables, 73 illustrations, bibliography, 107 titles.

The nonlinear dynamics of three physical systems has been investigated. Diode resonator systems are experimentally shown to display a period doubling route to chaos, quasiperiodic states, periodic locking states, and Hopf bifurcation to chaos. Particularly, the transition from quasiperiodic states to chaos in line-coupled systems agrees well with the Curry-Yorke model. The *SPICE* program has been modified to give realistic models for the diode resonator systems.

A proportional feedback technique is applied to both single and line-coupled diode resonator systems. For single diode system, periodic orbits up to period 17 from a typical chaotic attractor are successfully stabilized. More interestingly, for the line-coupled diode systems not only are high periodic oscillations obtained easily, but for the first time quasiperiodic orbits are also stabilized.

Synchronization of chaos to a common orbit has been observed by weakly coupling two tunnel diode relaxation oscillators. In addition, the "frequency-locked entrainment" states of two chaotic attractors have also been observed when appropriate coupling is applied.

The dynamical Hall effect in n-InSb at liquid helium temperatures has been investigated. The experimental results are consistent with the theoretical predictions of Hüpper and Schöll. The stability of chaos in this system against an external AC-driven source has been investigated and compared to that for a simple driven oscillator. The induced transitions from chaos to periodicity by an AC-driven

source have been found in good agreement with a conjectured scaling law.

Resonant Impact Ionization (RII) Spectroscopy, a new technique for studying low concentrations of trap levels in narrow-gap semiconductors, has been employed to investigate Hg interstitials in both bulk and LPE samples of $\text{Hg}_{1-x}\text{Cd}_x\text{Te}$ with x value from 0.22 to 0.24. The RII spectroscopy of these samples, which are processed under different conditions to control the concentration of Hg interstitials, provide direct evidence that these Hg interstitials are responsible for the formation of trap levels near midgap.

TABLE OF CONTENTS

	Page
LIST OF TABLES	v
LIST OF ILLUSTRATIONS	vi
CHAPTERS	
1. INTRODUCTION	1
1.1 Nonlinear Dynamics of Electronic Circuits and Semiconductor n-InSb	
1.2 Characterization of Deep Energy Levels in HgCdTe by Magneto-Optical Spectroscopy	
2. EXPERIMENTAL AND NUMERICAL METHODS	14
2.1 Experimental Setup for Oscillatory Instability Studies of n-InSb in Low Temperature and High Magnetic Field	
2.2 Experimental Setup for Nonlinear Dynamical Study of Diode Resonator Systems	
2.3 Method to Stabilize Chaos in the Diode Resonator Systems.	
2.4 Magneto-Optical measurement techniques	
2.5 Numerical Integration Methods	
3. NONLINEAR DYNAMICS OF DRIVEN DIODE RESONATOR SYSTEMS AND SYNCHRONIZATION OF CHAOS IN COUPLED TUNNEL DIODE OSCILLATOR SYSTEMS	32

TABLE OF CONTENTS--Continued

3.1	Time Series Analysis Methods	
3.2	Simulation and Characterization of Nonlinear Dynamics in Driven Diode Resonator Systems	
3.3	Stabilization of Periodic and Quasiperiodic Oscillations in Diode Resonator Systems	
3.4	Synchronization of Chaos in Coupled Tunnel Diode Relaxation Oscillators	
4.	AUTONOMOUS AND EXTERNALLY DRIVEN PERIODIC AND CHAOTIC OSCILLATIONS IN n-InSb	123
4.1	Introduction	
4.2	Hüpper and Schöll Model	
4.3	Experimental Results and Discussion	
4.4	Conclusions	
5.	CHARACTERIZATION OF DEEP LEVELS IN HgCdTe BY RESONANT IMPACT-IONIZATION SPECTROSCOPY	145
5.1	Introduction	
5.2	Resonant Impact Ionization Mechanism	
5.3	Experimental Results and Discussion	
5.4	Conclusions and Final Remarks	
6.	CONCLUSIONS	190
	BIBLIOGRAPHY	193

LIST OF TABLES

Table	Page
2.1 Electrical Properties of Bulk HgCdTe Samples	19
3.1 Parameters for a Single Diode Resonator System	47
3.2 Lyapunov Exponents for a Single Diode Resonator System from Both Experimental Time Series and a Theoretical Simulated System	49
3.3 Parameters for a Line-Coupled Diode Resonator System	51
3.4 Lyapunov Exponents for a Line-Coupled Diode Resonator System from Both Experimental Time Series and a Theoretical Simulated System	55
3.5 Parameter Values of a Coupled Tunnel Diode Oscillator System .	64
5.1 Comparison of Experimental and Theoretical Magnetic Field Positions of RII Resonances for a $x \approx 0.22$ Bulk Sample	158
5.2 Comparison of Experimental and Theoretical Magnetic Field Positions of RII Resonances for an $x \approx 0.22$ Bulk Control and "Doped" Sample	159
5.3 Comparison of Experimental and Theoretical Magnetic Field Positions of RII Resonances for an $x \approx 0.22$ LPE Sample	160

LIST OF ILLUSTRATIONS

Figure	Page
2.1 Sample Configuration for the Autooscillatory Dynamic Study of n-InSb	26
2.2 Experimental Setup for the Autooscillatory Dynamic Study of n-InSb	27
2.3 Experimental Setup for the Diode Resonator Systems Experiments	28
2.4 Logic Diagram of the Stabilizer Circuit	29
2.5 Experimental Setup for the Magneto-Optical Study of HgCdTe .	31
3.1 Schematic Diagram of a Diode Model In <i>SPICE</i>	72
3.2 Circuit of a Single Diode Resonator System	73
3.3 Wave Form of Period-8 Oscillations in a Single Diode Resonator System	74
3.4 Wave Form of Chaotic Oscillations in a Single Diode Resonator System	75
3.5 Wave Form of Period-8 Oscillations for the Simulated Single Diode Resonator System	76
3.6 Wave Form of Chaotic Oscillations for the Simulated Single Diode Resonator System	77
3.7 Phase Portrait of Period-8 Oscillations in a Single Diode Resonator	78

LIST OF ILLUSTRATIONS--Continued

Figure	Page
3.8 Phase Portrait of Chaotic Oscillations in a Single Diode Resonator	79
3.9 Phase Plot of Period-8 Oscillations for the Simulated Single Diode Resonator System	80
3.10 Phase Plot of Chaos for the Simulated Single Diode Resonator System	81
3.11 Power Spectrum of Period-8 Oscillation for the Single Diode Resonator System	82
3.12 Power Spectrum of Chaos for the Single Diode Resonator System	83
3.13 Power Spectra of Period-8 Oscillations And Chaos for the Simulated Single Diode Resonator System	84
3.14 Bifurcation Diagram for the Single Diode Resonator System	85
3.15 Bifurcation Diagram for the Simulated Single Diode Resonator System	86
3.16 Enlarged Bifurcation Diagram for the Simulated Single Diode Resonator System	88
3.17 Enlarged Bifurcation Diagram for the Simulated Single Diode Resonator System	90
3.18 Circuit of the Line-Coupled Diode Resonator System	92
3.19 Phase Plots for Period-1 And Quasiperiodic Oscillations for the Line-Coupled Diode Resonator System	93
3.20 Sequence of Phase Plots from the Periodic State to the Quasiperiodic State, to Chaos	94

LIST OF ILLUSTRATIONS--Continued

Figure	Page
3.21 Power Spectrum of the Quasiperiodic State	95
3.22 Power Spectrum of Frequency Locked State	96
3.23 Power Spectrum of the Chaotic State	97
3.24 Bifurcation Diagram for the Simulated Line-Coupled Diode Resonator System (part 1)	98
3.25 Bifurcation Diagram for the Simulated Line-Coupled Diode Resonator System (part 2)	100
3.26 Poincaré Section of a Chaotic Attractor for a Simulated Four-Line- Coupled Diode Resonator System	102
3.27 System and Control Signals Before and after Stabilization . . .	103
3.28 Phase Plots of the Stabilization of a Chaotic Attractor	104
3.29 Power Spectrum for a Chaotic Attractor	105
3.30 Power Spectrum for a Stabilized Quasiperiodic Oscillation . .	106
3.31 Power Spectrum for a Stabilized Periodic Locked State	107
3.32 Poincaré Sections of a Four-Line-Coupled Diode Resonator System Before and after Stabilization	108
3.33 Power Spectra Before and after Stabilization for a Four-Line- Coupled System	110
3.34 Tunnel Diode Relaxation Oscillator Unit	112
3.35 Two Coupled Relaxation Oscillators	113
3.36 Synchronized Chaotic Voltages and Corresponding Power Spectra	114

LIST OF ILLUSTRATIONS--Continued

Figure	Page
3.37 Chaotic Voltages Before and After Coupling	115
3.38 Power Spectrum for the Synchronized Voltages	116
3.39 Synchronized Chaotic Voltages and Corresponding Power Spectrum	117
3.40 Digitized Voltages for Synchronized Chaos	118
3.41 Chaotic Voltages Entrained At $2/3$	120
3.42 Variation of the Principal Lyapunov Exponent with respect to Replacement Time	121
4.1 Parameter Phase Plot Showing Autooscillatory Instability and Static Regions	134
4.2 Comparison of Actual and Filtered Signals	135
4.3 Hall and Longitudinal Voltages for Period-1, Period-2, Period-4 and Chaotic Motions	137
4.4 Power Spectra for Period-1, Period-2, Period-4 and Chaotic Motions	139
4.5 Autocorrelation Functions for Period-1, Period-2, Period-4 and Chaotic Motions	140
4.6 Phase Portraits for Period-1, Period-2, Period-4 and Chaotic Motions	141
4.7 Plot of Driving Amplitude <i>versus</i> Driving Frequency for Simple Driven Oscillator	142

LIST OF ILLUSTRATIONS--Continued

Figure	Page
4.8 Plot of Critical Amplitude <i>versus</i> Driving Frequency	143
4.9 Plot of Critical Amplitude <i>versus</i> Largest Lyapunov Exponent	144
5.1 Wavelength Dependence of OPMA and RII Spectra for an $x \approx$ 0.24 Bulk Sample	163
5.2 Schematic Diagram of Electronic Transitions Showing Resonance Condition for RII	165
5.3 Photoconductive Response versus Magnetic Field for Control and "Doped" Bulk Sample	166
5.4 Wavelength Dependence of OPMA Photoconductive Response for an $x \approx 0.22$ Control Bulk Sample	168
5.5 Fan Chart of Transition Energies for an $x \approx 0.22$ Control Bulk Sample	170
5.6 Comparison of RII Spectra for Control and "Doped" Bulk Sample	172
5.7 The Same Spectra As Fig. 5.6 with Background Removed for Better Comparison	174
5.8 Comparison of TPMA Resonances for Control and "Doped" Samples	176
5.9 Wavelength Dependence of RII Spectra for an $x \approx 0.22$ LPE Sample	178
5.10 Wavelength Dependence of RII Spectra for the $x \approx 0.22$ LPE Sample	179

LIST OF ILLUSTRATIONS--Continued

Figure		Page
5.11	Fan Chart of OPMA and RII Resonance Positions for the $x \approx 0.22$ LPE Sample	180
5.12	Comparison of RII Spectra Before and After 140 °C Bake for the $x \approx 0.22$ LPE Sample Passivated with an Oxide Layer	181
5.13	Transition Energies of OPMA and RII Resonance Positions for $x \approx$ an 0.22 LPE Unbaked Samples Passivated With ZnS	182
5.14	Transition Energies of OPMA and Resonance Peaks for an $x \approx 0.22$ LPE Sample Passivated With ZnS After 220°C Bake ...	183
5.15	Wavelength Dependence of OPMA Photoconductive Response for an $x \approx 0.23$ LPE Sample	184
5.16	Fan Chart of Transition Energies for OPMA fit with Resonance Peak Positions for the $x \approx 0.23$ LPE Sample	186
5.17	Wavelength Dependence of RII Spectra for an $x \approx 0.24$ LPE Sample	188

CHAPTER 1

INTRODUCTION

This dissertation encompasses investigations in two disciplines: nonlinear dynamics of semiconductor device circuits, and characterization of deep energy levels in $\text{Hg}_{1-x}\text{Cd}_x\text{Te}$ by using Magneto-Optical Spectroscopy. The experimental systems for the nonlinear dynamics studies included driven diode resonator systems, coupled tunnel diode relaxation oscillators, and the dynamical Hall effect in n-InSb. For the deep energy level studies of $\text{Hg}_{1-x}\text{Cd}_x\text{Te}$, a new technique called Resonant Impact Ionization (RII) spectroscopy was extensively used to investigate deep trap levels in both bulk and LPE $\text{Hg}_{1-x}\text{Cd}_x\text{Te}$ samples with x value from 0.22 to 0.24. The backgrounds on these two fields are presented in Sec. 1.1 and Sec. 1.2 respectively.

1.1 Nonlinear dynamics of electronic circuits and semiconductor n-InSb

A variety of oscillatory instabilities in a wide range of physical systems due to nonlinear effects have been observed and investigated for the past two decades. These systems include electronic circuits^[1-4], semiconductors^[5-17], chemical reactions^[18-20], optical systems^[21-23], and continuum hydrodynamics systems^[24-30]. Particularly in the last several years, many new results have been found in experimental chaos^[31]. Many esoteric theoretical predictions from chaos theory and concepts have been explored^[31], e.g., mode locking, tori, Curry-Yorke scenario to chaos, golden means, fractals, strange attractors, stability of chaotic attractor, scaling laws, *etc.* The studies of these experimental dynamical systems

not only confirm many theoretical predictions, but also facilitate the dramatic shift of emphasis toward applications of chaos^[31]. Two most notable examples are the synchronization of chaos and the stabilization of chaotic attractors.

In all of the chaos experiments an enormous challenge is that of data analysis. For example, many concepts in nonlinear dynamics are complex and abstract. These include concepts such as: fractal dimension, phase space, phase portrait, Poincarè section, autocorrelation function, and bifurcations. Thus, they are very difficult to observe directly from the experiments. In addition, partly because nonlinear dynamics is still a young discipline and partly because of the nature of nonlinear dynamics itself, there are very limited quantities which can quantitatively characterize a chaotic attractor. Quite often these quantities require high quality data in large amounts. One such quantity commonly used is the Lyapunov exponent.

Taken's theorem^[32] allows one to extract most of the important concepts from a single system observable. In other words, if a time series for one system observable from the experiment is obtained, then one can reconstruct the phase portrait, and this phase portrait is diffeomorphic to the original dynamics of the system. This means that one can obtain estimates of quantities such as phase portrait, Poincarè maps, autocorrelation functions, and most importantly Lyapunov exponents directly from a single time series.

Several experimental techniques are employed to obtain the single time series, its power spectrum, and autocorrelation function. Then these quantities are used to reconstruct the phase portrait and Poincarè sections (Sec. 2.1, 2.2). Practically, the calculation of Lyapunov exponents from a time series is complicated, and different approaches have to be taken for different dynamical

systems and circumstances. Three algorithms (Sec. 3.1) developed recently are employed in this dissertation, and Lyapunov exponents for all of the experiments reported here are successfully evaluated.

A driven diode resonator system is a simple electronic circuit that consists of pn-diodes, inductors, and resistors. Early work^{[2][3][4]} has shown that (1) a single diode resonator system exhibits a period doubling cascade, hysteresis, *etc.* and (2) a coupled system exhibits quasiperiodicity, Hopf bifurcation and periodic locking. However, there still remains controversy on the proper approaches for modeling of the systems. Testa, Perez, and Jefferies^{[33][34]} insisted that the observed period doubling and chaotic behavior were due to the nonlinearity of the effective capacitance on the diode pn-junctions. On the other hand, Hunt, Rollins and Su^[3] argued that the nonlinear reverse bias capacitance of the pn-junction is not responsible for the behavior observed. Instead, the rather large reverse recovery time of such diodes was essential. Recently Yu *et al.*^[35] gave a third approach, which is to employ the well-known *SPICE* program^[36] to achieve a realistic modeling of the diode. This model, which is detailed in this dissertation, gives more detailed expressions and realistic parameters corresponding to the particular type of diode. Although it does not resolve the controversy surrounding the modeling, this model is shown to achieve excellent agreement with experiment for both the single and coupled diode resonator systems. More importantly, this model becomes more useful for complex coupling diode resonator systems that represent higher dimensional dynamical systems.

The importance to carefully study diode resonator systems can be seen if one realizes that much more complex dynamical systems can be built out of

this simple building block (single diode resonator). In addition one can experiment and explore many different ideas to study the control of chaos and the synchronization of chaos. Doing the experiments on such systems is also superior over computer simulation because it is cheaper, easier to implement, and much faster.

One typical example to extend the diode resonator experiments is to study the stabilization of chaos. The idea that one can stabilize periodic orbits in a chaotic system was coined by Ott, Grebogi and Yorke (OGY)^[37]. It is well known^[38] that a typical chaotic attractor contains infinitely many unstable periodic orbits of all periods. By choosing small time dependent perturbations in an accessible system parameter, one can stabilize the system to an existing periodic orbit embedded in the original chaotic attractor. The stabilization of chaos not only has theoretical interests, but also potential applications. One possible application is to apply this technique to a laser system to achieve stable and high power output^[39]. These stabilization schemes have been realized experimentally in several different dynamical systems, including electronic circuits^[40], laser systems^{[39][41-43]}. However, most of the experiments were done on the most simple chaotic attractor, namely, a three-dimensional dynamical system, and researchers were only considering controlling a chaotic attractor to a periodic state.

In the investigation of chaos stabilization reported in this dissertation, the proportional feedback technique has been applied to the single and line-coupled diode resonator systems. As a result, both high period periodic states and quasiperiodic states have been stabilized. These stabilized quasiperiodic states have important implications for further investigation, which is whether there exist

any quasiperiodic orbits embedded in chaotic attractor. The fact that the quasiperiodic orbits can only be stabilized in coupled-diode resonator systems indicates that this is associated with higher dynamical systems. Therefore, quasiperiodic oscillations can possibly be used to characterize chaotic attractors of high dimensional systems.

Another interesting idea to exploit chaos is to investigate the possible synchronization of chaos^[44-47]. The study of this synchronization scheme not only can be provided as a model for nonlinear systems with many degrees of freedom, but also can help to explore biological information processing and even engineering applications. In this dissertation, experimental observations have shown that by weakly coupling the two tunnel diode oscillators while both are in chaotic regimes, a synchronization to a common chaotic orbit can be obtained.

Spontaneous or periodic externally driven oscillations and chaotic behavior related to impact ionization have been studied experimentally in a number of semiconductors: n-GaAs^[48-51], p-Ge^[52-56], n-InSb^{[57][58][16]} and n-Si^[59]. Various types of periodic oscillations and chaotic behaviors were observed in these experiments, including period doubling bifurcation to chaos (Feigenbaum scenario), quasiperiodic oscillations, intermittency, and the Ruelle-Takens-Newhouse scenario. Semiconductors, with generation-recombination kinetics and easily tunable parameters, provide an ideal testing ground for low dimensional models of dynamical systems with chaotic states.

In this dissertation, further investigations on both the self-generated and driven oscillations in InSb in the presence of a transverse magnetic field at liquid helium temperatures are presented. The experiments have shown that the system can have a period doubling route to chaos. More importantly, there is a

good agreement on the magnetic field versus current density phase diagram between the experiment and theory that was proposed by Hüpper and Schöll. Lyapunov exponents were also obtained to confirm the existence of chaos. For the AC-driven system, the stability of a chaotic attractor against an external AC-driven source was investigated and the results were compared to that of a simple driven oscillator. The induced transitions from chaos to periodicity by the AC-driving source are also studied. The experimental result agrees well with a conjectured scaling law.

1.2 Characterization of deep energy levels in $\text{Hg}_{1-x}\text{Cd}_x\text{Te}$

Impurities and defects in semiconductor $\text{Hg}_{1-x}\text{Cd}_x\text{Te}$ have long been considered as an important factor^[60-62] which limits the performance and yield of infrared detector systems made from this material. Particularly, those energy levels which lie deep in the forbidden gap region and have large capture cross-sections can make an enormous impact on the detector performance. Even though considerable effort has been made in characterizing these impurities and defects, many of these defects are still remain poorly understood because of the lack of sensitive techniques to detect and measure these trap levels. Deep Level Transient Spectroscopy (DLTS)^[63-65], which is usually used to study deep levels in silicon and III-V semiconductors, is not appropriate for narrow gap semiconductor like HgCdTe since it does not provide larger enough temperature range for DLTS measurement as the wide gap semiconductor does. Other techniques, such as thermally stimulated capacitance (TSC)^[66] is limited by the background drift due to leakage currents, and the admittance spectroscopy (AS)^[67] is appropriate only for majority carrier traps. Other reasons for the

difficulty to detect deep trap levels are that deep trap states usually have very small absorption cross-sections and are of low density. Very recently, a new technique, which involves the resonant impact ionization (RII)^[68-71] of a valence electron by a conduction band electron, has been developed to sensitively and accurately detect the deep trap levels.

The mercury (Hg) vacancy is a natural defect in HgCdTe due to the rather weakly bound nature of the Hg lattice and is commonly believed to act as an acceptor^[72]. During the manufacturing process, the Hg vacancy concentration in HgCdTe is generally reduced from a large as-grown concentration by a post-anneal in a Hg-rich atmosphere. During this anneal, Hg atoms enter the lattice as interstitials and move through the crystal until they encounter and fill vacancy sites. Other methods^{[70][73]} such as ion-beam milling and the baking of an anodic oxide at the surface exist to introduce Hg atoms, as interstitials, into the HgCdTe lattice and can be used to convert vacancy-doped p-HgCdTe to n-HgCdTe. Until now, a very limited amount of work has been done to study the electrical properties of Hg Interstitials in HgCdTe. Recently, two separate experiments^{[70][73]} on bulk HgCdTe samples have provide evidence that Hg interstitials appears to form deep trap levels. The Hg interstitials in these experiments are introduced to the sample by either ion-beam milling or oxide baking.

In this dissertation, the investigation of Hg interstitials in both bulk and LPE HgCdTe samples by using the RII technique is presented and described. The samples are grown and/or processed under different conditions to control the concentration of Hg interstitials. The effect of deep trap levels on the Two Photon Magneto-Absorption (TPMA) process is also studied and the result is

compared with theory.

This dissertation consists of six chapters. Chapter 2 describes the experimental apparatus, techniques and numerical methods used in this dissertation. Chapter 3 presents the time series analysis methods used for the data analysis of nonlinear dynamical experiments. Chapter 3 also include the investigation results on the nonlinear dynamics of driven diode resonator system, the stabilization of chaos in driven diode system, and synchronization of chaos in coupled tunnel diode oscillator system. Chapter 4 shows the experimental results on the autonomous and externally driven periodic and chaotic oscillations in n-InSb under transverse magnetic field. Chapter 5 reports the investigations of Hg interstitials in both bulk and LPE samples by using RII spectroscopy. Chapter 6 is the conclusion of this thesis. Suggestions for the future work are also included in Chapter 6.

CHAPTER 1 REFERENCES

1. J.P. Gollub, E.J. Romer, and J.E. Socolar, J. Stat. Phys. **23**, 321(1980).
2. J. Testa, J. Perez, C. Jefferies, Phys. Rev. Lett. **48**, 714(1982).
3. R. W. Rollins and E. R. Hunt, Phys. Rev. Lett. **49**, 1295(1982).
4. P.S. Lindsay, Phys. Rev. Lett. **47**, 1349(1981).
5. G. N. Maracas, W. Porod, D. A. Jonson, and D. K. Ferry, Physica **134B**, 276 (1985).
6. K. Aoki, O. Ikezawa, N. Mugibayashi, and K. Yamamoto, Physica **134B**, 288 (1985).
7. W. Knap, M. Jezewski, J. Lusakowski, and W. Kuszko, Solid-State Electron **31**, 813(1988).
8. K. Aoki, Y. Kawase, K. Yamamoto, and N. Mugibayashi, J. Phys. Soc. Jpn. **59**, 20(1990).
9. S. W. Teitworth, R. M. Westervelt, Phys. Rev. Lett. **51**, 825(1983).
10. B. Rohricht, B. Wessely, J. Peinke, A. Muhlbach, J. Parisi, and R. P.Huebener, Physica **134B**, 281(1985).
11. J. Peinke, A. Muhlbach, B. Rohricht, B. Wessely, J. Mannhart, J. Parisi, and R. P. Huebener, Physica **23D**, 176(1986).
12. E. Schöll, J. Parisi, B. Rohricht, J. Peinke, and R. P. Huebener, Phys. Lett. **A119**, 419(1987).
13. U. Rau, J. Peinke, J. Parisi, R. P. Huebener, and E. Schöll, Phys. Lett. **A124**, 331(1987).

14. D. G. Seiler, C. L. Littler, R. J. Justice, and P. W. Milonni, Phys. Lett. **A108**, 462(1985).
15. X. N. Song, D. G. Seiler, and M. R. Loloee, Appl. Phys. **48**, 137(1989).
16. X.N. Song, Z. Yu, G. Albert, J.M. Kowalski, C.L. Littler and J.M. Perez. "Autonomous and Externally Driven Periodic and Chaotic Hall Voltage Oscillations in n-InSb", **Proceedings of the 1st Experimental Chaos Conference** (World Scientific, Singapore, 1992).
17. K. Yamada, N. Takara, H. Imada, N. Miura, and C. Hamaguchi, Solid-State Electron **31**, 809 (1988).
18. J.L. Hudson, M. Hart and D. Marinko, J. Chem. Phys. **71**, 1601(1979).
19. J.C. Roux, A. Rossi, S. Bachelart and C. Vidal, Physica, **2D**, 395(1981).
20. R.H. Simoyi, A. Wolf and H.L. Swenny, Phys. Rev. Lett. **49**, 245(1982).
21. The special issue on the Instabilities in Active Optical Media, J. Opt. Soc. Am. **B2**, No.1, (1985).
22. R.W. Boyd, M.G. Raymer, and L.M. Narducci, *Optical Instabilities*, (Cambridge University Press, London, 1986).
23. F.T. Arecchi and R.G. Harison, *Instabilities and Chaos in Quantum Optics*, Vol. 34 of Springer Series in Synergetics, (Springer-Verlag, Berlin, 1987).
24. G. Ahlers and R. Behringer, Phys. rev. Lett. **40**, 712(1978).
25. P. Bergè, M. Dubois, P. Manneville and Y. Pomeau, J. Phys. Lett. **41**, L341(1980).
26. M. Giglio, S. Musazzi and U. Perini, Phys. Rev. Lett. **47**, 243(1981).
27. J.P. Gollub and S.V. Benson, J. Fluid. Mech. **100**, 449(1980).
28. A. Libchaber and J. Maurer, J. Phys. Lett. (Paris) **39**, L369(1978).
29. H.L. Swinney and J.P. Gallub, Physics Today **31**, No.8, 41(August 1978).

30. R. Shaw, C.D. Andereck, L.A. Reith and H.L. Swinney, Phys. Rev. Lett. **48**, 1172(1982).
31. S. Vohra, M. Spano, M. Shlesinger, L. Pecora, and W. Ditto, **Proceedings of the 1st Experimental Chaos Conference** (World Scientific, Singapore, 1992).
32. F. Takens, "Detecting Strange Attractors in Turbulence." in: Lecture Notes in Mathematics No. 898, (Springer, Berlin, 1981) p. 366.
33. J. Testa, J.M. Perez, C. Jefferies, Phys. Rev. Lett. **49**, 1055(1982).
34. R. Van Buskirk and C. Jefferies, Phys. Rev. **A31**, 3332(1985).
35. Z. Yu, J. Steinshnider, C.L. Littler, J.M. Perez, J.M. Kowalski, Accepted by Phys. Rev. E.
36. *SPICE*, Department of Electrical Engineering and Computer Sciences, U. C. Berkley.
37. E. Ott, Celso Grebogi, and James A. Yorke, Phys. Rev. Lett. **64**, 1196 (1990).
38. G. H. Gunarante, and P. S. Linsay, Phys. Rev. Lett, **63** 1(1989).
39. R. Roy, T.W. Murphy, Jr., T.D. Maier, Z. Gills, and E.R. Hunt, Phys. Rev. Lett. **68**, 1295(1992).
40. E. R. Hunt, Phys. Rev. Lett. **67**, 1953 (1991).
41. J. Singer, Y-Z Wang, and H.H. Bau, Phys. Rev. Lett. **66**, 1123(1991).
42. S. Bielawski, D. Derozier, and P. Glorieux, Phys. Rev. **A47**, 2492(1993).
43. F.T. Arecchi, G. Giacomelli, A. Lapucci, and R. Meucci, Phys. Rev. **A49**, 4997(1991).
44. K. Kaneko, Phys. Rev. Lett. **63**, 219(1989); **65**, 1391(1990); Physica **41D**, 139(1990).

45. L.M. Péroca, R.L. Carroll, Phys. Rev. Lett. **64**, 821(1990).
46. J.M. Kowalski, G.L. Albert and G.W. Gross, Phys. Rev. **A42**, 6260(1990)
47. W. L. Ditto and L.M. Péroca, *Scientific American*, **78**, August 1993.
48. G. N. Maracas, W. Porod, D. A. Jonson, and D. K. Ferry, Physica **134B**, 276 (1985).
49. K. Aoki, O. Ikezawa, N. Mugibayashi, and K. Yamamoto, Physica **134B**, 288 (1985).
50. W. Knap, M. Jezewski, J. Lusakowski, and W. Kuszko, Solid-State Electron **31**, 813(1988).
51. K. Aoki, Y. Kawase, K. Yamamoto, and N. Mugibayashi, J. Phys. Soc. Jpn. **59**, 20(1990).
52. S. W. Teitworth, R. M. Westervelt, Phys. Rev. Lett. **51**, 825(1983).
53. B. Rohricht, B. Wessely, J. Peinke, A. Muhlbach, J. Parisi, and R. P. Huebener, Physica **134B**, 281(1985).
54. J. Peinke, A. Muhlbach, B. Rohricht, B. Wessely, J. Mannhart, J. Parisi, and R. P. Huebener, Physica **23D**, 176(1986).
55. E. Schöll, J. Parisi, B. Rohricht, J. Peinke, and R. P. Huebener, Phys. Lett. **A119**, 419(1987).
56. U. Rau, J. Peinke, J. Parisi, R. P. Huebener, and E. Schöll, Phys. Lett. **A124**, 331(1987).
57. D. G. Seiler, C. L. Littler, R. J. Justice, and P. W. Milonni, Phys. Lett. **A108**, 462(1985).
58. X.N. Song, "*Magneto-Optical and Chaotic Electrical Properties of n-InSb*", Thesis, University of North Texas, December, 1991.

59. K. Yamada, N. Takara, H. Imada, N. Miura, and C. Hamaguchi, Solid-State Electron **31**, 809 (1988).
60. D.L. Polla and C.E. Jones, Solid State Commun. **36**, 809(1980).
61. A.T. Hunter, D.L. Smith, and T.C. McGill, Appl. Phys. Lett. **37**, 200(1980).
62. C.E. Jones, V. Nair, and D.L. Polla, Appl. Phys. Lett. **39**, 248(1981).
63. D.V. Lang and R.A. Logan, J. Electron Mater. **4**, 1053(1975).
64. B.L. Smith, T.J. Hayes, A.R. Peaker, and D.R. Wright, Appl. Phys. Lett. **26**, 122(1975).
65. G.L. Miller, D.V. Lang, and L.C. Kimerling, Ann. Rev. Mater. Sci. 377-448(1977).
66. D.L Polla and C.E. Jones, J. Appl. Phys. **51**, 12(1980).
67. C.T. Sah, Solid State Electron. **19**, 975(1977).
68. D. G. Seiler, J.R. Lowney, C.L. Littler, I.T. Yoon, and M.R. Loloee, J. Vac. Sci. Technol. **B9**, 1847(1991).
69. I.T. Yoon, "*Anisotropy of Conduction Electrons in n-InSb and Extrinsic and Intrinsic Properties of HgCdTe*", PhD thesis, University of North Texas, August, 1991.
70. C.L. Littler, X.N. Song, Z. Yu, J.L. Elkind, D.J. Seiler, and J.R. Lowney, J. Vac. Sci. Technol. **B10**, 1466(1992).
71. C.L. Littler, X.N. Song, Z. Yu, J.L. Elkind, J.R. Lowney, Semicond. Sci. Technol. **8**, s317(1993).
72. W. Scott, E.L. Stelzer and R.J. Hager, J. Appl. Phys. **47**, 1408(1976).
73. J. L. Elkind J. Vac. Sci. Technol. **B10**, 1460(1992).

CHAPTER 2

EXPERIMENTAL AND NUMERICAL METHODS

This chapter describes the experimental setup, techniques, and apparatus for the following experiments: (1) oscillatory instability study of n-InSb in low temperature and high magnetic field (Chapter 4), (2) nonlinear dynamical study of diode resonator systems (Chapter 3), (3) control of chaos in the diode resonator systems (Chapter 3), (4) investigation of the deep energy levels in HgCdTe by using magneto-optical spectroscopy (Chapter 5). Lastly, the numerical methods used in this dissertation are presented.

2.1 Experimental Setup for Oscillatory Instability Studies of n-InSb in Liquid Helium Temperature and High Magnetic Field.

Fig. 2.1 is a diagram that shows the sample layout for this experiment. In this sample configuration, the magnetic field **B** is transverse to the sample current **I**. The InSb samples were obtained from Cominco American Inc., and they have the following specifications: at 77K extrinsic electron carrier concentration is $9 \times 10^{13} / \text{cm}^3$, and electron mobility is $7 \times 10^5 \text{ cm}^2/(\text{V}\cdot\text{sec})$. By using a Servomat sparkgap cutting machine, the samples were cut into rectangular bars, with thickness from 0.1 mm to 0.4 mm, width from 0.6 mm to 0.9 mm, and length from 5 mm to 10 mm. Then sample surfaces were polished mechanically. Finally the ohmic electric contacts were made to the sample using pure indium as solder, and $60\mu\text{m}$ gold wires as electric leads. A constant current was supplied, and the resulting longitudinal voltage and Hall voltage were

measured simultaneously.

Fig. 2.2 is a block diagram showing the experimental setup. All outputs were buffered to eliminate the effects of external influences on the sample itself. An X-Y recorder was used to record the Hall voltage versus current or longitudinal voltage versus current characteristics of the samples under different magnetic field. The phase plots and Poincaré sections were obtained using oscilloscopes, as detailed in Sec. 2.2. The oscilloscope and spectrum analyzer were used to monitor the signals and their power spectra, respectively. The digitizer employed here has two channels with 64 K memory each, 8-bit precision, and up to 1 MHz digitizing speed. There are tradeoffs between choosing high precision and high speed for digitizers for the same cost. High speed was chosen here because the output signals of oscillatory voltages are not spiky and well behaved; however, the interested frequencies are often as high as around 50 KHz. A Turbo-c program was written to transfer data from the digitizer to IBM personal computer for data analysis. The autocorrelation functions for each time series can be computed and displayed on the IBM/PC in the real time.

2.2 Experimental Setup for Nonlinear Dynamical Study of Diode Resonator Systems.

Fig. 2.3 shows a schematic diagram of the experimental apparatus used for the nonlinear dynamical studies of the diode resonator systems. The diode circuits are very sensitive to external noise, so buffers were used to measure the voltages across a resistor or a diode throughout the experiments. The driving source is a signal generator which can supply a sinusoidal signal with

frequencies up to 100 KHz and adjustable amplitude. In addition it can also sweep the amplitude from zero to the maximum voltage with various time constants. An oscilloscope and an HP 3585A spectrum analyzer were used to monitor the output signals.

Electronic techniques, first used by Perez *et al.*^[1], were employed here to directly observe bifurcation diagrams, Poincaré sections, phase plots, and return maps on the oscilloscope in real time. The key idea to obtain the bifurcation diagram is to detect the peak position of the current signals with zero crossing detectors, and use a pulse generator triggered by the output of a zero crossing detector to strobe the oscilloscope. With an adjustment of timing delay one can achieve strobing at each peak of the system signal. By sweeping the amplitude of the driving voltage and using this as the input for the horizontal deflection voltage, a diagram of peak values versus driving amplitude is displayed on the CRT of the oscilloscope. Conceptually, this diagram corresponds to the Poincaré map on the plane of $d\phi/dt = 0$ and $d^2\phi/dt^2 \leq 0$ in a $\{\phi, d\phi/dt, d^2\phi/dt^2\}$ phase space. By changing the control parameter of the system (driving amplitude in this case), this map will undergo bifurcation between different changing system states (periodic, chaotic, *etc.*). All bifurcation diagrams presented in this dissertation were constructed for this type of Poincaré map.

In addition, if one feeds the horizontal deflection with system output signal and the vertical deflection with a certain timing delayed the same signal, one will obtain a reconstructed 2-D phase plot for the system on the oscilloscope. According to Takens^[2], this reconstruction should faithfully reflect the real phase plot (See Section 3.2 for details). In the same plot, the strobed trace will be the Poincaré section. All of the pictures shown on the oscilloscope and on the

spectrum analyzer were taken by a 35 mm SLR camera.

To obtain the time series of the system signals, an Analog Devices FAST-16 series digitizer was used. It has 16-bit resolution, 1 MHz speed and 1 Mega-word memory. A Turbo-C program was written to control the digitizer and transfer the data from digitizer memory to IBM/PC.

2.3 Method to Stabilize Chaos in the Diode Resonator Systems. (Proportional Feedback Technique)

The implementation of a stabilizer is based on an idea by Ott, Grebogi and York^[3] (OGY). It is similar to a method developed by Hunt^[4], but with some modifications. Basically, one samples the peak current I_n of the diode system; for all peaks within a preselected adjustable window, the difference between the peak position and the center of the window is then computed. This difference is amplified with an adjustable gain and used as a control signal by superposition with the driving sinusoidal signal. The time delay and duration of the control signals are also adjustable parameters of the control circuit.

Fig. 2.4 is a schematic diagram of the logic and electronic components for the stabilizer. A signal generator drives the diode resonator system (single diode resonator or line-coupled diode resonator system). The current through each system is converted to a voltage by the I/V converter. The dc level of this signal may be adjusted by the offset. One unique property of the driven diode resonator system is that a current peak occurs at every driving cycle, therefore one can detect the peak position and generate a peak reference pulse from the driving source by the zero crossing. Using this pulse to trigger a Sample/Hold with the above voltage as input, one can obtain the peak level voltage which reflects the

peak value of the system current. This peak level can then be fed into a window comparator and another Sample/Hold. The window's width and position level can be adjusted. Thus if the peak level is within the selected window, the difference is generated. After it goes through an analog switch and an amplifier, the resultant feedback control signal is generated and fed to the multiplier. This multiplier modulates the system's driving signal by the feedback signal. If the peak level falls out of the window, a zero control signal is generated.

2.4 Magneto-Optical Measurement Technique

(1) Sample Preparations

The sample preparation was carried out both at Texas Instruments and the University of North Texas. The measurements were performed at University of North Texas. Different kinds of samples used in this investigation are discussed as follows.

Bulk Samples ($x \approx 0.22$ and $x \approx 0.24$): The bulk samples were rectangular slabs of dimensions $\approx 8\text{mm} \times 1\text{mm} \times 0.2\text{mm}$, cut from larger rectangular slices obtained from ingots grown by standard solid state recrystallization methods and thinned to $\approx 0.2\text{mm}$ in such a manner that the p-type core was no longer present. The thinning of the larger slices was accomplished by lapping both sides with alumina grit and then chemo-mechanically polishing with a 2% solution of bromine-methanol. The electrical properties of the bulk $x \approx 0.22$ and $x \approx 0.24$ samples at 77K were listed in table 2.1.

Before cutting the final slabs to be used as samples, each slice was cut into two pieces. One piece was anodized in a 0.1M KOH solution (90% ethylene

glycol and 10% de-ionized water) at a 200mA constant current. The anodization was terminated after achieving a voltage drop of 15 V, which corresponding to an oxide thickness of approximately $\approx 600 \text{ \AA}$. This sample was then baked at 140°C for approximately five hours to partially decompose the oxide and to introduce Hg interstitials into the materials. The second piece did not receive the treatment and served as a control. The electrical contacts were made to the bulk samples by using pure indium. The samples were free standing, held in place by the current leads and Hall leads.

x values	$N_d - N_a \text{ (cm}^{-3}\text{)}$	$\mu \text{ (cm}^2 \text{V}^{-1} \text{s}^{-1}\text{)}$
$x \approx 0.22$	3.3×10^{14}	1.51×10^5
$x \approx 0.24$	2.5×10^{14}	1.21×10^5

Table 2.1 Electrical Properties of the Bulk $\text{Hg}_{1-x}\text{Cd}_x\text{Te}$

LPE samples ($x \approx 0.23$ and $x \approx 0.24$): The LPE samples were grown on $\langle 111\text{B} \rangle$ -oriented CdZnTe substrates using a tellurium-rich solution, where one of the melts contained indium at a mid- 10^{14} cm^{-3} concentration as a dopant. Both the indium-doped and undoped samples were annealed after growth in a Hg-saturated atmosphere to reduce the concentration of metal vacancy levels.

Surface passivation is extremely important for HgCdTe devices^[5]. Two different passivation technologies have been used. The first involves the deposition of a thick ZnS film. The second is a two-layer combination of a thin

native film and a thick deposited dielectric film (ZnS, or CdTe). For the second one, the native layer is made by anodic oxide, which is a mixture of HgTeO_3 , CdTeO_3 , and TeO_2 . It has been found^[6] that this anodic oxide can be thermally decomposed by baking and thus introduce Hg interstitials deeply into the LPE sample. The details of passivation procedure for LPE samples used in this dissertation are proprietary technologies of Texas Instruments, Inc. and therefore cannot be discussed here.

The electrical contacts were made to the LPE samples by using pure indium. Then the samples/substrates were attached to a holder by using a heat sink compound.

(2) Experimental Apparatus (Fig. 2.5)

Laser system and optics: The primary laser used is a Model 150 CO_2 system of Apollo Lasers Inc. It is an axial-flowing gas, electric discharge, water-cooled laser system that can produce up to 150 Watts/line. It can operate in the CW, chopped, pulsed modes and output more than 100 grating-tunable wavelengths in the $9.14\mu\text{m}$ - $11.01\mu\text{m}$ region. Most of the operation are controlled by IBM Microcomputer.

For the experiments as described in Chapter 4, the laser was operated in CW mode. The beam was first condensed and collimated by a ZnSe telescope. A variable frequency light chopper was used to produce laser pulses. The chopper was located at the focal point of a ZnSe lens with focal length of 2 inches. A HeNe laser was transmitted through the exact position on the chopper as the CO_2 beam on a Si detector to produce synchronized reference pulses. Then the CO_2 beam was collimated using

another 2 inch focal length ZnSe lens. Usually the CO₂ laser was chopped into 20 μ sec wide pulse with a low duty cycle to prevent the lattice-heating effect. In addition, an attenuator was used to adjust beam intensity before it was focused onto the sample by another ZnSe lens. The HeNe laser pulses obtained from the chopper were detected by a Si photodiode, and used to trigger the sampling electronics. During the experiments a CO₂ spectrum analyzer was used to monitor the excitation mode of the laser system.

Magnetic field and low temperature environment: High magnetic fields and low temperatures were obtained by using a Janis Research Superconducting Magnet/Cryostat System. Within the system, the magnetic field was produced by a superconducting solenoid that is made from filamentary niobium tin wire and niobium titanium wire. It can reliably produce fields of up to 12.0 Tesla at 4.2K in a 53mm bore, and it is capable of being ramped up and down uniformly at an adjustable speed. A modulation coil is also contained in the solenoid, and it can be used to produce a ± 500 Gauss modulation field in the bore, superimposed on the DC magnetic field. The main solenoid and modulation coil are immersed in a liquid helium bath, and the sample chamber is located at the center of magnet. There is a capillary tube with a needle valve control from helium bath to sample chamber. The temperature of the sample can be controlled from 2K to 300K (within ± 0.5 K) by the flowing of liquid helium and the DRC-82 temperature controller from Lake Shore Cryogenics, Inc.

Signal processing techniques: The signal processing procedure without magnetic field modulation is the following: A He-Ne laser beam passed through the same chopper as CO₂ beam is detected by a Si photodiode, and generates a pulse to trigger the boxcar averager unit. The signal from either Hall leads or longitudinal

leads of the sample are amplified, and then input to the boxcar. The aperture delay of the boxcar was adjusted so that it samples the desired position of the signal. The integrated output of the boxcar yield averaged output for the selected position of the input signal.

In order to do magnetic field modulation, a 22 Hz small ac magnetic field (± 500 Gauss) was superimposed on the dc field. The same ac signal used to excite modulation field is also used as external reference to the lock-in amplifier. When frequency is set to 22 Hz and 0 degree phase difference between reference and input signals, the lock-in amplifier will phase-sensitively detect 22 Hz component of boxcar averager output signal. To obtain fine details in the photoconductive response, the dc magnetic field is slowly swept. By setting lock-in amplifier frequency to 22 Hz and 0 degree phase difference, the first derivative photoconductive versus magnetic field is obtained. If the lock-in amplifier is set to 44 Hz and 90 degree difference with the input signal, second-derivative type spectra is obtained^{[7][8]}.

Data acquisition and processing: In this dissertation, most of the time data are needed in the digital form so that further data analysis can be performed. Therefore, data acquisition and processing are a very important part of the experiments.

Two kinds of micro-computers were used in the experiments of this dissertation: An HP9000 and IBM/PC. The HP 9000 series 300 computer in the solid state lab of UNT has the following specifications:

Operating System:	Basic 5.1
Processor:	MC68030
Display:	Bitmap (512×512)

Memory:	1 Megabytes
Hard disk:	40 Megabytes
Interfaces:	GP-IB(IEEE488), GPIO, RS232.

This computer provides a central control over a variety of instruments to achieve instrument control, data acquisition, data displays, data transformations, and data outputs, *etc.* Through the GP-IB interfaces (also called IEEE488 interface), one can connect GP-IB compatible instruments. The instruments used in this work were: HP3585A power spectrum analyzer, HP7090A plotting system which has three channels of built-in digitizers, SRS SR850 lock-in amplifier, Fluke 8840A multimeter, Keithley 175 multimeter, Keithley 220 Programmable Current Source, Tektronix 7904 oscilloscope with 7D20 programmable digitizer, and Palm Beach Cryophysics Inc.'s 4025 cryogenic thermometer/controller. Through the same interface it can also communicate with IBM/PC which has a Tecmar IEEE488 interface board.

A typical example of these applications is to design a system which can display magneto-transport or magneto-optical spectra in real time, plot the result when the hardcopy is needed, and store the data if it is necessary for further processing. Each run of the experiment can take between zero and 20 min; thus, the signal variation over this period is very slow. Therefore the speed of the digitizer can be in the range of 10 to 100 Hz (one data point per 0.01 sec up to one data point per 0.1 sec). However, the memory storage has to be very large (approximately 50, 000 data points). A further complication is that the range of the signal is not known a prior, so the parameter settings for the digitizer and display must be adjustable during the run without stopping the experiment. To solve this problem, the HP computer was connected to the HP 7090A plotter

through GP-IB. The plotter has built-in digitizers with 12-bit resolution, up to 500 Hz speed and signal range $\pm 100V$. It has both internal trigger mode and external trigger mode. All of the functions can be remotely controlled by computer through GP-IB interface. A program that was used to perform these functions. The basic algorithm was as follows: The HP 9000 will initiate the digitizer in the plotter to digitize the data (both axes, x: magnetic field, y: signal), and then transfer them to the computer memory. The data collected is displayed on its monitor by drawing a curve representing signal versus magnetic field. When a run is finished one has the options to plot the data on the plotter or store data on the hard disk, or both. Several hardware interrupts were set up to handle the parameter changes during the run. These parameters include digitizer speed and its range to customize the digitizer, vertical range and horizontal range on the display so that one can have customized view of the signal.

2.5 Numerical Integration Methods.

Most of the models describing the physical systems are in the form of differential equations. A differential equation with one independent variable is called Ordinary Differential Equation. In this thesis, models for the diode resonator systems, autonomous oscillation of Hall voltage in n-InSb, and tunnel diode relaxation oscillators are all in the form of ODEs. Due to the instabilities of dynamical systems, accuracy, stability and efficiency of numerical methods becomes even more important. The three numerical methods which were used in this dissertation are Runge-Kutta, Gear, and Adams-Moulton Methods.^[9]

CHAPTER 2 REFERENCES

1. J.M. Perez, "*Chaotic Behavior of a Driven P-N Junction*", PhD Thesis, UC Berkeley.
2. F. Takens, in: *Lecture Notes in Mathematics* No. 898 (Springer, Berlin, 1981) p. 366.
3. Edward Ott, Celso Grebogi, and James A. Yorke, *Phys. Rev. Lett.* **64**, 1196 (1990).
4. E. R. Hunt, *Phys. Rev. Lett.* **67**, 1953 (1991).
5. Y. Nemirovsky and G. Bahir, *J. Vac. Sci. Technol.* **A7**, 450(1989).
6. J. L. Elkind *J. Vac. Sci. Technol.* **B10**, 1460(1992).
7. H. Kahlert, D.G. Seiler, *Rev. Sci. Instruments* **48**, 1017(1977).
8. B.T. Moore, D.G. Seiler, and H. Kahlert, *Solid State Elec.* **21**, 247(1978).
9. D. Kahaner, C. Moler and S. Nash, *Numerical Methods and Software*, Chap. 8, (Prentice Hall, 1989).

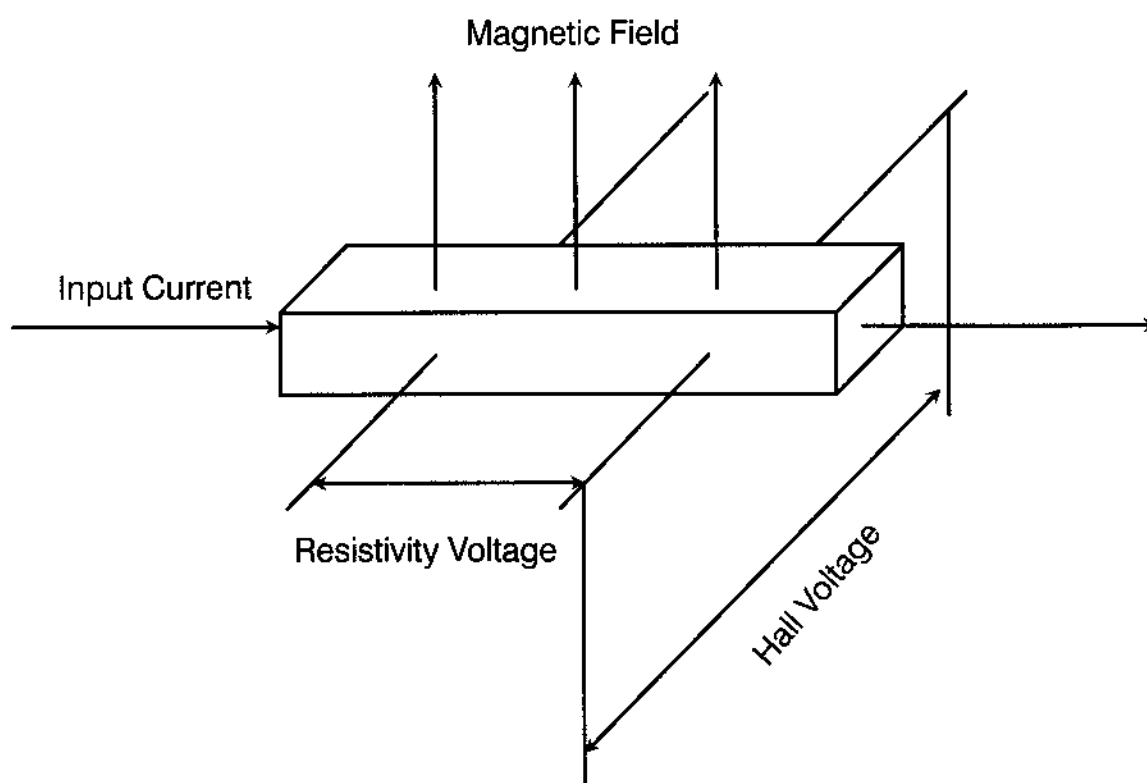


Figure 2.1 Sample configuration for the autooscillatory dynamic study of n-InSb.

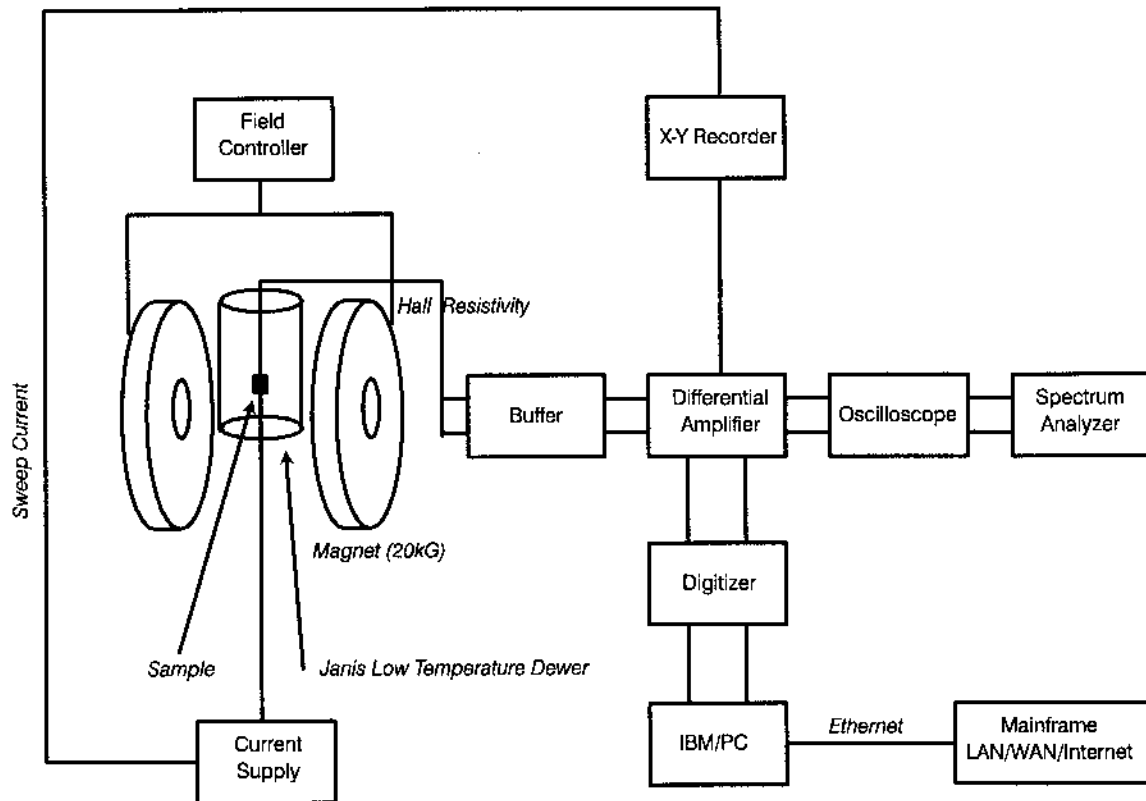


Figure 2.2 Experimental setup for the autooscillatory dynamic study of n-InSb in low temperature and high magnetic field.

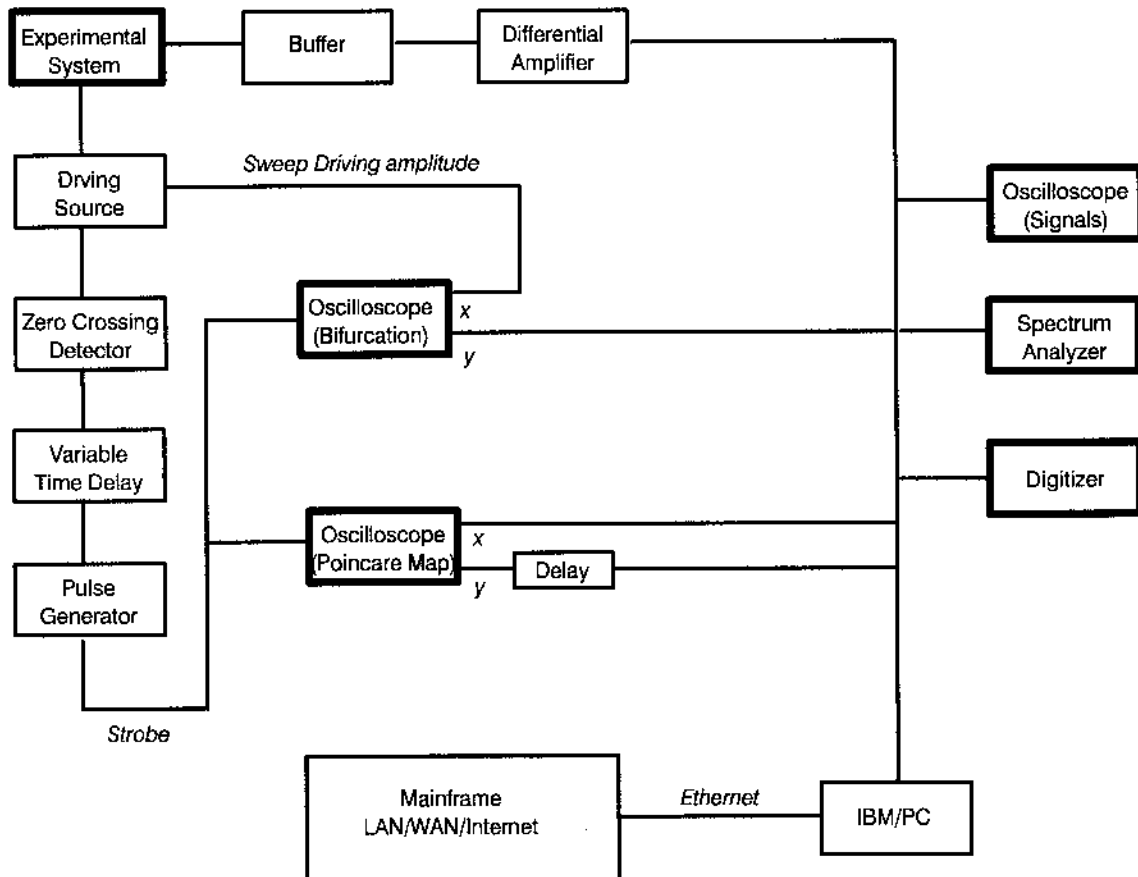
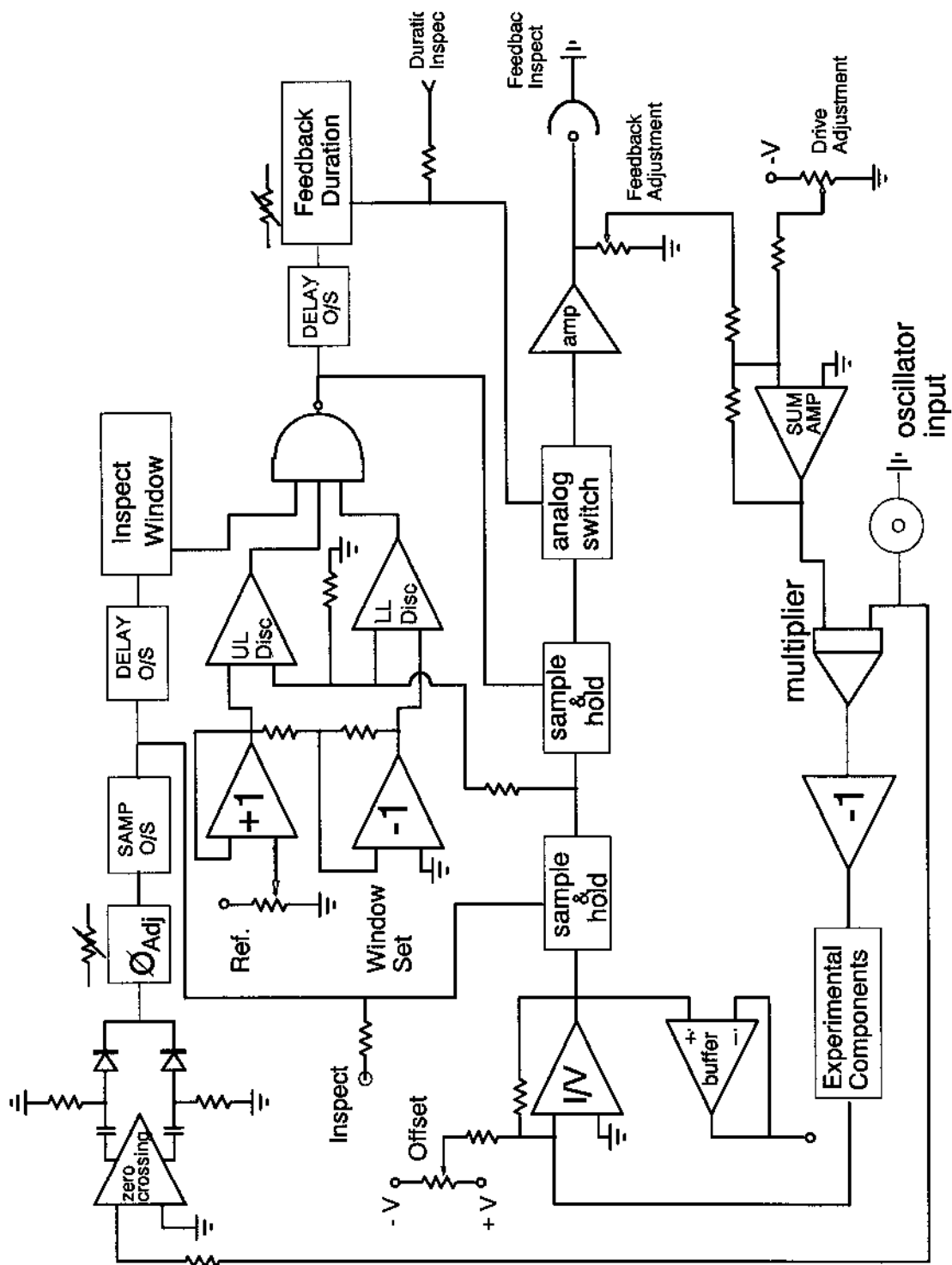


Figure 2.3 Schematic diagram of experimental setup for the nonlinear dynamic study of diode resonator systems.

Figure 2.4 Logic diagram of the circuit which was used to stabilize chaos in diode resonator systems.



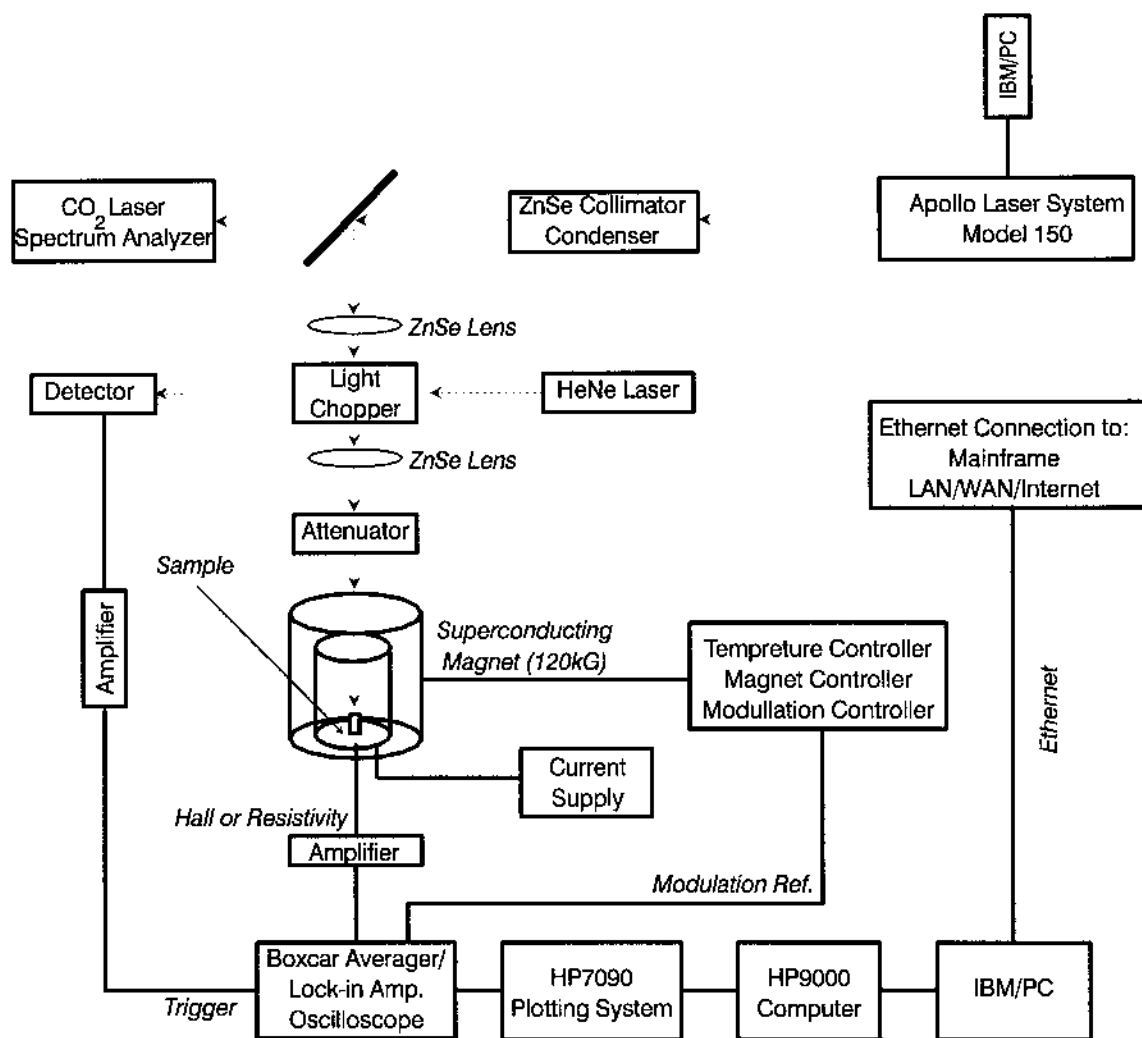


Figure 2.5 Experimental setup for magneto-optical study of HgCdTe materials.

CHAPTER 3

NONLINEAR DYNAMICS OF DRIVEN DIODE RESONATOR SYSTEMS AND SYNCHRONIZATION OF CHAOS IN COUPLED TUNNEL DIODE OSCILLATOR SYSTEMS

This chapter concerns the investigation of nonlinear dynamics in two different electronic circuits: coupled tunnel diode and driven diode resonator systems. The advantage of studying these systems is that they are easy to implement and expand, yet they can exhibit a variety of phenomena of nonlinear dynamics.

Sec. 3.1 is devoted to the data analysis methods used in this chapter and next chapter. Sec. 3.2 describes the simulation and characterization of nonlinear dynamics in driven diode resonator systems. In Sec. 3.3, the stabilization of periodic and quasiperiodic oscillations in driven diode resonator systems is presented. Sec. 3.4 presents experimental results on the synchronization of chaos in coupled tunnel diode resonator relaxation oscillators.

3.1 Time Series Analysis Methods

This section describes some important concepts and techniques for time series analysis in nonlinear dynamic experiments. These include phase portraits, Poincaré sections, power spectra, autocorrelation functions, and Lyapunov exponents.

(1) Phase portraits and Poincaré Sections

In general, *state space* is defined as the space whose axes are the coordinates of position and momentum of the system, and a given dynamic state at a particular time is represented as a single point in this space. A *phase trajectory* is a curve in the phase space representing the time evolution of the system originating from any initial state. The set of phase trajectories for all possible initial conditions constitutes a *phase portrait*.

For illustration, consider only a system with a three-dimensional phase space. Rather than directly studying the solution to the dynamical system, sometimes it is fruitful to observe the points of intersection of the trajectory with a surface. Starting with an initial condition, one thus obtains a set of points comprising a *Poincaré Section*, that is, a graph in two dimensions. The transformation leading from one point to the next is a continuous mapping called *Poincaré Map*.

It has been shown^[1] that the Poincaré section and map have the same kind of topological property as the flow from which they arise. Therefore, the study of Poincaré sections and maps can help one obtain direct information on complex attractors, which otherwise is difficult to do. In most of the experiments discussed in this dissertation, the Poincaré sections can be obtained on the oscilloscope in real time (See Chapter 2 for details). For a periodic oscillation, the corresponding Poincaré section is a single point. For a two-frequency (f_1, f_2) quasiperiodic solution the Poincaré section is a closed curve C ; but when the ratio f_1/f_2 is rational, the Poincaré section is composed of a finite set of points. The Poincaré sections for chaotic attractors generally have more complicated structures.

(2) Embedding Theorem

Given a time series of a single scalar observable $B(t)$ for a complex system, $\{B(t_1), B(t_2), \dots, B(t_N)\}$ and $t_{i+1} - t_i = \tau$, one can reconstruct an m -dimensional phase portrait from vectors $\{B(t_k), B(t_{k+1}), \dots, B(t_{k+m-1})\}$ for $k = 1, 2, \dots, (N-m+1)$. Takens^[2] has proved that this reconstruction is diffeomorphic to the original dynamics provided $m \geq 2d + 1$, where d is the dimension of the underlying attractor. In practice d is not generally known a priori. The easiest approach to this problem is to increase m systematically until additional structure fails to appear when an extra dimension is added. Several more advanced techniques have been proposed to improve this approach^{[3][4][5]}.

(3) Power Spectrum

For discrete finite sequence $\{x_1, x_2, \dots, x_n\}$, the power at frequency k is:

$$P_0 = N a_0^2, \quad P_k = \frac{N}{2} (a_k^2 + b_k^2), \quad 0 < k \leq \frac{N}{2} \quad (3.1)$$

where a_k and b_k are discrete Fourier cosine (sine) transform of the original sequence. Plot of power versus frequency is called power spectrum.

The power spectrum indicates whether the system is periodic or quasiperiodic. For a periodic system with frequency f its spectrum has peaks at f and its harmonics $2f, 3f, \dots$. For a quasiperiodic system with fundamental frequencies f_1, f_2, \dots, f_k its spectrum has peaks at these positions and also possibly at all linear combinations with integer coefficients. In experimental situations, the peaks are not infinitely sharp; they have at least an "instrumental width" $2\pi/T$ in addition to the effects of system noise, where T is the length of the time series used. Generally, two-frequency quasiperiodic phenomena ($k =$

2) are common, and the higher k 's are more difficult to observe. If the signal is mostly noise or it is chaotic, its power spectrum will become broad. White noise does not depend on the frequency, so it will evenly increase the spectrum level. The $1/f$ noise, on the other hand, will have strong contribution to the low frequency end of the spectrum, and decay very quickly as frequency increases. For the chaotic signals, the spectra will generally bear the system characteristics as when the system is non-chaotic, in addition to that the spectra are broad.

Thus the power spectrum can give a good visualization for periodic oscillations, some quasiperiodic oscillations, and their separations from chaotic time evolutions. However, the power spectrum does not provide much quantitative information for the analysis of chaotic signals.

(4) Autocorrelation Functions

For a time series $\{y_1, y_2, \dots, y_n\}$, its autocorrelation is defined as

$$r_j = \frac{\sum_{t=1}^n y_t y_{t-j}}{\sum_{t=1}^n y_t^2} \quad (3.2)$$

for $j = 1, 2, \dots, n$. This function is a measure of the degree of resemblance of the signal with itself as time passes. It actually is the Fourier transform of the power spectrum for the same signal sequence^[6]. Therefore it can be another useful tool for identification of periodic and quasiperiodic oscillations. For periodic oscillations, the autocorrelation function will oscillate with the same number of period as the original signals. It's amplitude theoretically should not decay at all, but in the experimental environment, the noise will cause slow decay. On the

other hand, if the signal is chaotic or mostly noisy, the autocorrelation function amplitude will usually exponentially decay. Again, only quantitative information can be obtained from the autocorrelation function.

(5) Lyapunov Exponents

The concepts described above can only qualitatively identify chaos. To quantitatively characterize a chaotic attractor, one needs a new concept: Lyapunov exponents.

Lyapunov exponents are defined by the time-dependent behavior of small derivations from the flow. Given a d-dimensional system of ODEs:

$$\dot{x} = F(x) \quad (3.3)$$

the solution is designated as:

$$x(t) = T^t x_0 \quad (3.4)$$

where x_0 is the initial condition, T^t is a matrix representing the "flow map". Small deviations from the orbit $x(t)$ are denoted by $\delta x(t)$. Their time evolution is governed by the variational equation:

$$\delta \dot{x} = \frac{\delta F}{\delta x} (T^t x_0) \delta x \quad (3.3a)$$

or:

$$\delta \dot{x} = J(x(t)) \delta x \quad (3.3b)$$

where J is the Jacobian matrix of F . The solution of Eqs. (3.3a) or (3.3b) is written as:

$$\delta x(t) = U^t_{x_0} \delta x_0 \quad (3.5)$$

U is called the fundamental matrix. Now consider a set of vectors e_i , $i = 1, 2, \dots$

... d , each representing a deviation $\delta x(t)$ from the orbit $x(t)$. The volume $Vol(\mathbf{e}^d)$ is the volume of the parallelepiped spanned by these vectors, defined as:

$$Vol(\mathbf{e}^d) = \|\mathbf{e}_1 \times \mathbf{e}_2 \times \dots \times \mathbf{e}_d\| \quad (3.6)$$

The symbol " $\|\ \|$ " denotes Euclidean norm in a d -dimensional Euclidean space. The time dependent volume of the parallelepiped is given by:

$$Vol(\mathbf{e}^d, t) = \|\mathbf{U}_{x_0}^t \mathbf{e}_1(0) \times \mathbf{U}_{x_0}^t \mathbf{e}_2(0) \times \dots \times \mathbf{U}_{x_0}^t \mathbf{e}_d(0)\| \quad (3.7)$$

The d -dimensional Lyapunov exponent then defines the average expansion rate of the d -dimensional parallelepiped:

$$\lambda(\mathbf{e}^d, x_0) = \lim_{t \rightarrow \infty} \frac{1}{t} \ln \frac{Vol(\mathbf{e}^d, t)}{Vol(\mathbf{e}^d, 0)} \quad (3.8)$$

If \mathbf{U} is a multiplicative cocycle with respect to T , i.e., if the condition:

$$\mathbf{U}^{t+s}_{x_0} = \mathbf{U}_{x_0}^t \mathbf{U}_{x_0}^s \quad (3.9)$$

is satisfied, then the limit in Eq.(3.8) exists for all \mathbf{e}^d and for almost all initial orbits x_0 ^[7]. The quantity $\lambda(\mathbf{e}^d, x_0)$ is independent of the choice \mathbf{e}^d .^[8] There exists any subset of $Vol(\mathbf{e}^d, t)$. In particular the following limit:

$$\lambda(\mathbf{e}^l, x_0) = \lim_{t \rightarrow \infty} \frac{1}{t} \ln \frac{Vol(\mathbf{e}^l, t)}{Vol(\mathbf{e}^l, 0)} = \lim_{t \rightarrow \infty} \frac{1}{t} \ln \frac{\mathbf{U}_{x_0}^t \mathbf{e}^l(0)}{\mathbf{e}^l(0)} \quad (3.10)$$

is of interest. The Eq. (3. 10) is the definition of the 1-dimensional Lyapunov exponent. There are d different limits for $l = 1, 2, \dots, d$. They can be ordered as:

$$\lambda_1 \geq \lambda_2 \geq \dots \geq \lambda_d \quad (3.11)$$

These are the complete Lyapunov spectrum.

Lyapunov exponents describe the exponential divergence and

convergence of trajectories toward an attractor in a multi-dimensional dynamic flow. These exponents reflect the properties of an attractor by their sign and magnitude. The sum of the exponents is the time-average divergence of the phase space velocity; therefore any dissipative dynamical system will have at least one negative exponent, the sum of all of the exponents is negative. An attractor for a dissipative system with one or more positive Lyapunov exponents is said to be "strange" or "chaotic".

A stable fixed point has all negative exponents. A periodic attractor is characterized by one zero exponent, and the rest of the exponents are negative. A two-frequency quasiperiodic attractor has two zero exponents and negative exponents for the rest. A chaotic attractor has at least one positive exponent indicating the divergence of the trajectories, i.e., the sensitivity with respect to initial conditions. For example, in a three-dimensional continuous phase space a fixed point has spectrum $(-, -, -)$, a periodic limit cycle $(0, -, -)$, a quasiperiodic attractor (torus) $(0, 0, -)$ and a chaotic attractor $(+, 0, -)$. A zero exponent corresponds to the slowly changing magnitude of a principle axis tangent to the flow. The magnitude of the negative exponents quantitatively describes the contraction of the attractor along certain axes in phase space.

The magnitude of Lyapunov exponents measures the rate at which the system processes create or destroy information.^[9] Thus the exponents are expressed in bits of information per second, or bits/orbit for a continuous system and bits for a discrete system. In this dissertation, all the Lyapunov exponents computed from experimental time series are in bits/iteration.

The Lyapunov spectrum is closely related to the fractional dimension of the associated strange attractor. There is a number^[10] of different fractional-like

quantities such as the fractal dimension, information dimension, and the correlation dimension. It has been conjectured by Kaplan and Yorke^[11] that the information dimension d_i is related to the Lyapunov spectrum by the equation:

$$d_i = j + \frac{\sum_{t=1}^j \lambda_t}{|\lambda_{j+1}|} \quad (3.12)$$

where j is defined by the condition that:

$$\sum_{t=1}^j \lambda_t > 0 \quad \text{and} \quad \sum_{t=1}^{j+1} \lambda_t < 0 \quad (3.13)$$

The conjectured relation between d_i and the Lyapunov exponents appears to be satisfied for some model system.^[12]

In most of the experimental situations there are no dynamical equations, therefore no Jacobians \mathbf{A} and fundamental matrix \mathbf{U} available to calculate Lyapunov exponents. Fortunately, from the time series one can reconstruct the attractor, and then estimate a linearized flow map \mathbf{A}' of the tangent space by using a different technique. Experimental data inevitably contain noise due to environment fluctuations and limited experimental resolution. Therefore the ability to obtain good estimates of \mathbf{A} depends largely on the quantity and quality of the data as well as the complexity of the dynamical system. There has been considerable effort to provide algorithms for the determination of the Lyapunov exponents from time series alone^{[13][14][15][16][17]}. In this dissertation the three most popular algorithms developed by Wolf *et al.*^[14], Sano *et al.*^[15], and Bryant *et al.*^[16] were employed.

In Wolf *et al.*'s algorithm^[14] a single vector is chosen between nearby trajectories, and propagated along the attractor. After reaching a certain size

along the system's fiducial trajectory, it is replaced by a new vector with minimal length and most similar orientation. The largest exponent can be estimated reliably and easily, but the other exponents, especially the negative ones, are difficult to obtain because the evolved vectors tend to fall in the direction of strongest divergence. Selection of the embedding dimension and delay time is very important here. It was found that attractors reconstructed using smaller values of m often yield reliable value for the largest Lyapunov exponent, even though it has been suggested^[2] to choose m to be greater than twice the dimension of the underlying attractor to have a good embedding. But when m is too small "catastrophes" that interleave distinct parts of the attractor are likely to result. On the other hand increasing m past what is minimally required will effectively increase the noise level. Therefore it is recommended that the stability of results with m and τ are checked to ensure robust estimates. The amount of the data required to calculate Lyapunov exponents is recommended to be in the range of 10^d to 30^d , where d is the information dimension of the dynamical system.

The basic idea of Sano *et al.*'s algorithm^[15] is to approximate the local tangent space to the attractor by a flow map A_j which is computed by a least-squares method from a number of pseudo-tangent vectors propagated over a certain time span. These vectors are generated from near-by trajectories of the attractor, and serve as an approximation for the true tangent space. Lyapunov exponents can be computed as:

$$\lambda_i = \lim_{n \rightarrow \infty} \frac{1}{tn} \ln \sum_{j=1}^n \|A_j e_i\| \quad (3.14)$$

for $i = 1, 2, \dots, d$, where $\{\mathbf{e}_i^j\}$ ($i = 1, 2, \dots, d$) is a set of basis vectors of the local tangent space. In the numerical procedure, an arbitrary set $\{\mathbf{e}_i^j\}$ was chosen, operated on with matrix \mathbf{A}_j , and renormalized to $\mathbf{A}_j \mathbf{e}_i^j$. The Gram-Schmidt procedure^[18] was then used to maintain orthogonality. This procedure was repeated for n iterations and used to compute the Lyapunov spectrum given by Eq. 3.11. The advantage of this algorithm is that it can compute all of the components to a good accuracy with relative ease. However in some locations of the chaotic attractors flow is very "thin" in certain directions associated with negative exponents. When the local data-set curvature is too large in these locations the linear least-squares method becomes inappropriate. In some cases the reconstructed data are close to degenerate; then a Singular-Value Decomposition technique has to be used to achieve a reasonable result.

Bryant *et al.*'s algorithm^[16] is similar to Sano *et al.*'s except it finds the required Jacobians by making local polynomial maps, allowing for a more accurate determination of \mathbf{A} . The calculation based on this algorithm is quite sensitive to the noise level compared to the above two. But with careful setting of the parameters it can find the negative exponents quite accurately as well as the positive ones.

When only the largest Lyapunov exponent is needed, Wolf's algorithm is always the best choice. It can be easily implemented, and the calculation results are often stable and reliable. This algorithm was used for all three nonlinear dynamic systems described in this chapter and next chapter: driven diode resonator systems (Sec. 3.2), coupled tunnel diode relaxation circuits (Sec. 3.4), and autonomous and externally driven oscillations in n-InSb (Chapter 4).

On the other hand, if one is interested in the complete Lyapunov spectra,

Sano's or Bryant's approach has to be considered. An implementation of Sano's algorithm by Krueel *et al.*^[17] is used in this dissertation for the experiment of diode resonator systems (Sec. 3.2); Bryant's approach was used in the system of electrical oscillations of n-InSb (chapter 4). Krueel's program is stable and fast for most of the experimental data. It can give reasonably accurate estimates for system's complete spectra, but sometimes has difficulty to find good negative exponents. Bryant's program can be used to calculate more accurate negative exponents, but it often takes longer computing time, and fails for some experimental data.

(6) Summary

Several different concepts, which include phase portraits, Poincaré sections, power spectrum and autocorrelation functions, all can be used to identify periodic and quasiperiodic oscillations. They can be also used to separate periodic or quasiperiodic motions from chaotic evolutions. However to quantitatively characterize chaotic attractor, one has to use Lyapunov exponents. Lyapunov exponents are the average exponential rates of divergence or convergence of nearby orbits in phase space. But the orbits in phase space can only be obtained from the equations of the dynamic systems. In real world applications, most of time these equations are not available. Fortunately, from a time series of single system variable, the Takens' embedding reconstruction technique allows one to obtain a phase space diffeomorphic to the original one. In addition, Lyapunov exponent is invariant with respect to diffeomorphic transformation of variables for an infinite amount of noise-free data. In practice, one can use a finite segment of a time series obtained from the experimental

system to give good estimates for the exponents.

3.2 Simulation and Characterization of Nonlinear Dynamics in Driven Diode Resonator Systems

(1) Introduction

Harmonically driven diode resonator systems have been found to exhibit several universal behaviors representing particular routes to chaos. These behaviors include period doubling route to chaos in the single diode resonator system^{[19][20][21]}, and quasiperiodic route to chaos in the coupled diode resonator systems^[22]. However there is still controversy about the modeling of these systems. Testa, Perez, Buskirk and Jefferies^{[23][24]} insisted on that the observed period doubling and chaotic behavior were due to the nonlinearity of the effective capacitance on the diode pn-junctions. They showed that this model gives reasonable qualitative agreement with experiments. On the other hand, Hunt, Rollins and Su^{[25][26][27]} argued that the nonlinear reverse bias capacitance of the pn-junction is not responsible for the behaviors observed, but the rather large reverse recovery time of such diodes was essential here. A third approach^[28] is to employ the well-known *SPICE* program^[29] trying to achieve a maximally realistic modeling of the diode. This model is similar to the model by Testa *et al*^[23] in that both introduce a voltage-dependent differential capacitance. The difference is the model with *SPICE* gives more detailed expressions and realistic parameters corresponding to the particular type of diode. Under some circumstances an accurate and realistic model is very important. For example an accurate model is very useful for complex coupling diode resonator systems that represent a higher dimensional dynamical system.

It is known that high-dimensional line-coupled diode resonator systems can reach the chaotic state via a quasiperiodic route^{[24][27]}. One important theory about this route was put forward by Ruelle, Takens and Newhouse^[30]. In the Ruelle-Takens theory, the sequence of transitions leading to chaos is as follows: fixed point $S \rightarrow$ limit cycle $P \rightarrow$ quasiperiodic with two frequencies $T^2 \rightarrow$ quasiperiodic with three frequencies $T^3 \rightarrow$ chaos. As soon as the third frequency arrives, the broad-band noise characteristic of chaos should start to appear. But as Curry and Yorke pointed out^[31], there is another route to chaos via quasiperiodic regimes, where chaos appears directly from a quasiperiodic regime with two frequencies. In this case, the manifestation of another degree of freedom is not in the form of a third frequency, but rather by the gradual departure of the trajectories from T^2 , which amounts to the destruction of tori (quasiperiodic orbits). The typical transitions to chaos are as follows: periodic $P \rightarrow$ quasiperiodic with two frequencies $T^2 \rightarrow$ periodic locking states $L \rightarrow$ chaos.

In this section, the diode resonator model from *SPICE* is discussed first. Then detailed comparisons between experimental and simulation results on the single diode resonator system are presented. These include wave forms, power spectra, phase portraits, bifurcation diagrams, and Lyapunov exponents. Thirdly, the transitions from quasiperiodic oscillations to chaos in line-coupled systems are shown, in good agreement with the Curry-Yorke model. A comparison of Lyapunov exponents from the experimental time series and simulation model is given to show that the *SPICE* model also accurately describes the coupled systems.

(2) Diode Model from *SPICE*^[29]

A *SPICE* model for a diode pn-junction is composed of an ohmic resistance r_s , an ideal static diode I_D , and an effective capacitance C_D , which reflects the dynamic properties of diode, and is essential for the observed chaotic behaviors (Fig. 3.1).

Static Model of a pn-junction: It is well known that a pn-junction can be modeled as follows:^[29]

$$I = f(V_D) = \begin{cases} I_s(e^{\frac{qV_D}{nkT}} - 1) + V_D G_{MIN} & \text{for } V_D \geq -5 \frac{nkT}{q} \\ -I_s + V_D G_{MIN} & \text{for } V_D < -5 \frac{nkT}{q} \end{cases} \quad (3.15)$$

Here n is the emission coefficient ($1 \leq n \leq 2$), and I_s is the saturation current. A small conductance G_{min} is added in *SPICE* in parallel with pn-junction to aid convergence of numerical integration. The default value for G_{min} is 10^{-12} F.

Charge-storage effects of a pn-junction: There are two forms of charge storage: minority-carrier injection Q_s and the space charge Q_d . The first one results from excess minority carriers injected across the junction in forward bias. This charge is proportional to the total current injected across the junction:

$$Q_s = \tau_D I_D(V_D) \quad (3.16)$$

Where τ_D is called the transit time, which represents the minimum time required to either store or remove the charge.

A second kind of charge is associated with the changing of the space-charge region when V_D changes. It can be given as:

$$Q_D = 2 \phi_0 C_d(0) \sqrt{1 - \frac{V_D}{\phi_0}} \quad (3.17)$$

Here $C_D(0)$ is the diode junction capacitance at zero bias ($V_D = 0$), and ϕ_0 is the junction potential (built-in voltage).

There are two points that can be made on Eq (3.17). First, for reverse bias and small forward bias, Q_D is the dominant stored charge. Second, for moderate forward bias and beyond, the injected charge Q_S dominates. The second observation is important because as V_D approaches ϕ_0 , Eq (3.17) is no longer valid. A more exact analysis of real diode gives the following results. For forward-bias voltage up to about $\phi_0/2$, the values of Q_D are more accurately predicted by Eq. (3.17). For voltage $V_D \geq \phi_0$ a linear extrapolation of Eq. (3.17) can be used to achieve the best simulation result.

Therefore the charge storage element $Q_D = Q_s + Q_d$ can be determined by the following relations:

$$Q_D = \begin{cases} \tau_D I_D + C_D(0) \int_0^{V_D} \left(1 - \frac{V}{\phi_0}\right)^{-m} dV & \text{for } V_D < FC \times \phi_0 \\ \tau_D I_D + C_d(0) F_1 + \frac{C_d(0)}{F_2} \int_{FC \times \phi_0}^{V_D} \left(F_3 + \frac{mV}{\phi_0}\right) dV & \text{for } V_D < FC \times \phi_0 \end{cases} \quad (3.18)$$

the above equation can also be defined equivalently by the effective capacitance relations:

$$C_D = \frac{dQ_D}{dV_D} = \begin{cases} \tau_D \frac{dI_D}{dV_D} + C_D(0) \left(1 - \frac{V_D}{\phi_0}\right)^{-m} & \text{for } V_D < FC \times \phi_0 \\ \tau_D \frac{dI_D}{dV_D} + \frac{C_d(0)}{F_2} \left(F_3 + \frac{mV_D}{\phi_0}\right) & \text{for } V_D < FC \times \phi_0 \end{cases} \quad (3.19)$$

where m is the junction grading coefficient, and FC determines how the depletion capacitance is calculated when the junction forward-biased. Usually FC is set

equal to 0.5, which means linear extrapolation is taken; F_1 , F_2 , and F_3 are SPICE constants whose values are determined as follows:

$$\begin{aligned}
 F_1 &= \frac{\phi_0}{1-m}(1 - (1-FC)^{1-m}) \\
 F_2 &= (1-FC)^{1+m} \\
 F_3 &= 1-FC(1+m)
 \end{aligned}
 \tag{3.20}$$

(3) Results and Discussion

Single diode resonator system: The single diode resonator system is composed of a diode, a resistance, and an inductance in series with an external sinusoidal driving source. Fig. 3.1 shows the schematic diagram of the circuit used in our experiment. The parameters used in this experiment are listed as in Table 3.1.

R	100 Ω
L	100mH
D	1N4004
f	50KHz

Table 3.1 Parameters for a Single Diode Resonator System.

A set of Ordinary Differential Equations (ODE) derived from the model described above are listed as follows:

$$\frac{dl}{dt} = \frac{V_0 \sin \Omega - V - I(R_0 + R_s)}{L} \quad (3.21)$$

$$\frac{dV}{dt} = \begin{cases} \frac{l - I_d}{\tau_d \frac{dI_d}{dV} + C_d(0) \left(1 - \frac{V}{\phi_0}\right)^{-M}} & \text{when } V < FC * \phi_0 \\ \frac{l - I_d}{\tau_d \frac{dI}{dV} + \frac{C_d(0)(F_3 + \frac{M * V}{\phi_0})}{F_2}} & \text{when } V \geq FC * \phi_0 \end{cases} \quad (3.22)$$

$$\frac{d\Omega}{dt} = 2\pi f \quad (3.23)$$

where
$$I_d = I_S \left(\exp \frac{V}{NkT} - 1 \right) + V * G_{\min}.$$

The first thing obtained from the experiment is the wave form of the current signals. Fig. 3.3 and Fig. 3.4 are pictures taken from the oscilloscope. Fig. 3.3 shows wave form of a period-8 signal, and Fig. 3.4 shows a typical chaotic signal. The time series of Fig. 3.4 was captured using a digitizer, and used to calculate the Lyapunov exponents. Brown's algorithm was employed, and a typical run gave the results listed in Table 3.2. Note that the sum of all three components is -2.18, which means the system is dissipative. One positive component, one negative component, and one much smaller compared to the other two indicate that the system has a strange attractor (See Sec. 3.2).

By integrating the simulated equations and plotting their solutions verse time, wave forms of periods 8 (Fig. 3.5) and chaos (Fig. 3.6) are obtained. Note

that Fig. 3.5 and Fig. 3.6 closely resemble Fig. 3.3 and Fig. 3.4, respectively. The complete Lyapunov spectra from the ODE equations for the chaotic regime are also calculated, and the results are listed in Table 3.2. The accumulated error for this calculation is estimated around 1%. Comparing the Lyapunov spectra from experimental time series and simulated equations as in Table 3.2, one can see they are in good agreement.

	Experimental Time Series	Simulated Equations
λ_1	0.56 ± 0.2	0.378
λ_2	0.016 ± 0.01	0.0
λ_3	-2.76 ± 1.5	-3.86
d_f	2.21 ± 0.6	2.098

Table 3.2 Lyapunov Exponents for a Single Diode Resonator System from Both Experimental Time Series and Theoretical Simulated System

Phase portraits were also obtained, as described in Chapter 2, for periods 8 and chaotic oscillations (Fig. 3.7 and Fig. 3.8). In the period-8 phase portrait one can identify 8 different stable curves in the upper right part, although most of the portraits have more than one curves overlapping with each other. Both portraits have a characteristic "hump" near the center of the upper region in the pictures.

From the simulated system, phase portraits for period-8 and chaotic

oscillations were produced, as shown in Fig. 3.9 and Fig. 3.10. These phase plots are obtained by integrating the simulated equations to produce a time series for one system variable (Current I in Fig. 3.1 is used in this dissertation), and then plotting the series versus a certain time delay of the same time series. The time delay was chosen so that the portraits resemble those from experiments. One can see the similarities between the experimental phase portraits and portraits from simulated system, including the characteristic "humps".

Fig. 3.11 and Fig. 3.12 show the power spectra corresponding to period 8 and chaotic oscillations, respectively. Fig. 3.13(a)(b) show the power spectra calculated from simulated system for the same two dynamical regimes.

A bifurcation diagram from the experimental diode system is shown in Fig. 3.14. It shows period doubling, chaos, band merging, windows of period 5 and period 3, and hysteresis. This is the simplest type of bifurcation diagram observed, and it is displayed by different diode systems with variety of element parameters and diode types, provided that the driving frequency f is close to the resonance frequency for that diode f_{res} .

The bifurcation diagram from the simulation was obtained as follows. For different driving amplitudes, the equations were integrated first. Then, a certain amount of the consecutive peaks values of the current variable (usually around 500 peak values in our simulations) were picked and stored. Plotting those peaks values versus their driving amplitude gave the bifurcation diagram as shown in Fig. 3.15, Fig. 3.16, and Fig. 3.17 (See Sec. 2.2). Figures 3.16 and 3.17 are enlarged diagrams showing some of details of Fig. 3.15. Compared to Fig. 3.14 of the experimental bifurcation diagram, these bifurcation diagrams has

period doubling, chaos, band merging, windows of periods 5 and periods 3, hysteresis, *etc.* One can notice that all the transitions to chaos in this diagram are going through period doubling route.

Line-coupled diode resonator systems: A two-line-coupled diode resonator system consists of two parallel, single diode resonators coupled through a series of a resistor and a conductor as shown in Fig. 3.18. Many different sets of parameters in these line-coupled diode resonator systems were experimented, and in most cases similar results have been obtained. A typical set of parameters used in the experiments are listed as in Table 3.3.

$R_1 \text{ \& } R_2$	100 Ω
$L_1 \text{ \& } L_2$	100mH
$D_1 \text{ \& } D_2$	IN4007
f	53.21KHz

Table 3.3 Parameters for a Line-Coupled Diode Resonator System

A set of Ordinary Differential Equations can be derived from the *SPICE* model as follows:

$$\frac{dl}{dt} = \frac{V_0 \sin \Omega - V_1 - I(R_0 + R_s)}{L} \quad (3.24)$$

$$\frac{dl_1}{dt} = \frac{V_0 \sin \Omega - 2V_1 + V_2 - I_1(R_0 + R_s)}{L} \quad (3.25)$$

$$\frac{dV_1}{dt} = \begin{cases} \frac{I_1 - I_{d1}}{\tau_d \frac{dI_{d1}}{dV_1} + C_d(0)(1 - \frac{V_1}{\phi_0})^{-M}} & \text{when } V_1 < FC * \phi_0 \\ \frac{I_1 - I_{d1}}{\tau_d \frac{dI_{d1}}{dV_1} + \frac{C_d(0)(F_3 + \frac{M * V_1}{\phi_0})}{F_2}} & \text{when } V_1 \geq FC * \phi_0 \end{cases} \quad (3.26)$$

$$\frac{dV_2}{dt} = \begin{cases} \frac{I - I_1 - I_{d2}}{\tau_d \frac{dI_{d2}}{dV_2} + C_d(0)(1 - \frac{V_2}{\phi_0})^{-M}} & \text{when } V_2 < FC * \phi_0 \\ \frac{I - I_1 - I_{d2}}{\tau_d \frac{dI_{d2}}{dV_2} + \frac{C_d(0)(F_3 + \frac{M * V_2}{\phi_0})}{F_2}} & \text{when } V_2 \geq FC * \phi_0 \end{cases} \quad (3.27)$$

$$\frac{d\Omega}{dt} = 2\pi f \quad (3.28)$$

where: $I_{d1} = I_S(\exp^{\frac{V_1}{NkT}} - 1) + V_1 * G_{\min}$ and $I_{d2} = I_S(\exp^{\frac{V_2}{NkT}} - 1) + V_2 * G_{\min}$.

In these coupled diode resonator systems, two different transitions have been found: the first one is the conventional period-doubling bifurcation route, just like the transitions to chaos in the single diode resonator systems; the second one however follows quasiperiodic oscillations, and was called Hopf bifurcation scenario.

One typical transition to chaos is described as follows. For an increasing amplitude of the driving signal with fixed frequency $f_0 = 53.21$ KHz the following sequence has been observed. (1) For $V_0 \leq 6.07V$ the system resides on a simple stable limit cycle with frequency equal to the driving frequency f_0 as shown in Fig. 3.19(a), (these are period-one "oscillations" of the system). (2) For $6.07V \leq V_0 \leq 9.87V$ the system has a quasiperiodic attractor (two-dimensional torus) as shown in Fig. 3.19(b). (3) For $9.87V \leq V_0 \leq 10.50V$ the system appears to be chaotic. (4) The chaotic regime is followed by clear period-three stable oscillations which occur for $10.50V \leq V_0 \leq 13.00V$. The Poincaré section and phase portrait of the system, is represented by three bright dots in Fig. 3.20(a). (5) Further increase in the amplitude of the driving signal, when $13.01V \leq V_0 \leq 14.21V$, brings the system again to a different two-frequency quasiperiodic attractor, with intermittent period three windows as shown in Fig. 3.20(b). Poincaré sections of these tori consist of three nearly circular closed curves, centered on the three dots of the periodic orbit as in Fig. 3.20(a). The radii of the circles grow rapidly with increasing amplitude of the driving signal. The power spectrum of this regime is shown in Fig. 3.21, where one can identify the fundamental frequency f_0 and another incommensurate frequency f_1 with all other frequencies occurring at linear combinations of f_0 and f_1 with rational multipliers. The value of f_1 slowly increases with an increase of the amplitude V_0 . (6) For yet higher driving amplitudes, $14.25V \leq V_0 \leq 15.31V$, frequency locked states were observed. Fig. 3.20(c) shows a typical frequency locked state with an orbit of high period residing on the torus. The Poincaré section initially consists of three groups of dots falling on nearly circular closed curves. These closed curves deformed away from circles with increasing V_0 . The power

spectrum shown in Fig. 3.22 shows that all peaks occur at frequencies $(p/q)f_0$ where p and q are integers and a particularly strong peak is observed at the period-3 positions. The frequency locking ratio is $f_0 / f_1 = 33/3$. (7) Finally with further increase of the driving voltage, $15.40V \leq V_0 \leq 16.20V$, again the chaotic regime is reached as shown in Fig. 3.20(d). The attractor still bears resemblance to that in the quasiperiodic regime, but the presence of wrinkles and corrugations indicates that folding is taking place. Broad band features, seen in the power spectrum with period-3 windows, is shown in Fig. 3.23. This sequence of transitions is in agreement with the Curry-Yorke scenario^[6].

Additional evidence for the existence of chaotic and quasiperiodic regimes can be provided, as usual, by Lyapunov spectra. Kruel and Eisworth^[12]'s algorithm has been used to calculate Lyapunov exponents in this dynamical system. Guided by the dimensionality of the phase space of the SPICE simulated model, $d = 5$ was selected as embedding dimensions for line coupled systems. Data series obtained from these systems are well behaved, and singular-value decomposition is unnecessary. The obtained spectra of a line coupled system for typical quasiperiodic and chaotic regimes are listed in Table 3.4. As emphasized by Kruel and Eisworth^[12], reliable exponents' estimates must be stable in all parameters which enter the program. The two most important parameters are ϵ_{\max} , the maximum distance to locate the neighbors, and t_{evolv} , the evolution time. The exponents listed in Table 3.4 have plateaus when ϵ_{\max} is in the range of $[0.01, 0.08]$ and t_{evolv} in the range $[0.5 \times 10^{-6}, 9.0 \times 10^{-6}]$. The maximum variations of the exponents with respect to the above two parameters are entered as the error estimates. The other two algorithms developed by Wolf *et al.*^[14] and by Bryant *et al.*^[16] were used for the same time series. The positive

exponents of the chaotic regimes and the largest negative exponents were all in qualitative agreement.

	Experimental Time Series	Simulated System
Quasiperiodic regime	-0.0038 ± 0.0002	0.00
	-0.0038 ± 0.0006	-0.00175
	-0.14 ± 0.015	-0.100
	-0.82 ± 0.2	-3.25
	-4.0 ± 1.5	-3.27
Chaotic Regime	$+0.13 \pm 0.02$	+0.0876
	-0.0017 ± 0.00015	0.00
	-0.45 ± 0.08	-0.4
	-1.28 ± 0.17	-3.06
	-5.96 ± 2.0	-3.42

Table 3.4 Complete Lyapunov spectra of a quasiperiodic regime and a chaotic regime calculated from both experimental time series and *SPICE* simulated equations (Eqs. 3.24-3.28) for line-coupled diode resonator system.

Less difficult, but by no means trivial, are calculations of the complete Lyapunov spectra for a simulated model system. In particular, error bars for

calculated values are difficult to estimate and the obtained values show variations for changing parameters of the algorithm. After numerical integration of these equations using Runge Kutta's method for the line coupled diode system, an identical sequence of transitions have been found, *i. e.* periodic solution \rightarrow quasiperiodic solution $T^2 \rightarrow$ frequency locked state \rightarrow chaotic state, occurs. Lyapunov spectra calculations based on this model are listed in Table 3.4, for comparison with those obtained from the experimental time series. The error for this calculation is around 10^{-3} . One can see a very good agreement between the estimated exponents from the experimental data and those calculated from simulated system.

Bifurcation diagrams from simulation system of Eq. 3.24-3.28 were shown in Fig. 3.24 and Fig. 3.25. One interesting thing about this bifurcation diagram is that at the critical point of the Hopf bifurcation in Fig. 3.24, the convergence rate is very slow as theory indicated. Therefore it took extremely long computing times to locate the critical position. One can compare bifurcation diagram Fig. 3.24 from the simulation to the Fig. 27 of Ref. [24], which is a bifurcation picture for a two-coupled diode resonator system. The two bifurcation diagrams have many similarities, *e.g.* Hopf bifurcation, period doubling, periodic locking, chaos, *etc.*

To compare the simulation model and its experimental systems for higher dimensional line-coupled resonators, a phase plot was obtained for the chaotic regime of a four line-coupled diode resonator system (Fig. 3.26). One can compare this with the corresponding phase plot from experiment as shown in Fig. 3.33(a).

(4) Conclusions

The single diode resonator system displays a typical period doubling cascade and transitions to chaos. Experimentally the wave form, phase portrait, and power spectra can be used to study the periodic oscillations and to delineate between the periodic states and chaotic states. But only the Lyapunov exponents can quantitatively describe the chaotic attractor. The model derived from *SPICE* program is capable of simulating the system quite accurately, as shown by good agreement for experimental observables including the wave form, phase portrait, power spectra, bifurcation diagram, and more importantly by the agreement of Lyapunov exponents.

Comparing to the single diode resonator systems, the line coupled system can follow a quasiperiodic route to chaos, in addition to the period doubling route. More accurately, the transitions to chaos for these systems agree with Curry-Yorke model very well, that is: periodic states $P \rightarrow$ quasiperiodic states with two frequencies $T^2 \rightarrow$ periodic locking states $L \rightarrow$ chaos. The simulation model for line-coupled system derived *SPICE* gives consistent results. In addition, Lyapunov exponents calculated from experimental time series and simulation system are in good agreement for both quasiperiodic regimes and chaotic regimes.

Diode resonator systems are simple, yet they can display varieties of interesting nonlinear dynamics features: period doubling, band merging, windows of period-5 and period-3, hysteresis, quasiperiodic states, periodic locking states, and Hopf bifurcation to chaos. The last three features are associated with higher dimensional systems (usually higher than 3).

The line-coupled systems are higher dimensional systems. For example,

for two line-coupled system $d = 5$, and for three line-coupled system $d = 7$. So for every branch added to the system two extra freedom are added to the dynamical systems. Therefore these simple systems provide ideal test ground for the more complex dynamical system experiments. One example is to explore the possibility to stabilize unstable orbits in a chaotic attractor, as described in Sec. 3.3 of this dissertation.

3.3 Stabilization of Periodic and Quasiperiodic Oscillations in Diode Resonator Systems

(1) Introduction

The idea of stabilizing high-period orbits in a chaotic system was first coined by Ott, Grebogi, Yorke^[32] (OGY). As is well known^[41], a typical chaotic attractor contains infinitely many unstable periodic orbits of all periods. In the original paper by OGY^[32] it was proposed that an unstable orbit can be stabilized by small and carefully chosen perturbations in an accessible system parameter. These perturbations "turn-on" when the system begins to move away from unstable orbit along the unstable manifold. Shortly afterwards, several experimental chaos control schemes were reported^{[33][34][35][36][37]}, which converted chaotic motions into stable period-1 and period-2 oscillations by a proportional feedback technique. Hunt^[38] modified this method and applied it to a single diode resonator system. He stabilized periodic orbits up to period-23 on a typical chaotic attractor. More recently, Fillie, Grebogi and Ott^[39] pointed out the possibility of stabilization of periodic orbits from chaotic attractor that has more than one unstable eigendirection. So far, most of the experiments were done on

the most simple chaotic attractors, namely, three-dimensional dynamic system, and researchers are only considered controlling a chaotic attractor to a periodic state.

To understand the details of chaos stabilization and explore the possibility of stabilizing more complex dynamical systems, a stabilization circuit based upon the so-called proportional feedback technique was designed and built. By applying this circuit to both single diode resonator systems and line-coupled diode systems, one not only can stabilize a chaotic attractor to a periodic oscillation as high as period-17, but also obtain quasiperiodic orbits from the line-coupled diode resonator systems.

(2) Experimental Results and Discussions

Single diode resonator system: Fig. 3.27(a) is a picture showing the wave forms before employing the control feedback, in which the top trace is the chaotic signal, and the bottom one is the control feedback signal. After turning on the control and adjusting the control parameters, the result shown in Fig. 3.27(b) was obtained, where the system becomes period-2 oscillation. It is interesting to note that the control feedback back signal becomes erratic when the stabilization of the resonator is obtained. By careful tuning the control parameters, a stabilized period-6 oscillation from the same chaotic attractor was obtained, as shown in Fig. 3.27(c). The stabilization of higher-period orbits is more difficult (more precise control parameter tuning required), though periodic orbits up to the period 17 can be stabilized. These results confirm those obtained by Hunt with somewhat different single diode circuit and control circuit.

Line coupled diode resonator system: For the line-coupled diode resonator

system, it was found that the stabilization of high period orbits is typically easier than the single diode system. What is more important, careful stabilization allows one to restore some of the quasiperiodic orbits with two incommensurate frequencies. Fig. 3.28(a) is the phase plot and Poincaré section of a typical chaotic attractor, Fig 3.28(b) shows the phase plot and Poincaré section of the same system stabilized from chaotic attractor Fig. 3.28(a). One can see that its phase plot is a winding torus, and its Poincaré section consists of two circles, which are indications of quasiperiodic oscillations. In addition, a periodic locked state from the same attractor has been obtained by adjusting the control circuit. Fig. 3.28(c) shows the phase plot and Poincaré section of this periodic locked state. By counting the dot of its Poincaré section, a locked ratio of $22/2$ is obtained. The above stabilization results can be confirmed by their power spectra. Figures 3.29, 3.30 and 3.31 show the power spectra corresponding the chaos of Fig. 3.28(a), quasiperiodic oscillation of Fig. 3.28(b), and periodic locked state of Fig. 3.28(c).

The same control technique was also applied to a line coupled system consisting of four single diode resonators. This system, as shown in Section 3.3, has periodic, quasiperiodic and chaotic regimes. The stabilization of periodic and quasiperiodic orbits was also found to be possible, as shown in Fig. 3.32 and Fig. 3.33.

The above stabilization results were also possible for a variety of line-coupled diode resonator systems with different elements (resistors and inductors) as well as diode types.

The control signals in the experiments described above were always small when compared to the system signals (less than 5%). Unfortunately, a simple

operational recipe for the stabilization for all of the observed orbits within the Hunt's technique was not found. Both high periodic and apparently quasiperiodic orbits are equally difficult to stabilize, and there was not any specific difference in the stabilization procedures for orbits of these two types. The orbits classified as quasiperiodic appeared less often than the periodic ones, as may be expected. A word of comment should be added on the observed quasiperiodic orbits. Obviously, a strictly quasiperiodic orbit is an experimental and simulational impossibility (all measured frequencies are commensurate, all simulated orbits are ultimately periodic). Additionally, a high periodic orbit perturbed by a small amount of noise residing on a torus will behave as an almost periodic orbit, which can be well approximated by a quasiperiodic orbit. In this situation, an experimental observation of quasiperiodicity must first localize tori on which these orbits may live, and secondly provide an example of an orbit which appears dense on this torus. All of the high period orbits stabilized clearly belong to some common tori, similar to those observed in the system before the transition to chaos. Additionally, orbits of period as high as 17 are still classified as such, which indicates the relatively low noise level in the system.

It was well known that a typical attractor has embedded within it an infinite number of unstable periodic orbits^[40]. Based on the experiments described above it is conjectured that the chaotic attractors for systems considered in this section contain both unstable periodic and unstable quasiperiodic orbits. These quasiperiodic orbits within a chaotic attractor could provide another invariant set besides the unstable periodic orbits used in characterization of complex fractal structure of strange attractors^[41].

(3) Conclusions

By applying the stabilization circuit to single diode system, periodic orbits up to period 17 from a typical chaotic attractor were successfully stabilized. More interestingly, for the line-coupled diode systems not only were high periodic oscillations obtained easily, but quasiperiodic orbits were also stabilized. Theoretically, this raises a serious question: Does there exist any unstable quasiperiodic orbits in addition to the well-known unstable periodic orbits? On the other hand, these results and techniques directly aid in the investigation of the stabilization of laser arrays, which is higher dimensional system, and its stabilization has potential applications in the laser manufacturing industry^[42].

3.4 Synchronization of Chaos in Coupled Tunnel Diode Relaxation Oscillators

(1) Introduction

Recently, synchronization of chaos has been found in several different dynamical systems: coupled lattice maps (Kaneko^[43]), dynamical systems driven by a common "master system" (Pecora and Carroll^[44]), and finally systems of coupled "virtual" chaotic nonlinear oscillators which for some values of the coupling parameters produce synchronized auto-oscillations ranging from periodic to chaotic (Kowalski *et al.*^[45]). The study of synchronized chaos is important not only as a model for nonlinear systems with many degrees of freedom, but also from the view point of biological information processing and possible engineering applications. For example, the synchronized chaos circuit might be used for a military communication system^[46]. In this section, experimental observations^[47] of synchronization to a common chaotic orbit in a

coupled relaxation oscillator system through weak coupling are presented.

(2) Circuit layout and dynamical equations

Fig. 3.34 shows a basic relaxation circuit in which there are two branches connected in parallel. Each branch contains a nonlinear element tunnel diode, and two linear elements consisting of a resistance and an inductance. For any real tunnel diode there is an effective capacitance associated with it in addition to the ideal tunnel diode. This circuit is a simplified version of a circuit proposed earlier^[48] where two branches were coupled by a resistor R . With this coupling the circuit can display much more complex dynamics. But even for $R = 0$ the two branches remain coupled due to the finite internal resistance of the voltage source, and therefore some common periodic and chaotic regimes can still be observed. The reason for choosing $R = 0$ is to simplify the system to study the coupling behavior of several such relaxation units. Fig. 3.35 shows a circuit of two coupled relaxation oscillators. The typical values of the circuit elements are listed in **Table 3.5**. The coupling resistance was chosen as $R_c = 50\text{k}\Omega$. The tunnel diodes used were purchased from Custom Components, Inc. P/N 151100G. Two separate power supplies were used to drive the two units. The voltage signals were taken at points A and B by using high impedance buffer amplifiers to minimize external perturbations to the circuit. As with the other nonlinear dynamic experiments, the signals can be displayed on a digital oscilloscope or digitized by using 10MHz 8-bit sampler and stored in the computer. The frequency spectra were obtained using Hewlett-Packard 3585A spectrum analyzer.

$R_1 = 1.35\Omega$	$R_3 = 1.51\Omega$
$R_2 = 1.20\Omega$	$R_4 = 1.25\Omega$
$L_1 = 220.0\mu H$	$L_3 = 270.0\mu H$
$L_2 = 180.0\mu H$	$L_4 = 220.0\mu H$
$R_w = 1.0\Omega$	$R_w' = 1.0\Omega$

Table 3.5 Parameter Values of a Coupled Tunnel Diode Oscillator systems

The dynamics of a single relaxation unit can be described by:

$$L_k \frac{dI_k}{dt} = V - I_k R_k - V_{dk} \quad k=1,2 \quad (3.29)$$

$$V + (I_1 + I_2)R_w = \varepsilon \quad (3.30)$$

$$C_k \frac{dV_{dk}}{dt} = I_k - f_k(V_{dk}) \quad k=1,2 \quad (3.31)$$

where ε is the applied bias voltage, V_{dk} and I_{dk} are the voltages and currents, respectively, in the k -th tunnel diode, f_k is the current-voltage characteristic of the k -th diode, which is well approximated by a cubic polynomial, C_k are the small effective diode capacitances which are essential for the generation of relaxation oscillations, and R_w is the internal resistance of the voltage source. The system described by the four equations given above (Eq. (3.29) & Eq. (3.31)) represents a pair of relaxational Van der Pol type oscillators with linear coupling via slow variables (Eq.(3.30)). These systems were originally considered as hardware models of coupled Fitzhugh-Nagumo neuromimes^[49] with fast voltage variable

representing the membrane potential and the current modeling the slow "recovery" variable.

(3) Experimental results

In the many different decoupled units both periodic and aperiodic behavior have been observed. It is well known that two such similar units in periodic regimes residing on stable limit cycles with close frequencies may synchronize in the presence of weak coupling to a common periodic orbit. Even more interesting is the possibility of synchronization of two weakly coupled chaotic attractors. Fig. 3.36(a) shows an oscilloscope picture of periodic synchronized diode voltages near the start of auto-oscillations. Fig. 3.36(b) shows the corresponding power spectra. Fig. 3.37(a) shows two unsynchronized chaotic diode voltages when the units are uncoupled and when a slightly smaller bias voltage is applied to one of the units than in Fig. 3.36(a). Fig. 3.37(b) shows synchronized chaotic pulses when the units are coupled via resistor R_C for the same experimental conditions as Fig. 3.37(a). Fig. 3.38 shows the power spectra for the synchronized chaotic pulses. Fig. 3.39(a) shows synchronized chaotic signals for qualitatively different behavior with shorter time intervals between pulses when slightly larger bias voltage is applied than in Fig. 3.37(b). Fig. 3.39(b) shows the corresponding chaotic power spectra. The synchronization can be observed over long periods of time by digitizing the signals and displaying them on a computer, as shown in Fig. 3.40 for the experimental conditions of Fig. 3.37(b). The synchronization in Fig. 3.40 is observed at each pulse as the pulses form bursts.

The observed synchronization is only the simplest result of two similar

chaotic attractor interactions, similar to the case of two coupled limit cycles. The "frequency-locked entrainment" states of two chaotic attractors have also been observed when one of the units is modified. This behavior is shown in Figs. 41(a)-(b) for 2/3 entrainment, that is every two peaks in the top trace are entrained with every three peaks in the bottom trace. This clearly is a interesting phenomenon falling in between synchronization with strong coupling and unsynchronization with weak coupling. The experimental circuit to observe this behavior is that of Fig. 3.35 with the addition of a coupling resistance R of 16Ω between the two branches of Unit 1, as in the scheme of Gollub *et al.* A wide range of entrained chaos and synchronized chaos was observed as a function of R .

To make sure that such units did not act as "noise amplifiers", one has to study the experimental time series in terms of Lyapunov spectra. By using Takens' embedding technique and the algorithm of Wolf *et al.* the principal Lyapunov exponent was estimated. A stability analysis was made of the time series shown in Fig. 3.38(a) and Fig. 3.40. The number of data points is 30, 000, and was sampled at a rate of 5MHz. The evolution time of the Wolf algorithm was varied for both signals and the resultant calculated exponents are shown in Fig. 3.42(a)-(b). The variation in the calculated principal exponent with respect to maximum replacement distance was examined for several parameter values. In these instances, changing the maximum replacement distance from 10 percent to 5 percent of the lateral extent of the embedding changed the calculated principal exponent by at most 10 percent. These calculations suggest a principal Lyapunov exponent of 50×10^3 (bits/s) for the time series of Fig. 3.38(a) and 70×10^3 (bits/s) for time series of Fig. 3.40. The positivity of the

exponent and its degree of stability with respect to changes in the evolution time are consistent with a chaotic voltage train, which has around 40 KHz oscillations; so the signal will lose almost all of the information within one cycle.

(4) Conclusions

Through a weak coupling, the simple system of Fig. 3.35 shows mutual entrainment of two chaotic relaxation oscillators. This is first time that the synchronization of chaos has been observed in the coupled tunnel diode systems. This result also experimentally confirm the idea of synchronization in chaotic systems, which was proposed by Pecora and Carroll^[44]. In addition, the "frequency-locked entrainment" states of two chaotic attractors have also been observed when appropriate coupling is applied. Large communities of interacting chaotic relaxational units would be worthy of further investigation. In addition numerical simulations for a model of the coupled units shown in Fig. 3.35 will also be interesting to confirm the synchronization phenomena.

CHAPTER 3 REFERENCES

1. Pierre Berge, Yves Pomeau, and Christian Vidal. *Order within Chaos: Towards a deterministic approach to turbulence*. (John Wiley & Sons 1984).
2. F. Takens, "Detecting Strange Attractors in Turbulence." in: *Lecture Notes in Mathematics* No. **898**, (Springer, Berlin, 1981) p. 366.
3. Andrew M. Fraser, *Physica* **34D** 391(1989).
4. D.S. Broomhead and Gregory P. King, *Physica* **20D** 217(1986).
5. P.S. Landa and M.G. Rosenblum, *Physica* **48D** 232(1991).
6. S. N. Rashband, *Chaotic Dynamic of Nonlinear Systems* (John Wiley & Sons 1990).
7. Oseledec, V. I., *Trans. Moscow Math. Soc.* **19**, 197(1968).
8. G. Benettin, L. Galgani, A. Giorgilli, and J.-M. Strelcyn, *Meccanica* **15** 9(1980).
9. R. Shaw. "Strange Attractors, Chaotic Behavior, and Information Flow." *Z. Naturforsch.* **36A**, 80(1981).
10. J.D. Farmer, E. Ott and J.A. Yorke, "The Dimension of Chaotic Attractors," *Physica* **7D**, 153(1983).
11. J. Kaplan and J. Yorke, "Chaotic behavior of multi-dimension difference equations." in: *Functional Differential Equations and the Approximation of Fixed Points. Lecture Notes in Mathematics*, Vol. **730**. H.O. Peitgen and H.O. Walther. eds. (Springer, Berlin). p. 228.

12. D.A. Russel, J.D. Hanson and E. Ott. Phys. Rev. Lett. **45**, 1175(1980).
13. J.-P. Eckmann, S.O. Kamphorst, D. Ruelle, and S. Ciliberto, Phys. Rev. **A 34**, 4971(1986).
14. A. Wolf, J. B. Swift, H. L. Swinney, and J. A. Vastano, Physica **16D**, 285(1985).
15. M. Sano and Y. Sawada, Phys. Rev. Lett. **55**, 1082(1985).
16. P. Bryant and R. Brown, Phys. Rev. Lett. **65**, 1523(1990).
17. Th.-M. Kruel, M. Eiswirth and F.W. Schneider, Physica **63D**, 117(1993).
18. See for example: C. Phillips and B. Cornelius *Computational Numerical Methods*, (Ellis Horwood Limited, 1986) p.174
19. P. S. Linsay, Phys. Rev. Lett. **47**, 1349(1981).
20. J. Testa, J. Perez, C. Jefferies, Phys. Rev. Lett. **48**, 714(1982).
21. J. Perez, Thesis, UC Berkeley. R. W. Rollins and E. R. Hunt, Phys. Rev. Lett. **49**, 1295(1982).
22. Z. Su, R.W. Rollins, and E.R. Hunt, Phys. Rev. **A 36**, 3515(1987).
23. J. Testa, J.M. Perez, C. Jefferies, Phys. Rev. Lett. **49**, 1055(1982)
24. R. Van Buskirk and C. Jefferies, Phys. Rev **A 31**, 3332(1985).
25. E. R Hunt, Phys. Rev. Lett. **49**, 1054(1982).
26. R. W. Rollins and E. R. Hunt, Phys. Rev. Lett. **49**, 1295(1982).
27. Z. Su, R. W. Rollins and E. R. Hunt, Phys. Rev. **A 40**, 2698(1989).
28. Z. Yu, J. Steinshnider, C.L. Littler, J.M. Perez, J.M. Kowalski, Phys. Rev **E 49**, 220(1994).

29. *SPICE*, Department of Electrical Engineering and Computer Sciences, U. C. Berkley. See also Paolo Antognetti and Giuseppe Massobrio, *Semiconductor Device Modelling with SPICE*. (McGraw-Hill, New York, 1988).
30. S. Newhouse, D. Ruelle, T. Takens, "Occurrence of strange axiom-A attractors near quasiperiodic flows on T^m , $m \geq 3$ ", *Communications in Mathematical Physics*, **64**, p.35(1978).
31. J. Curry, J. A. Yorke, "A transition from Hopf bifurcation to chaos: computer experiments with map in R_2 " in *The Structure of attractors in dynamical systems, Springer Notes in Mathematics*, **668**, p. 48, Springer-Verlag (1977).
32. Edward Ott, Celso Grebogi, and James A. Yorke, *Phys. Rev. Lett.* **64**, 1196 (1990).
33. W. L. Ditto, S. N. Rauser, and M. L. Spano, *Phys. Rev. Lett.* **65**, 3211 (1990).
34. J. Singer, Y-Z. Wang, and H. H. Bau, *Phys. Rev. Lett.* **66**, 1123 (1991),
35. A. Azevedo and S. M. Rezende, *Phys. Rev. Lett.* **66**, 1342 (1991).
36. Y. Braiman and I. Goldhirst, *Phys. Rev. Lett.* **66**, 2545 (1991)
37. R. Lima and M. Pettini, *Phys. Rev.* **A41**, 726 (1990).
38. E. R. Hunt, *Phys. Rev. Lett.* **67**, 1953 (1991).
39. Fillie, Grebogi, Ott, *Physica*. **58D**, (1992).
40. C. Grebogi, E. Ott, and J. Yoeke, *Phys. Rev.* **A37**, 1711(1988).
41. G. H. Gunarante, P. S. Linsay and M. J. Vinson, *Phys. Rev. Lett*, **63**, 1(1989).

42. R. Roy, T.W. Murphy, Jr., T.D. Maier, Z. Gills, and E.R. Hunt, *Phys. Rev. Lett.* **68**, 1295(1992).
43. K. Kaneko, *Phys. Rev. Lett.* **63**, 219(1989); **65**, 1391(1990); *Physica* **D41**, 139(1990).
44. L.M. Peroca, R.L. Carroll, *Phys. Rev. Lett.* **64**, 821(1990).
45. J.M. Kowalski, G.L. Albert and G.W. Gross, *Phys. Rev.* **A42**, 6260(1990);
J.M. Kowalski, G.L. Albert, B.K. Roades and G.W. Gross, *Neural Networks* **5**, 805(1992).
46. W. L. Ditto and L.M. Pecora, *Scientific American*, **78**, August, 1993.
47. J.M. Perez, Z. Yu, J.M. Kowalski, G. Albert, C.L. littler and X.N. Song, "Synchronization of Chaos in Coupled Tunnel Diode Relaxation Oscillators", **Proceedings of the 1st Experimental Chaos Conference**, Arlington, VA, Oct. 1991 (*World Scientific, Singapore, 1992*).
48. J.P. Gollub, E.J. Romer, J.E. Socolar, *J. Stat. Phys.* **23**, 321(1980).
49. R. Fitzhugh, *Mathematical Models of Excitation and propagation in Nerve*, in *Biological Engineering*, edited by H.P. Schwan, (McGraw-Hill, New York, 1968).

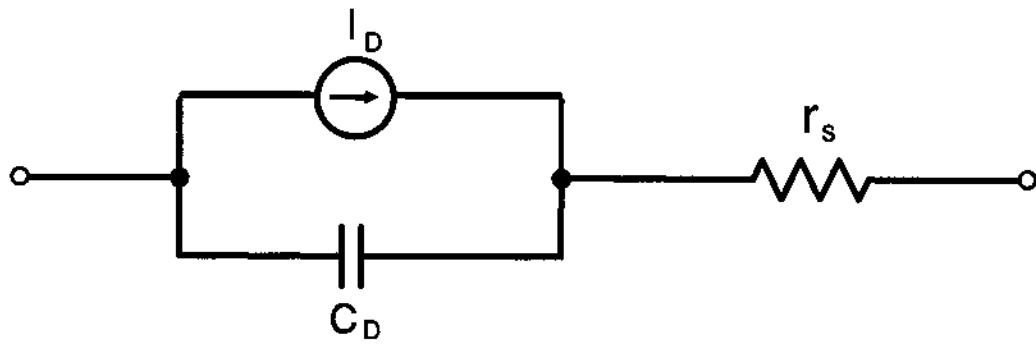


Figure 3.1 Schematic diagram of a diode model in *SPICE*.

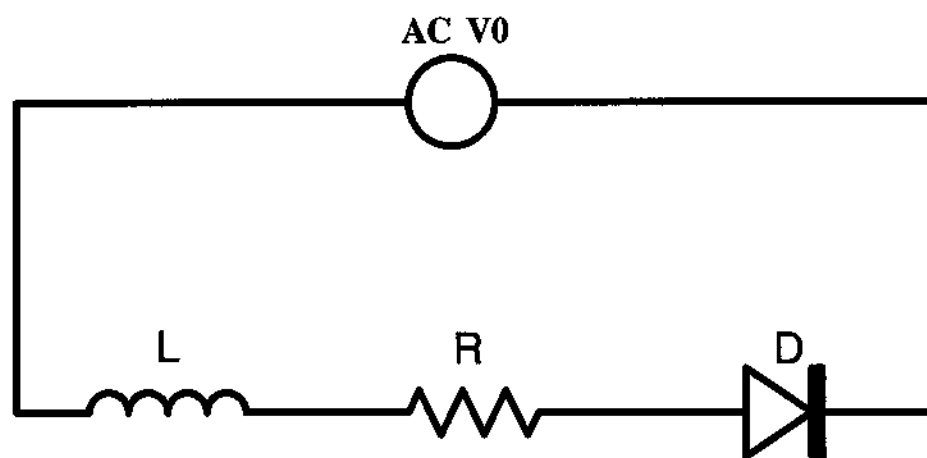


Figure 3.2 Circuit of a single diode resonator system.

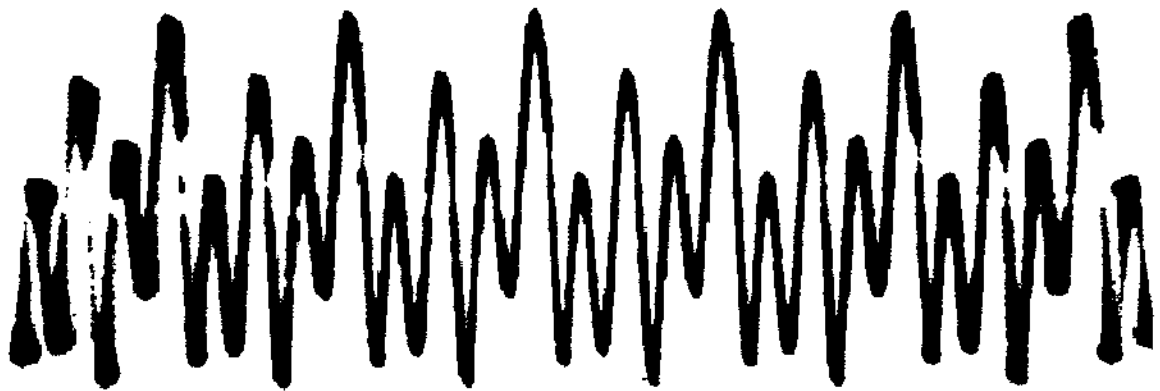


Figure 3.3 Picture taken from a oscilloscope showing the wave form of period-8 oscillations in a single diode resonator system.



Figure 3.4 Picture taken from a oscilloscope showing the wave form of chaotic oscillations in a single diode resonator system.

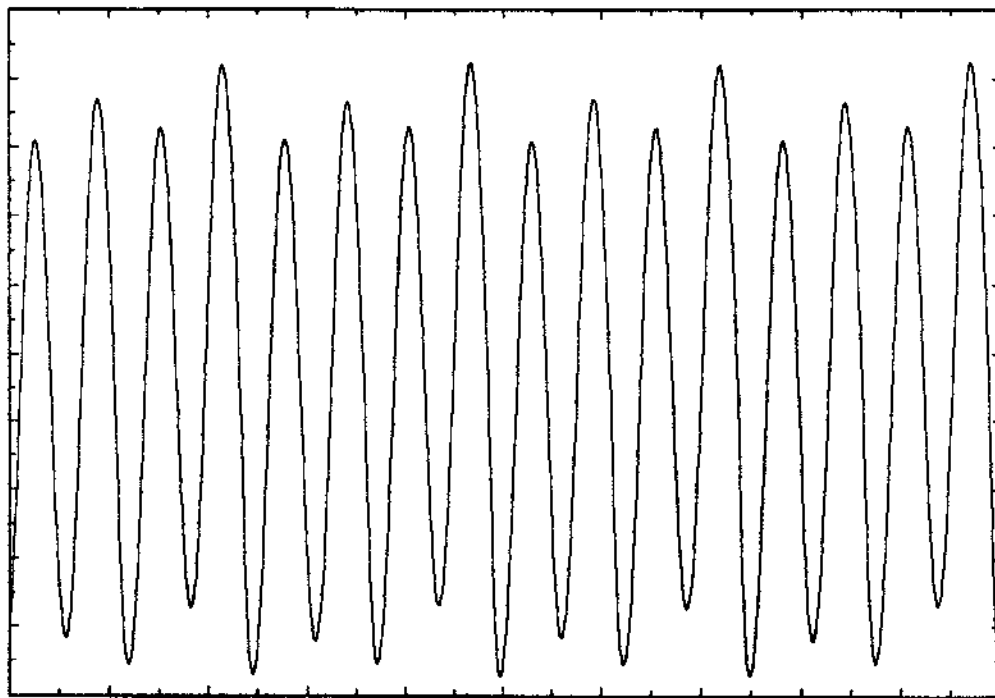


Figure 3.5 Wave form of period-8 oscillation obtained from simulated system of single diode resonator. Vertical axis is current I through the system and horizontal axis is time t .

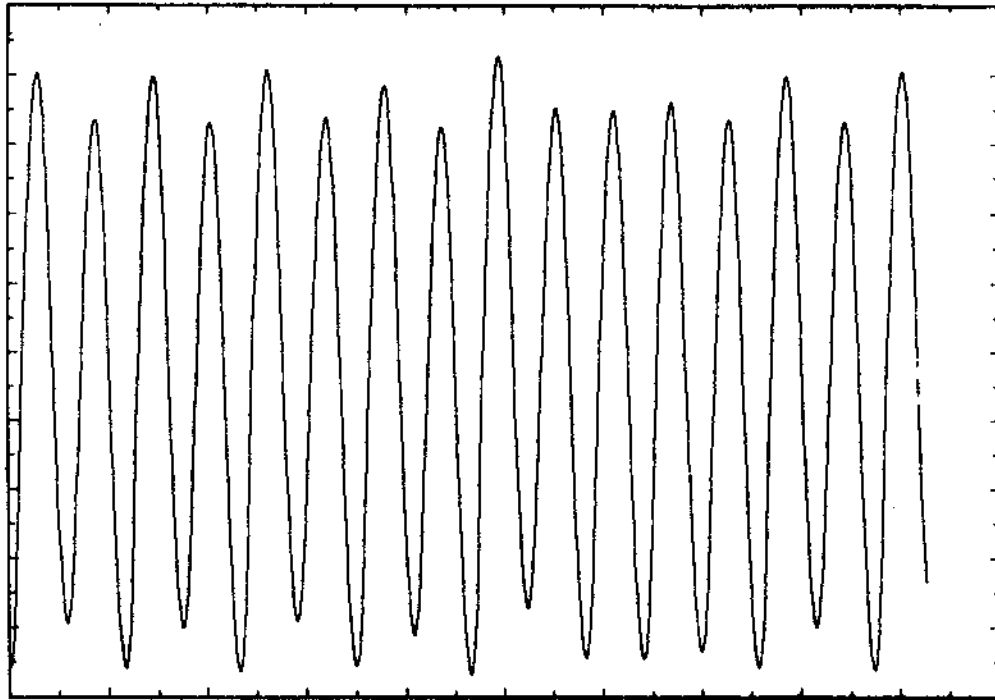


Figure 3.6 Wave form of chaotic oscillation obtained from simulated system of single diode resonator. It has the same fundamental frequency as the driving source, but the amplitudes of peaks are randomly distributed.

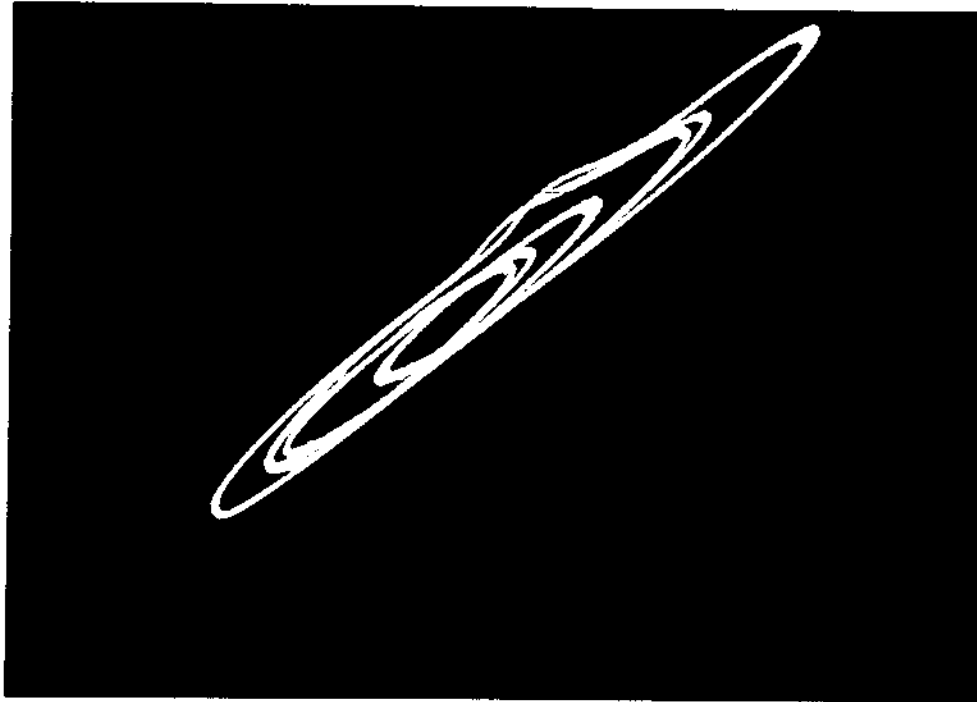


Figure 3.7 Picture taken from oscilloscope showing the phase portrait of the period-8 oscillation in the single diode resonator. There are 8 winding curves in the upper right region, although those curves tend to overlap with each other.

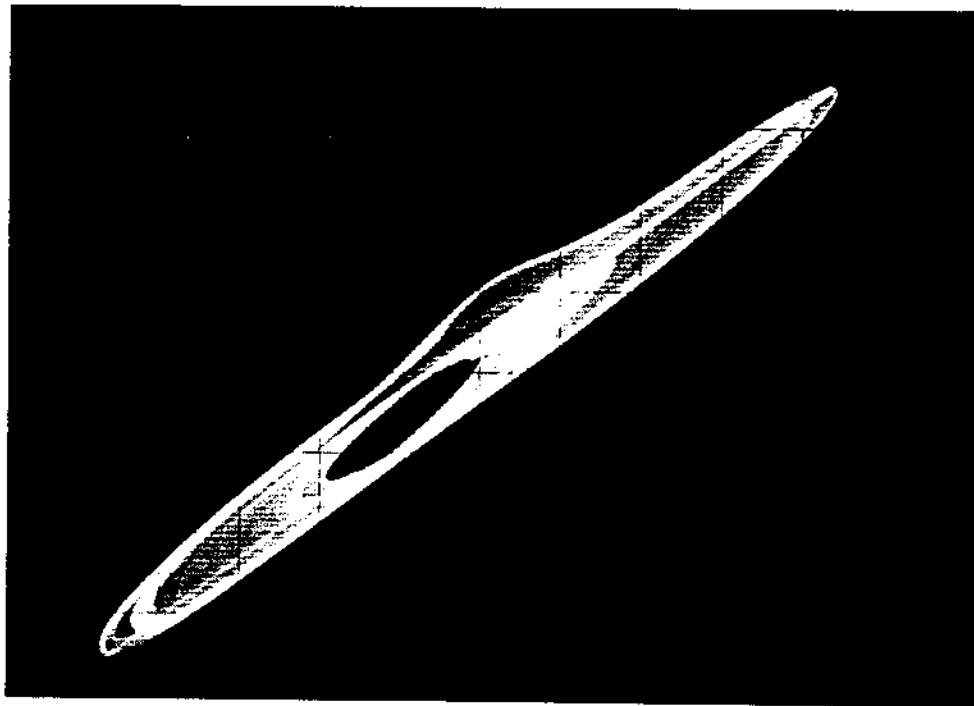


Figure 3.8 Picture taken from oscilloscope showing the phase portrait of the chaotic motion in the single diode resonator. It expanded in one diagonal direction and contracted in another.

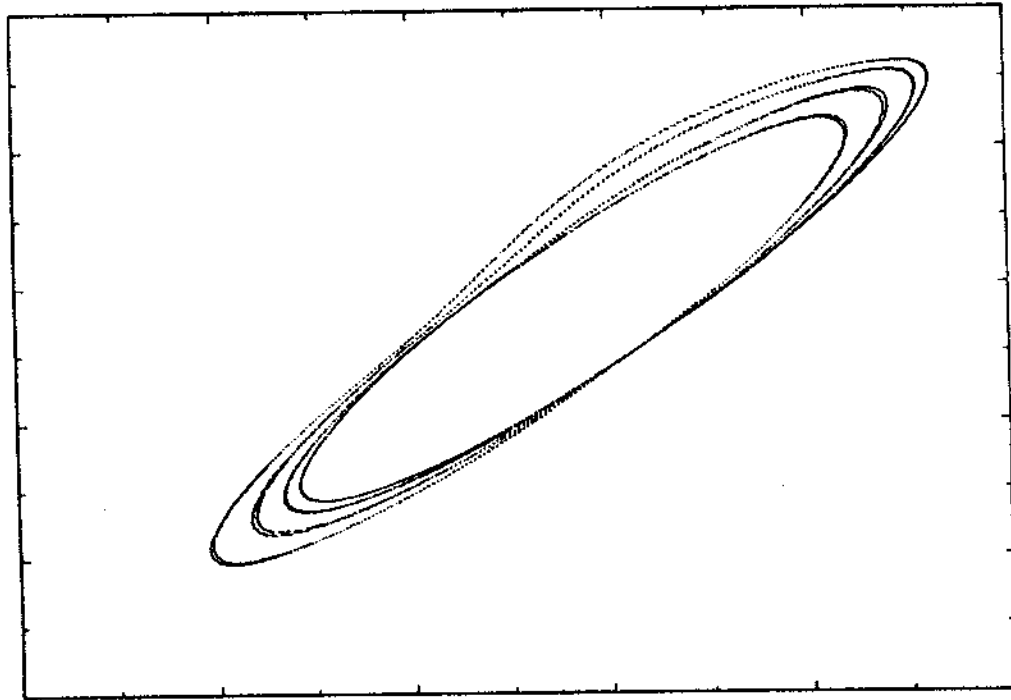


Figure 3.9 Phase plot of period-8 oscillation from simulated Eqs. 3.21-3.23 for single diode resonator. Compare this plot with Fig. 3.7.

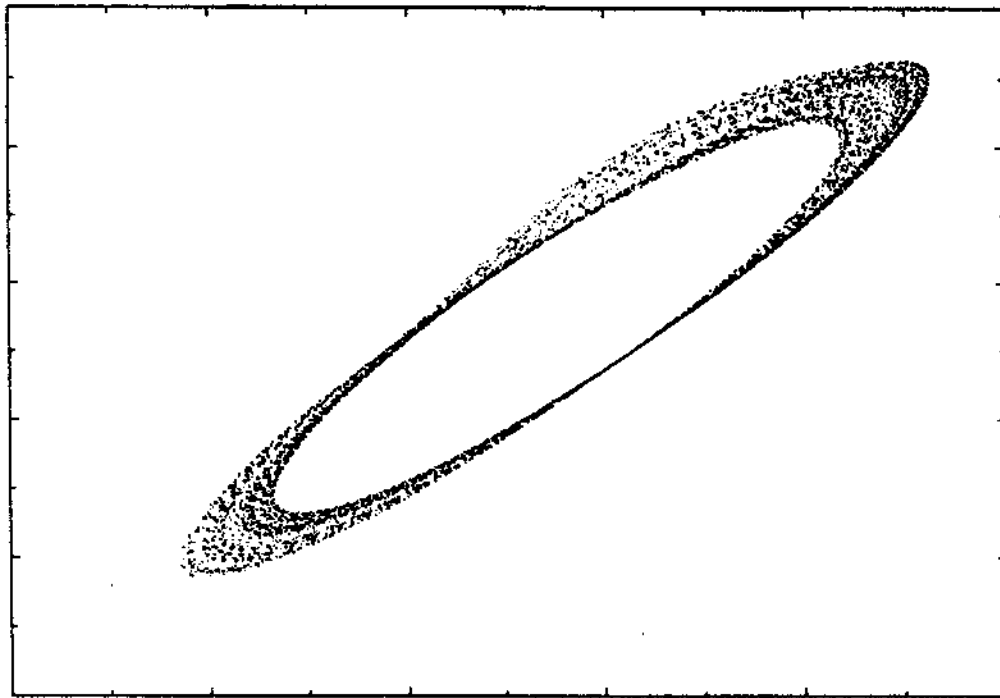


Figure 3.10 Phase plot of a chaos from simulated Eqs. 3.21-3.23 for single diode resonator. Compare this plot with Fig. 3.8.

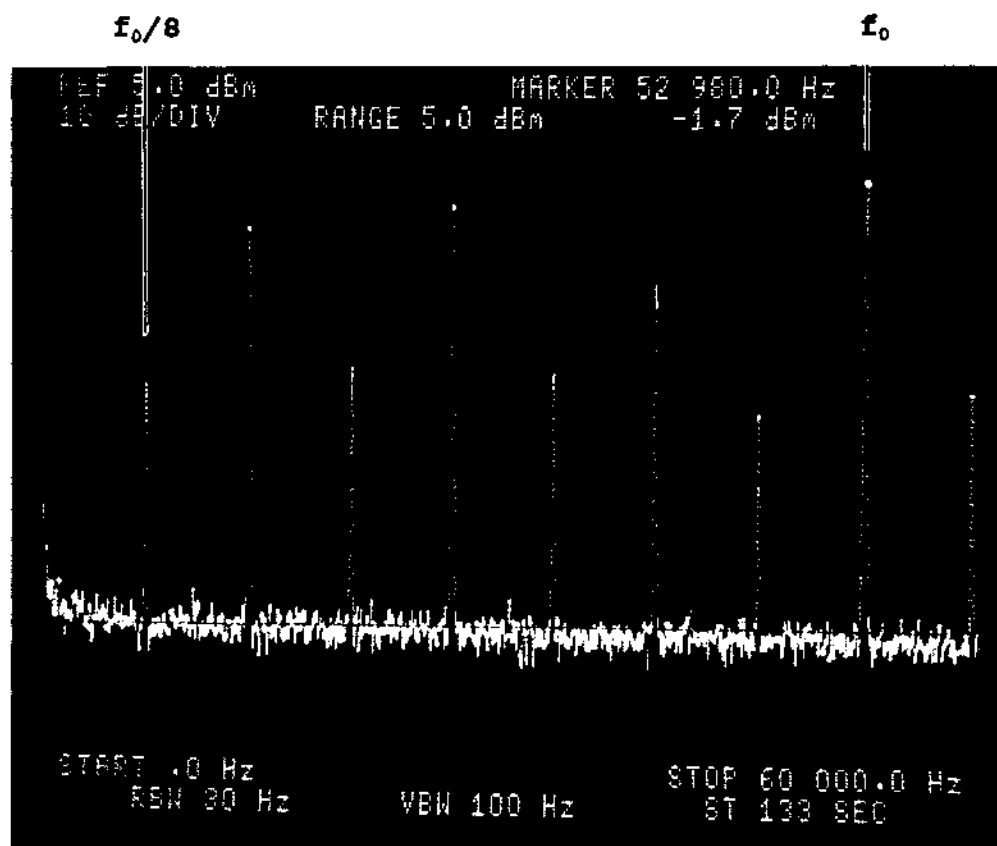


Figure 3.11 Power spectrum corresponding periods 8 of Fig. 3.7 and Fig. 3.9 for the single diode resonator system. The second peak from the right is the fundamental frequency.

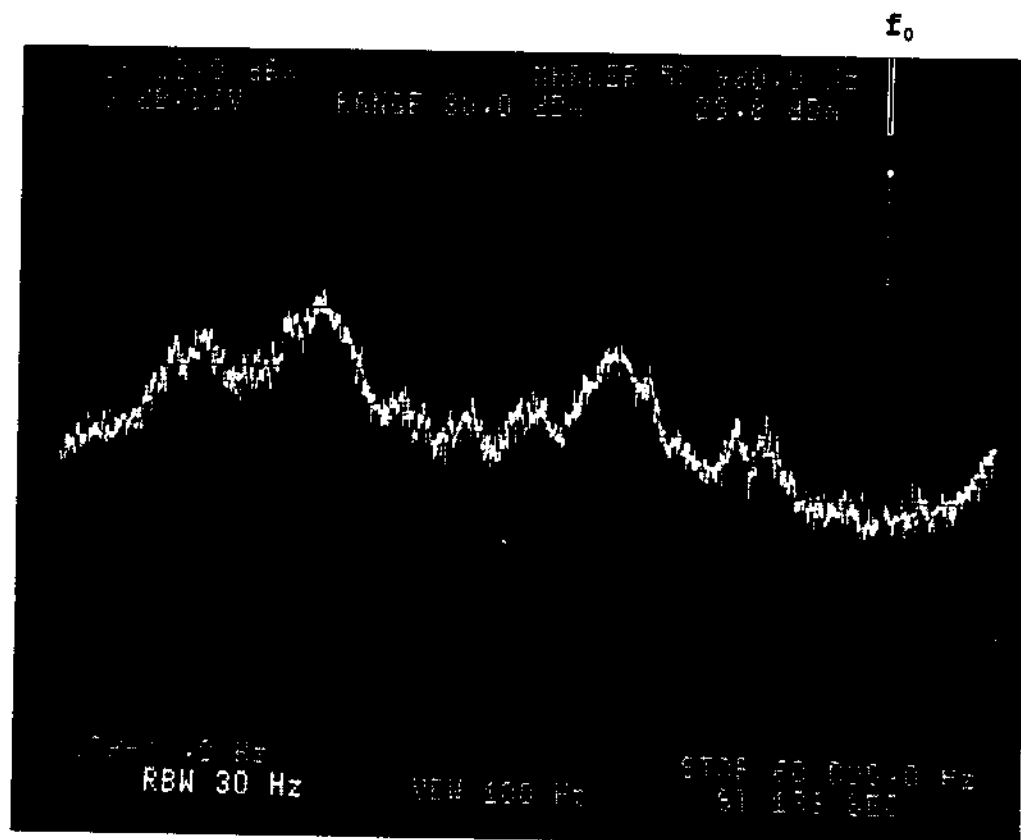


Figure 3.12 Power spectrum corresponding chaos of Fig. 3.8 and Fig. 3.10 for the single diode resonator system. Broad band spectrum indicated that the system is truly in chaotic.

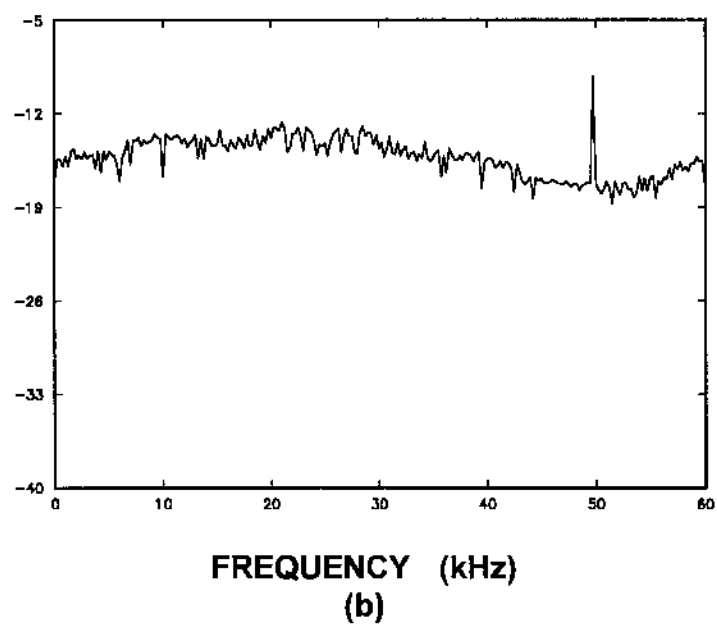
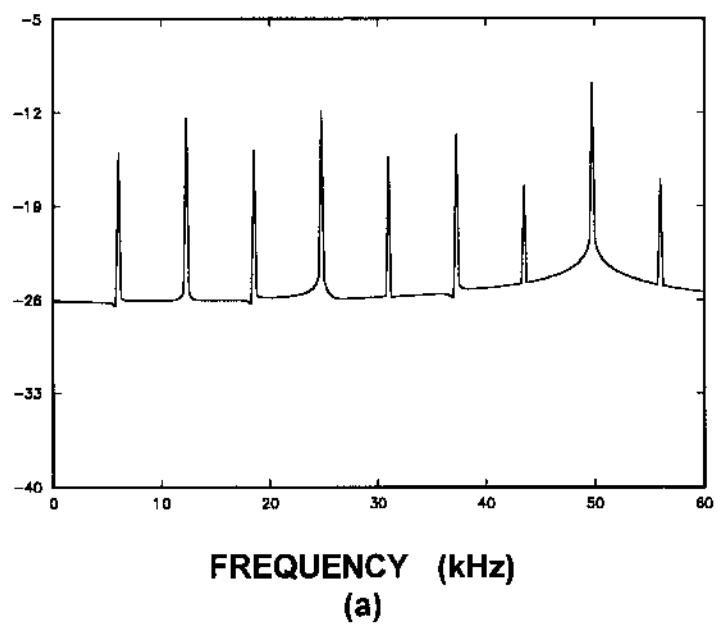


Figure 3.13 Power spectra for (a) period-8 oscillations and (b) chaotic oscillations obtained from simulated systems.

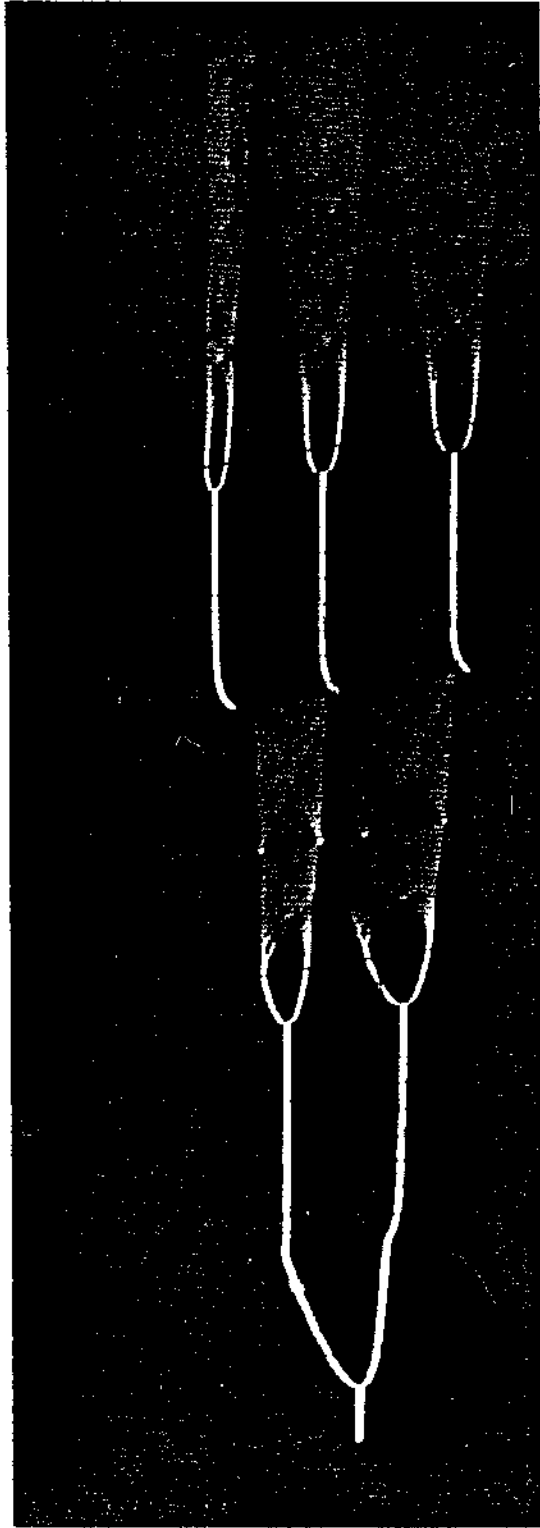


Figure 3.14 Bifurcation diagram obtained from experiment for a single diode resonator system.

Figure 3.15 Bifurcation diagram obtained from simulated Eqs. 3.21-3.23 of a single diode resonator system. Compare this plot with Fig. 3.14 of experimental result. This plot contains 500,000 data points.

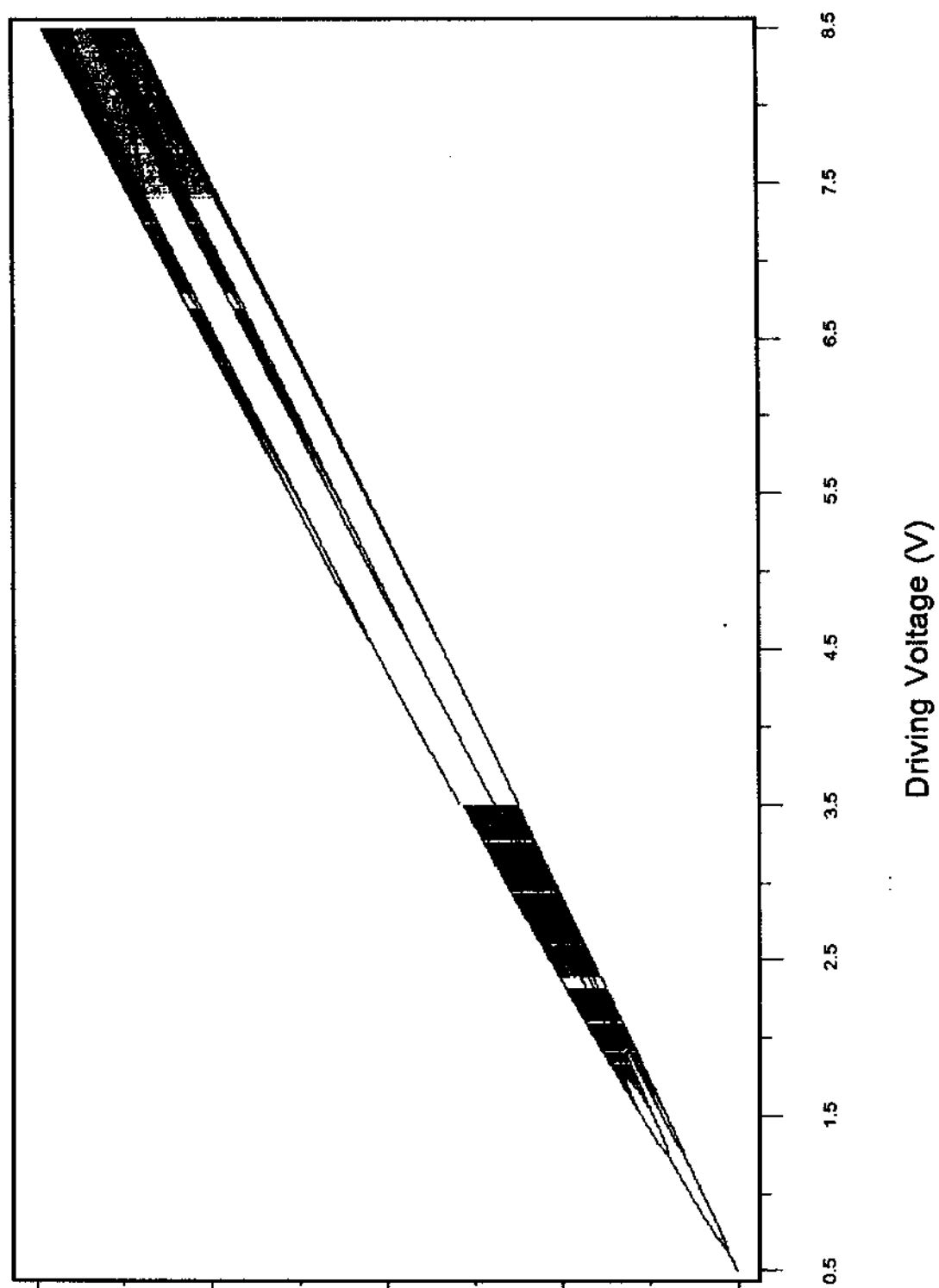


Figure 3.16 Enlarged bifurcation diagram showing the first portion of the Fig. 3.15. It has period doublings, period 5, period 7, *etc.*

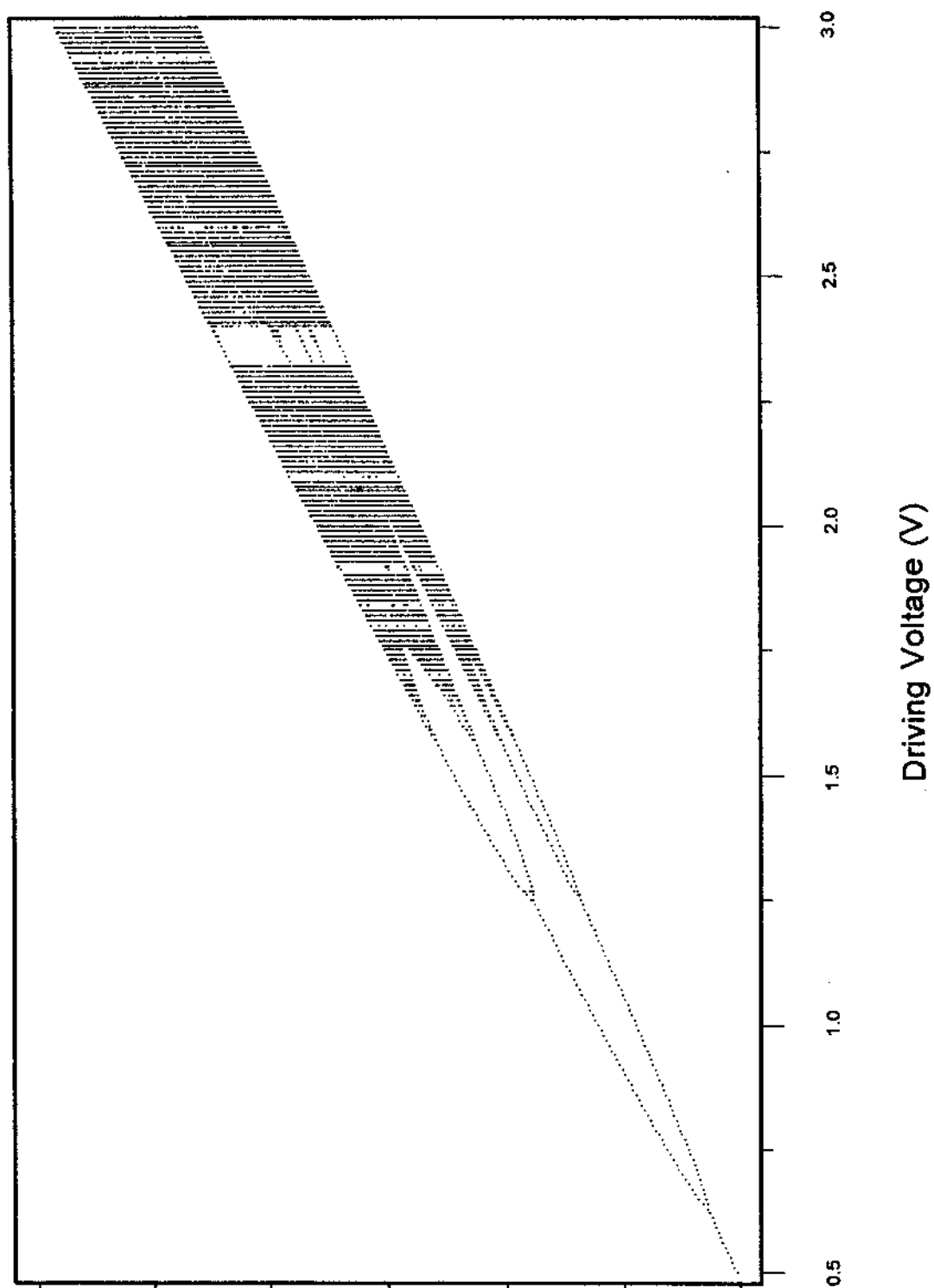
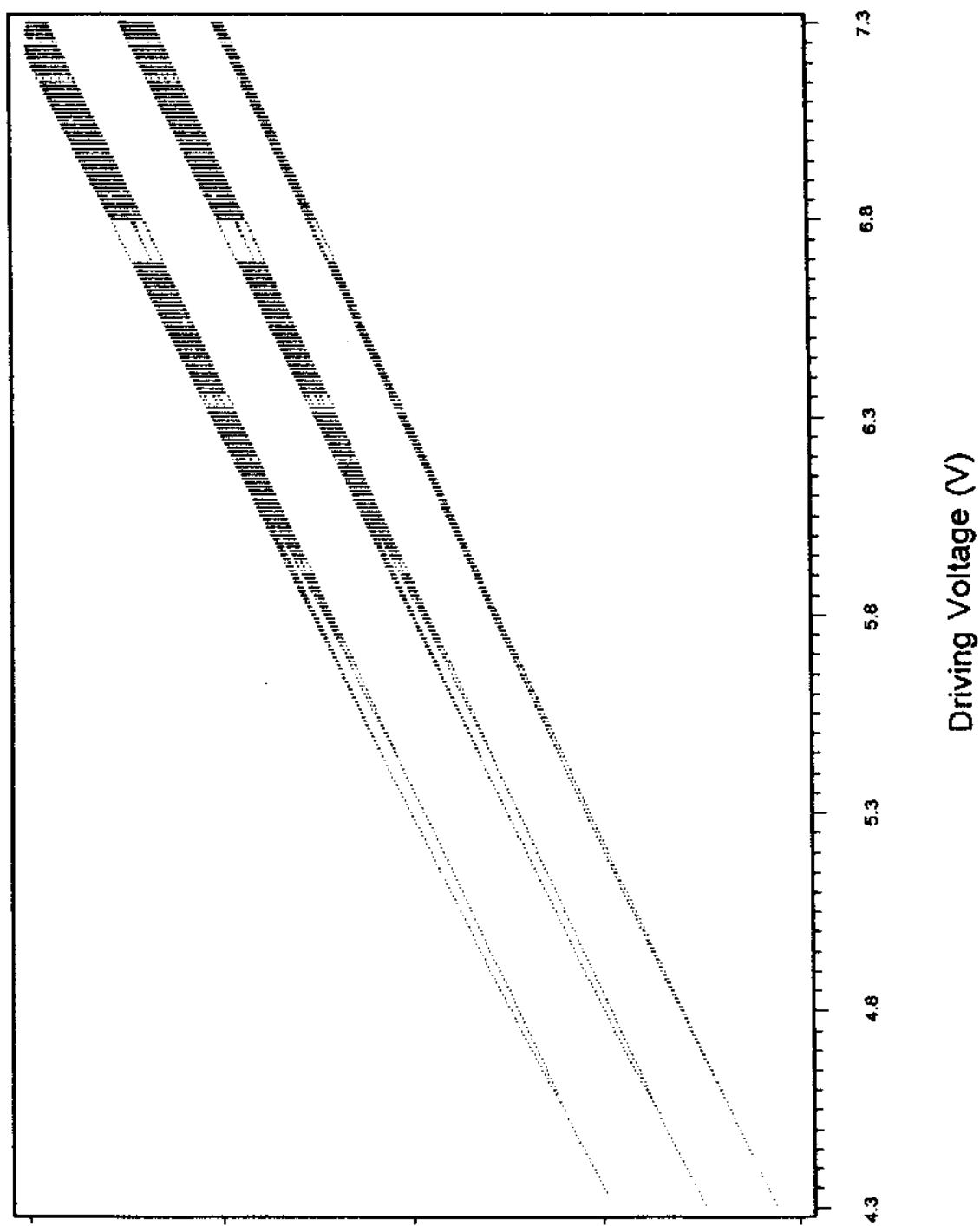


Figure 3.17 Enlarged bifurcation diagram showing the second portion of the Fig. 3.15.



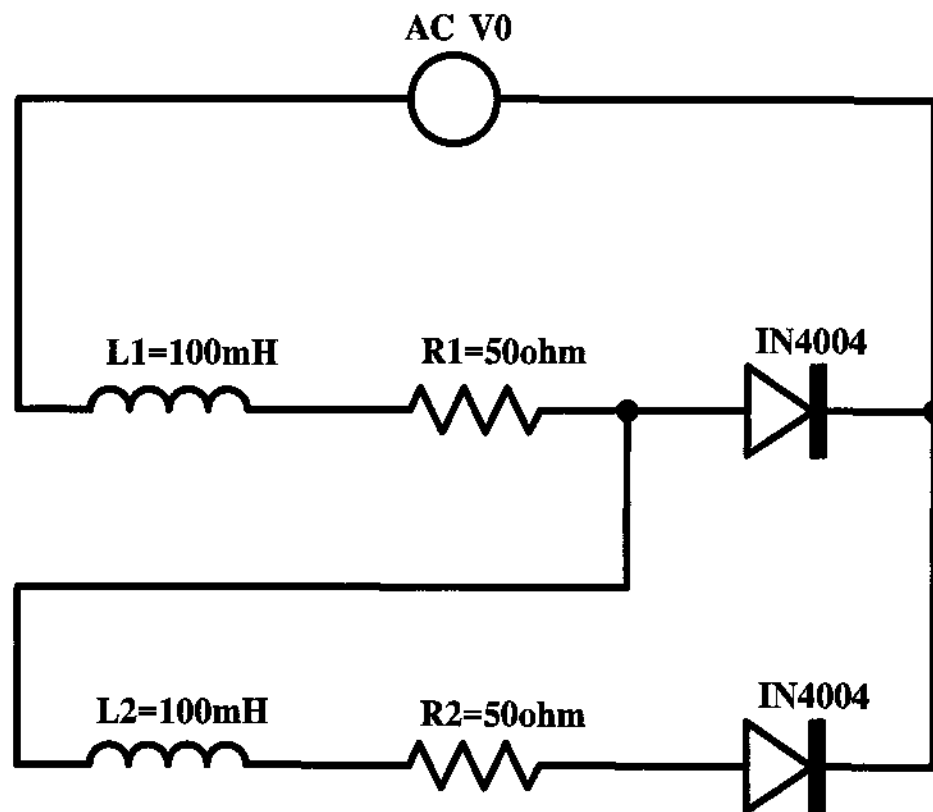
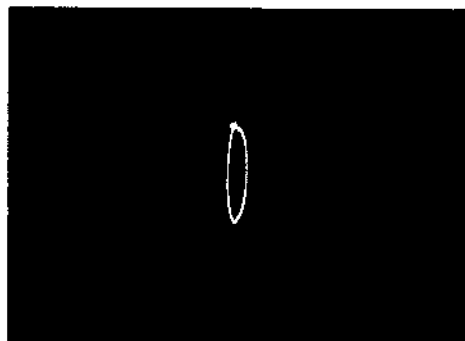
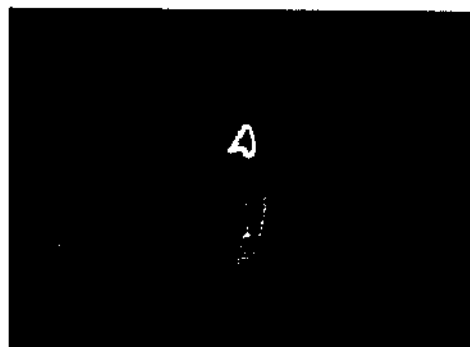


Figure 3.18 Circuit of a line-coupled diode resonator system.

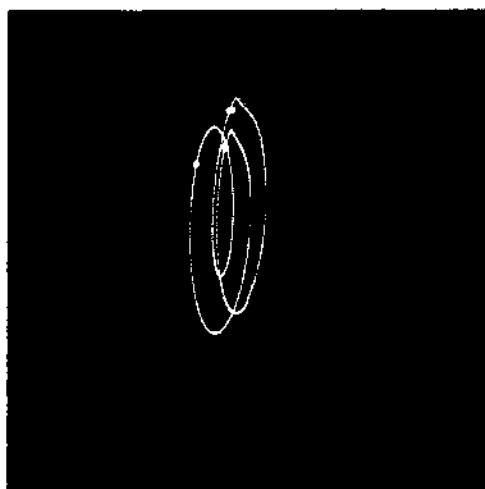


(a)

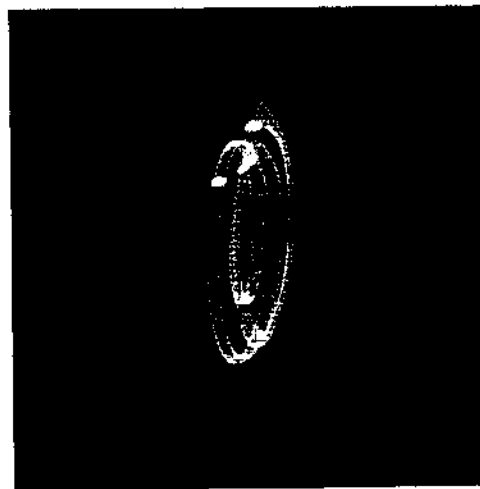


(b)

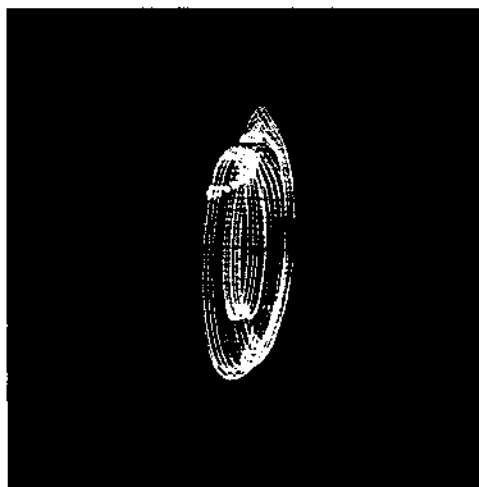
Figure 3.19 Phase plots for (a) period-1 with driving amplitude $V_0 \leq 6.07V$ and (b) two frequency quasiperiodic oscillations with driving amplitude in the range: $6.07V \leq V_0 \leq 9.87V$.



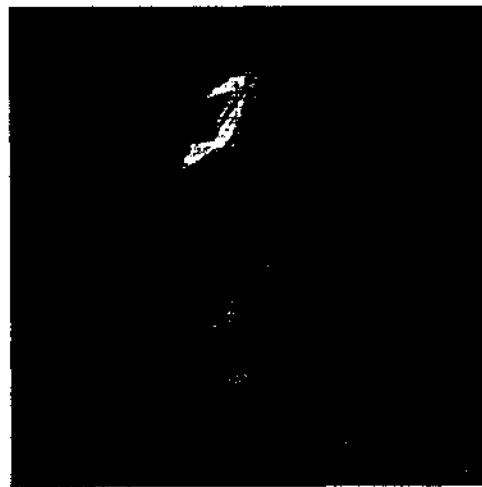
(a)



(b)



(c)



(d)

Figure 3.20 Sequence of phase plot for the driving amplitude $V_0 \geq 10.05V$ i.e., after the first transition to chaos. (a) Period three state. (b) Quasiperiodic state. (c) Frequency locked state. (d) Second chaotic state.

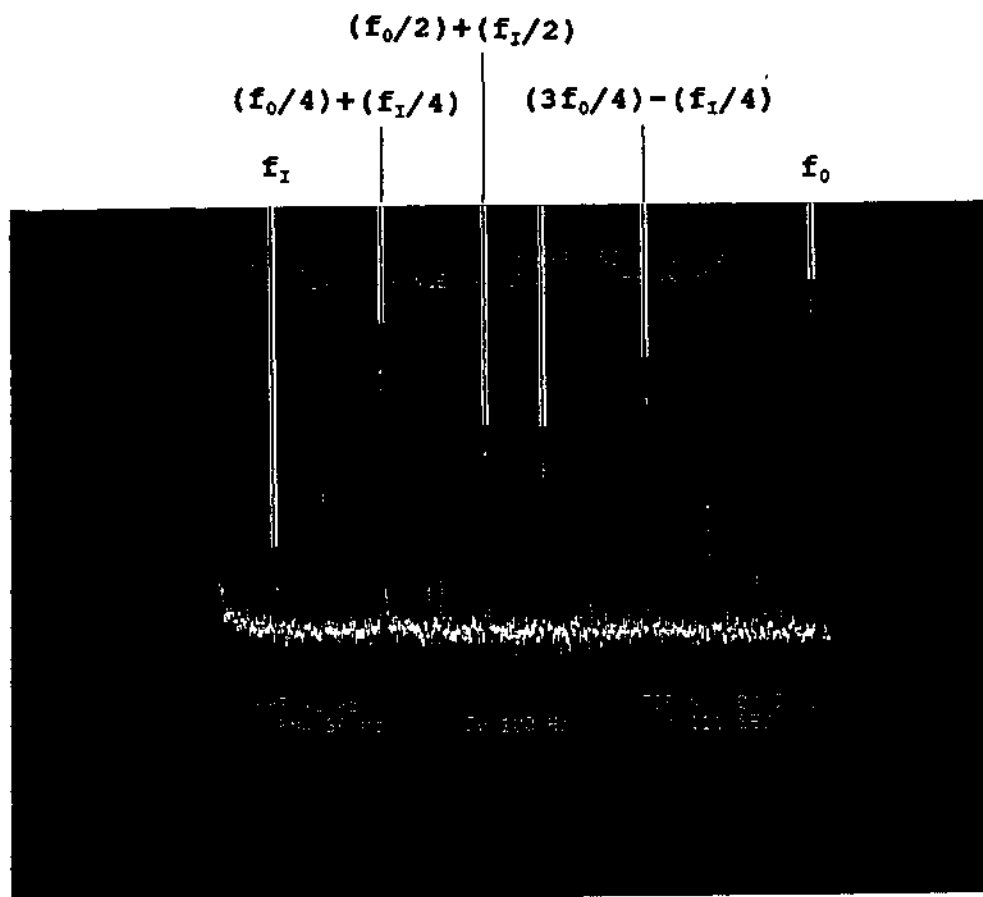


Figure 3.21 Power spectrum of the quasiperiodic state shown in Fig. 3.20(b). Here the two basic frequencies are $f_0 \approx 50.22\text{KHz}$ and $f_I \approx 4.43\text{KHz}$.

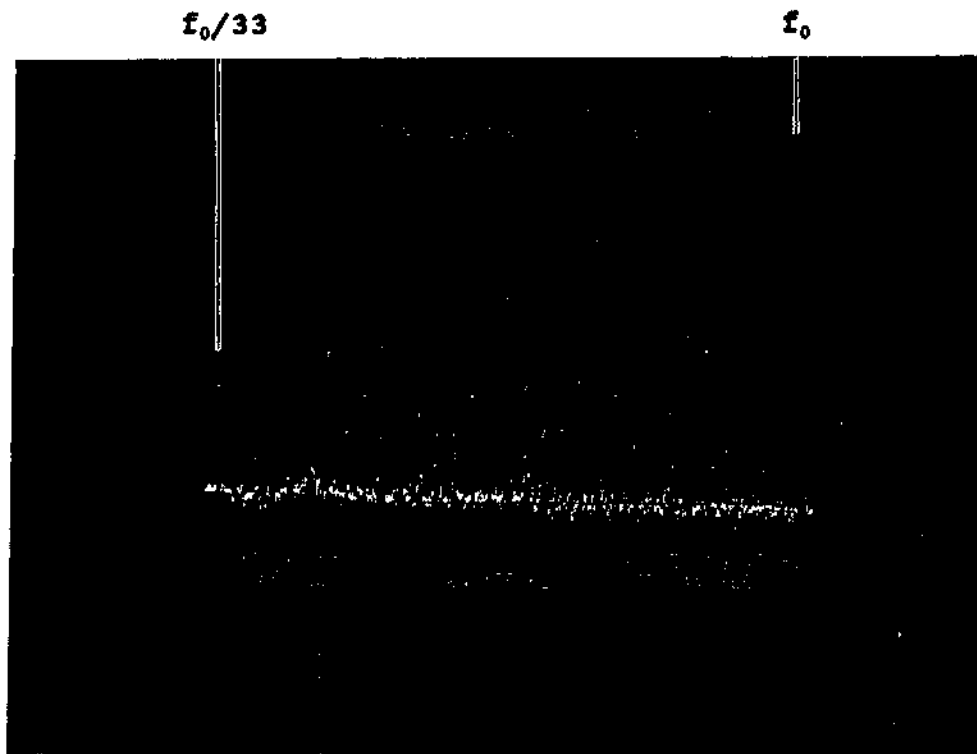


Figure 3.22 The power spectrum of frequency locked state corresponding to the phase plot shown in Fig. 3.20(c). The locking ration is 33/3.

Figure 3.24 Bifurcation diagram obtained from Eqs. 3.24-3.28 of the simulated line-coupled diode resonator system. The driving amplitude ranges from 2.0V to 3.0V. This plot contains 300,000 data points.

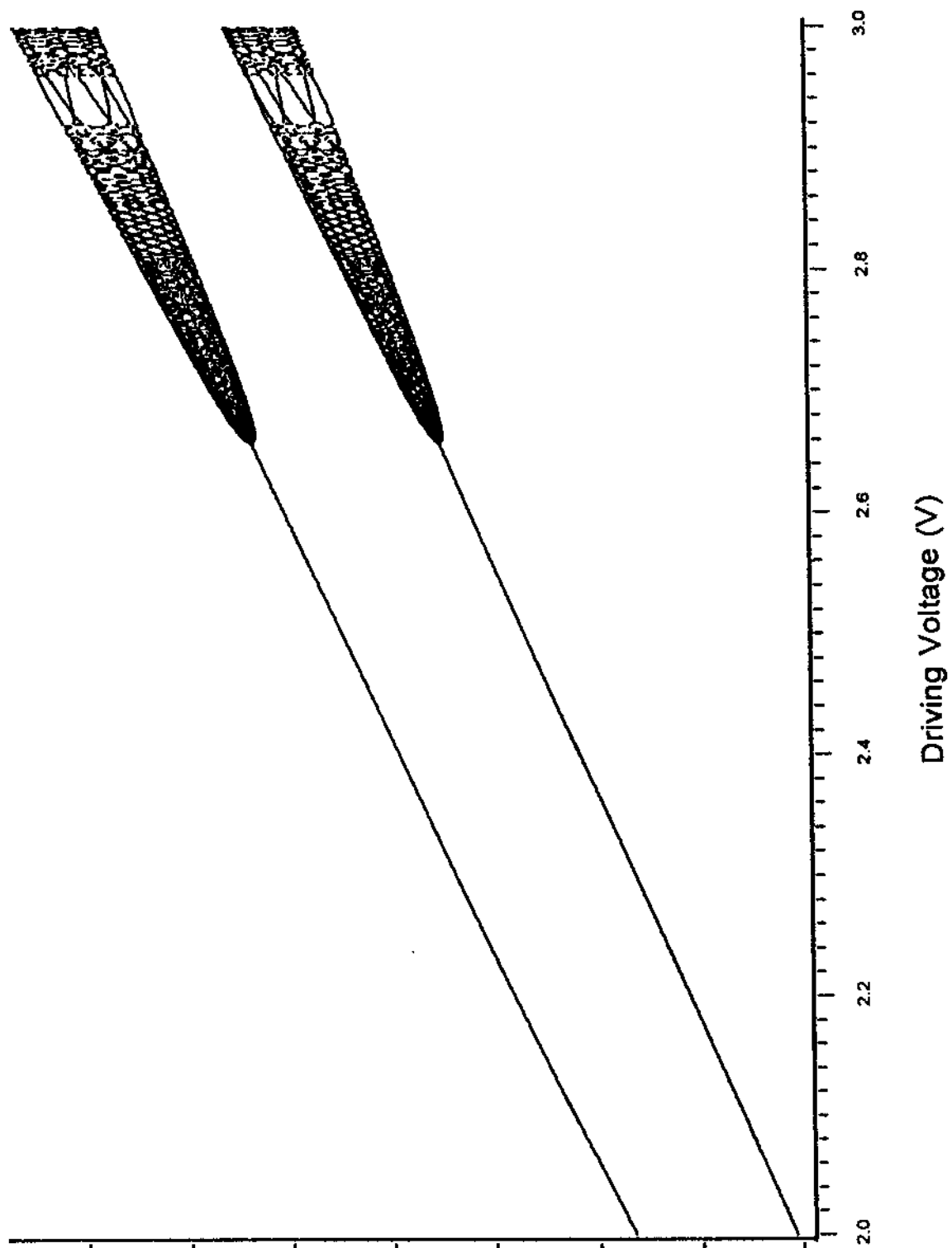
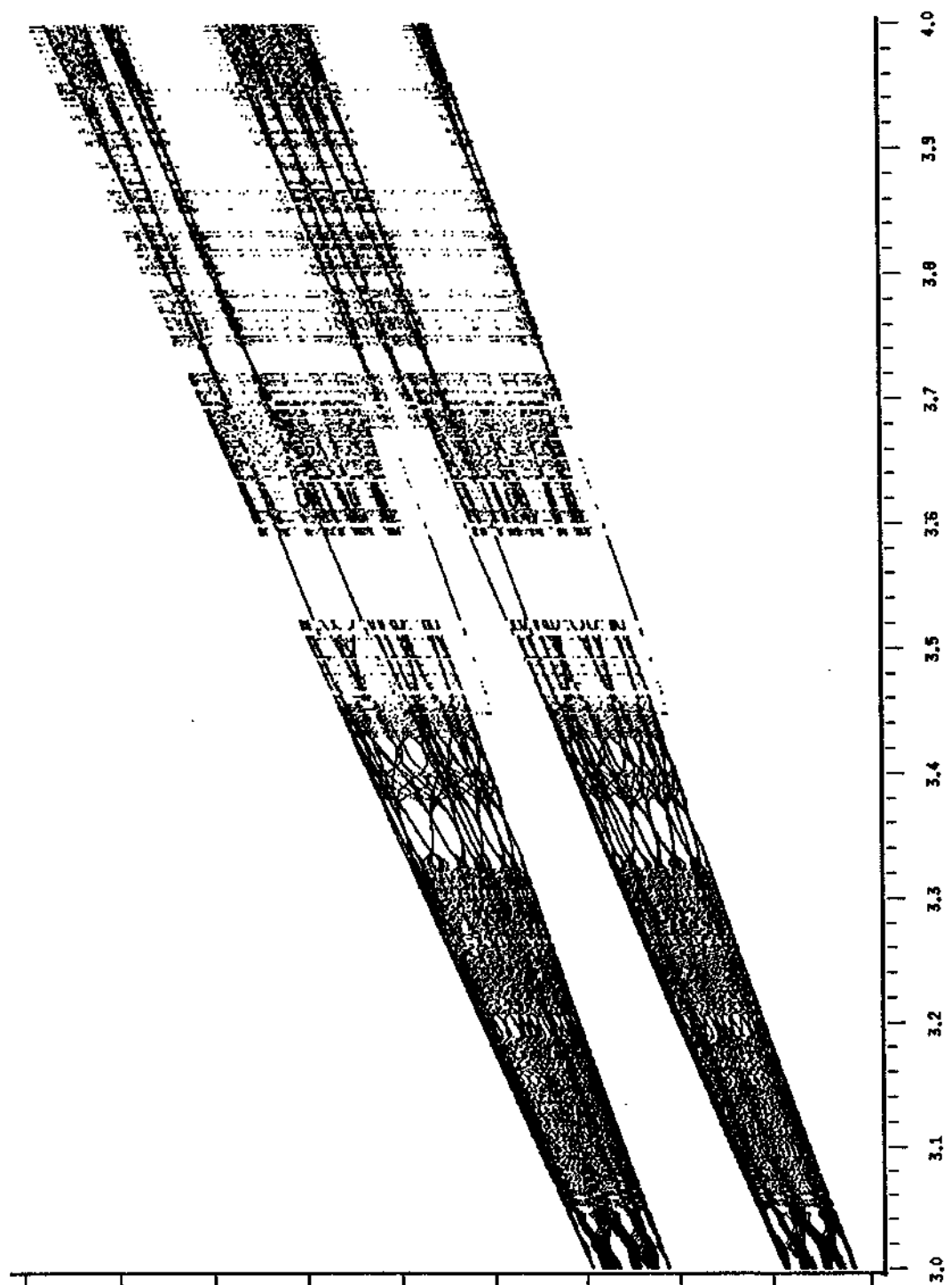


Figure 3.25 Another bifurcation diagram obtained from Eqs. 3.24-3.28 of simulated line-coupled diode resonator system. The driving amplitude is ranging from 3.0V to 4.0V. This plot contains 300,000 data points.



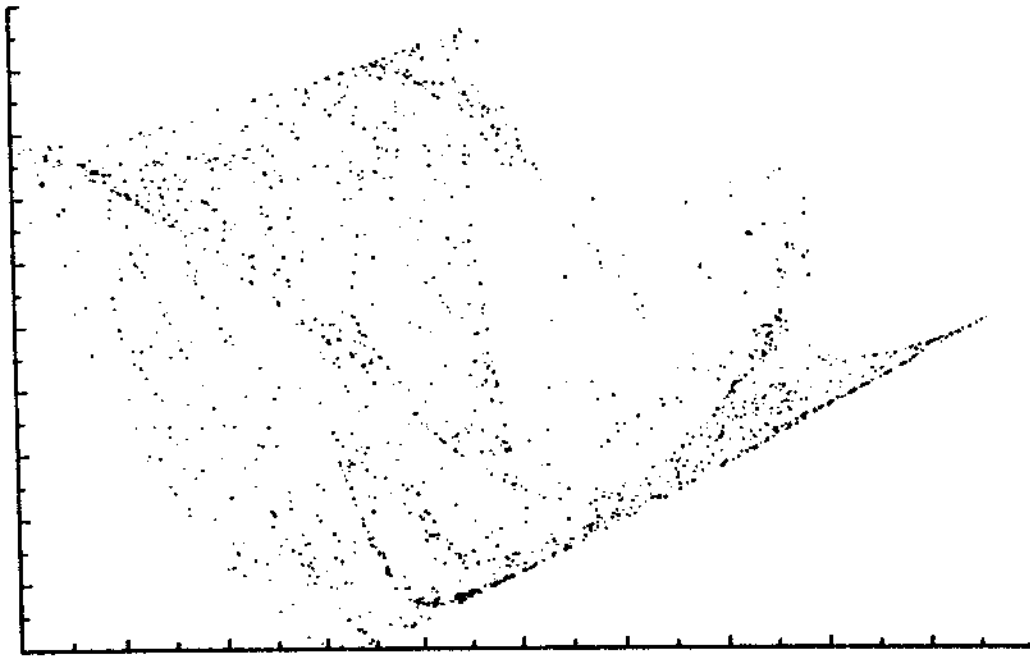
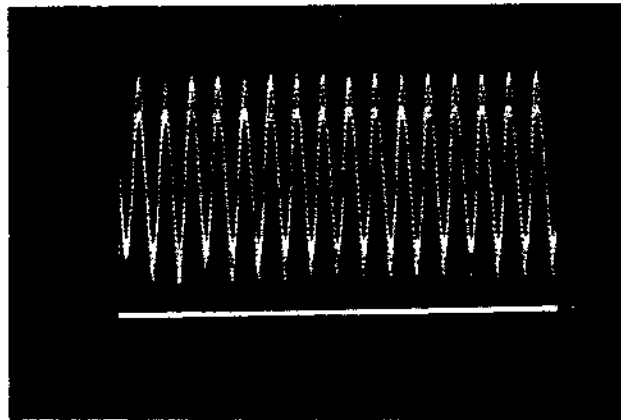
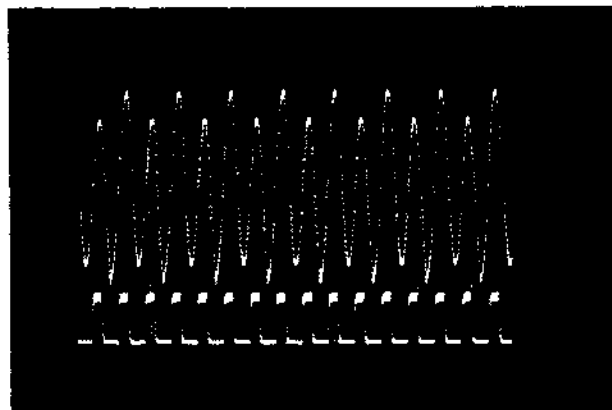


Figure 3.26 The Poincaré section of a chaotic attractor for a simulated four-line-coupled diode resonator system. Compare this plot with Fig. 3.32(a) of the experimental result.

(a)



(b)



(c)

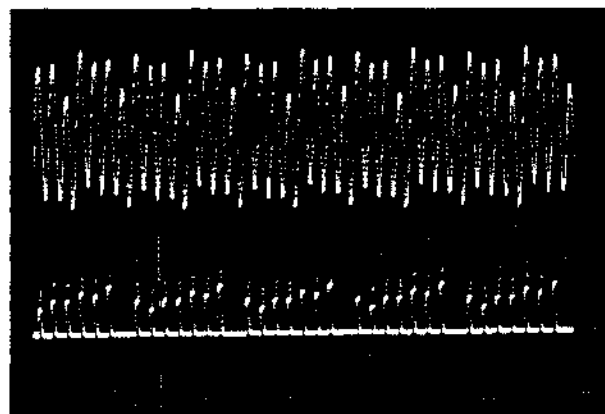
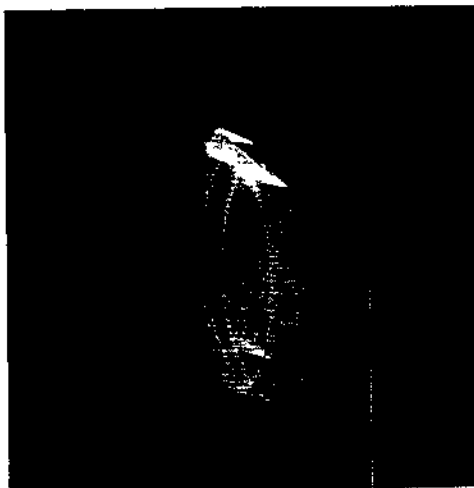
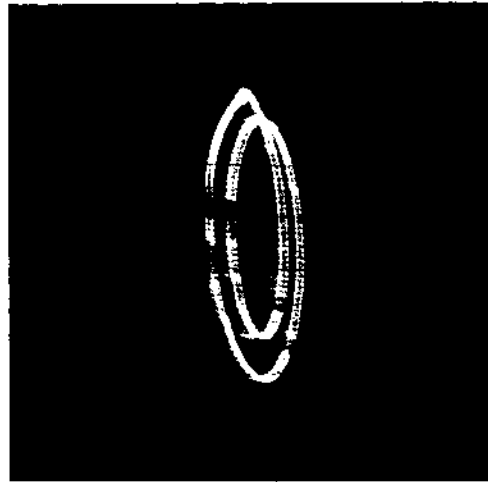


Figure 3.27 System signals (top) and control signals (bottom) for (a) chaotic attractor with control off, (b) stabilized period-2 and (c) stabilized period-8.



(a)



(b)



(c)

Figure 3.28 Phase plot for (a) chaotic attractor before the control (b) stabilized quasiperiodic oscillation and (c) stabilized periodic locked state.

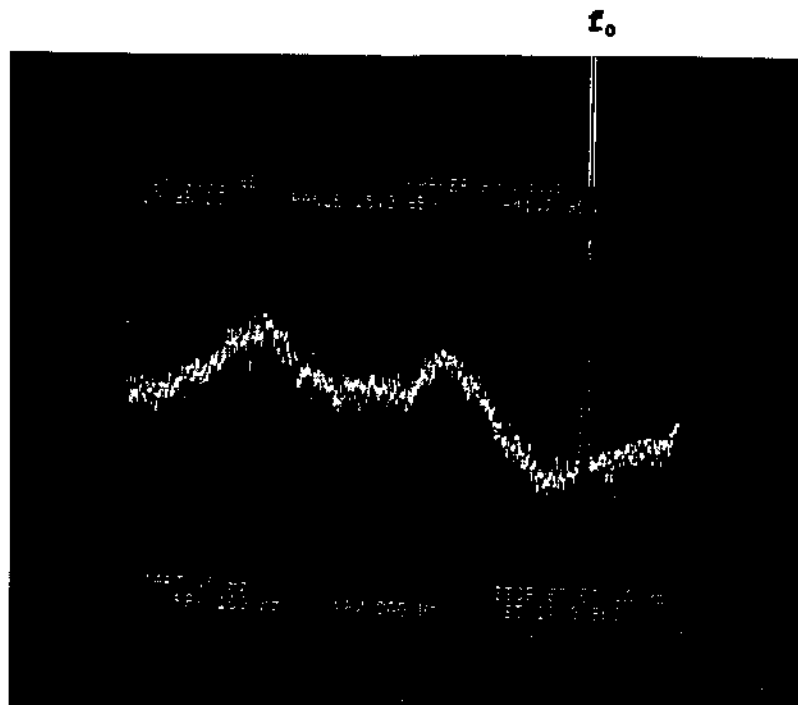


Figure 3.29 Power spectrum for the chaotic attractor before the stabilization; the corresponding phase plot is shown in Fig. 3.28(a).

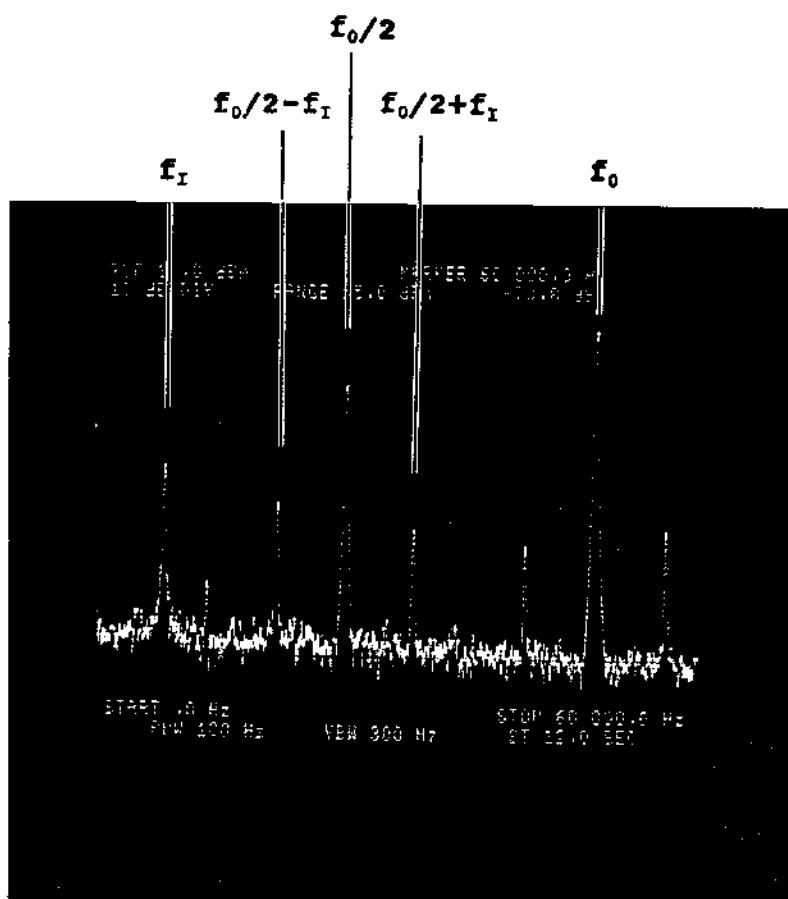
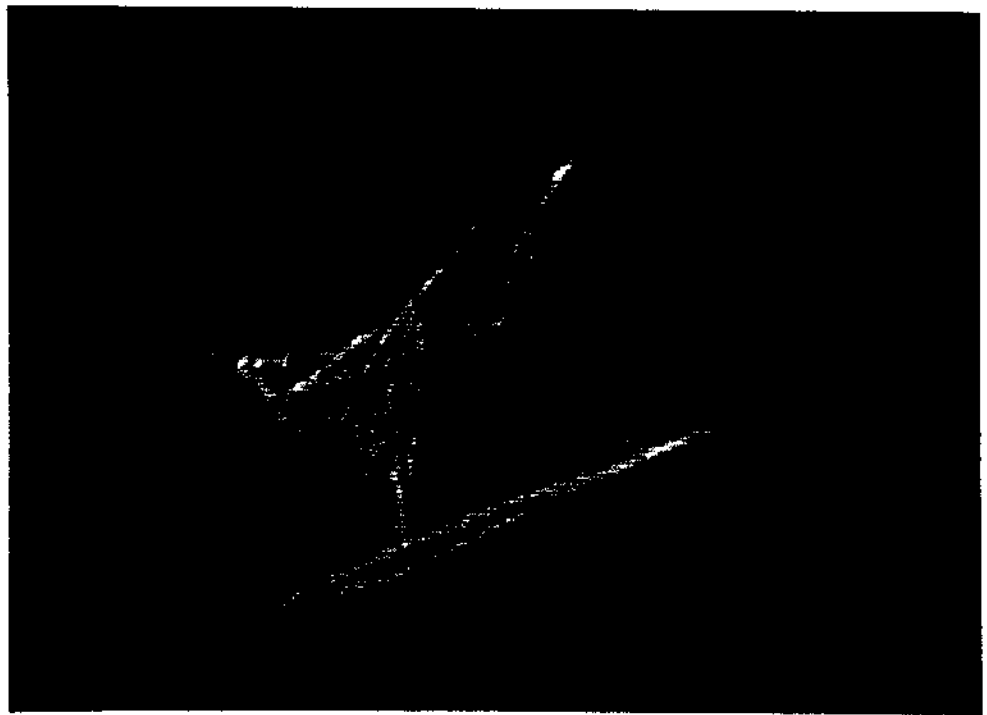


Figure 3.30 Power spectrum for the stabilized quasiperiodic oscillation; the corresponding phase plot is shown in Fig. 3.28(b).

Figure 3.32 Poincare sections of a four-line-coupled diode resonator system for (a) a chaotic attractor before the control on and (b) the two-frequencies quasiperiodic oscillation stabilized from the above chaotic attractor. Their power spectra are shown in Fig. 3.33(a) and (b) respectively.

(a)



(b)

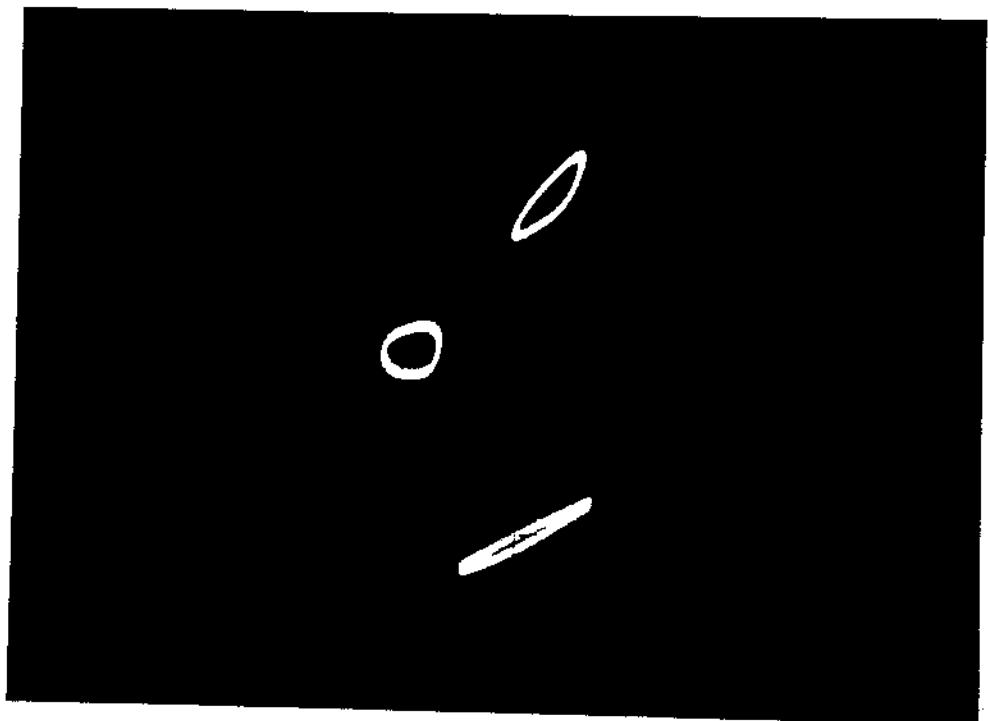
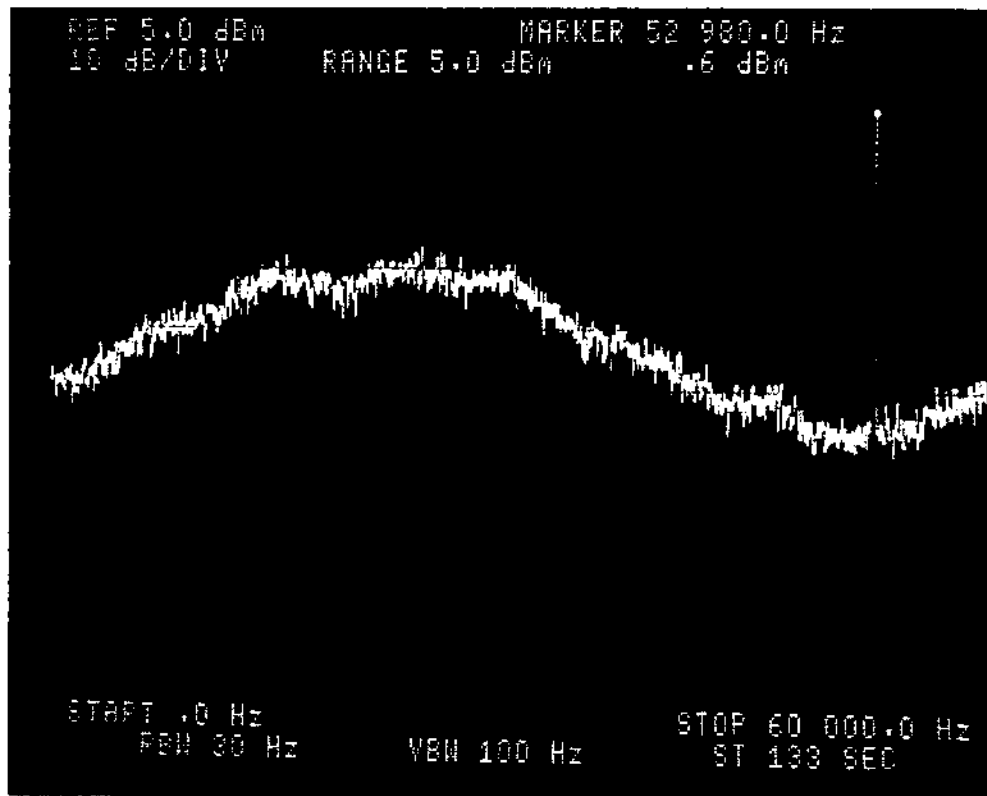
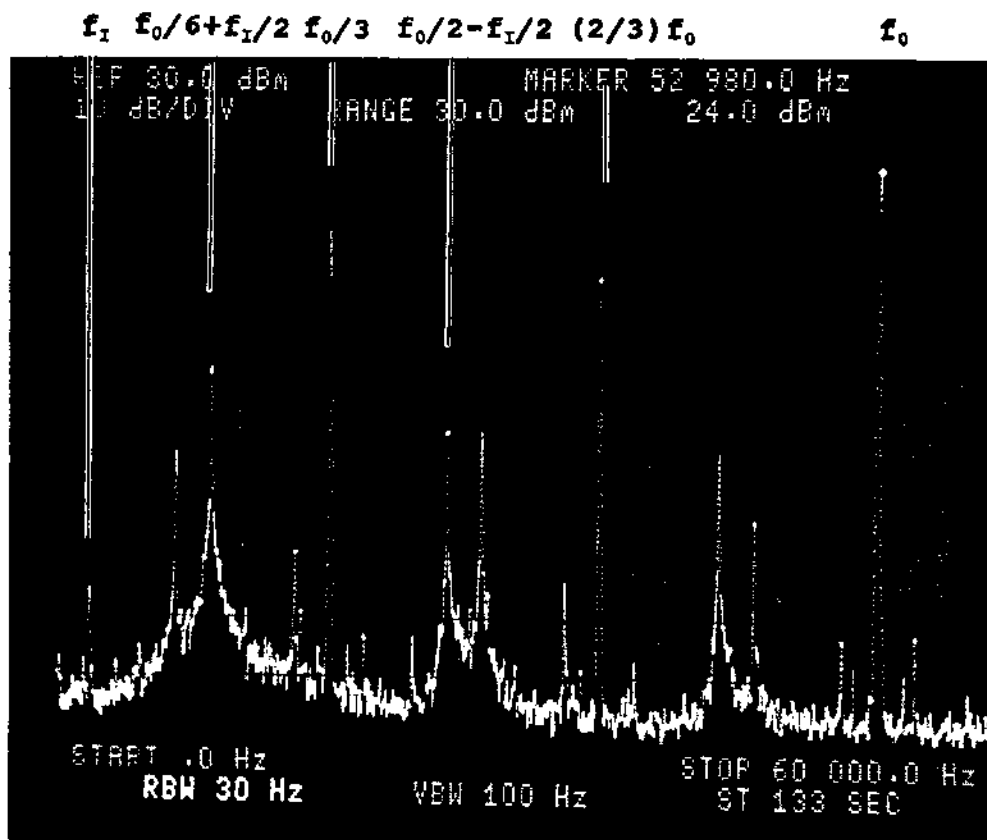


Figure 3.33 Power spectra for the (a) chaotic motion before the stabilization and (b) quasiperiodic oscillation with two incommensurate frequencies as result of the stabilization.

(a)



(b)



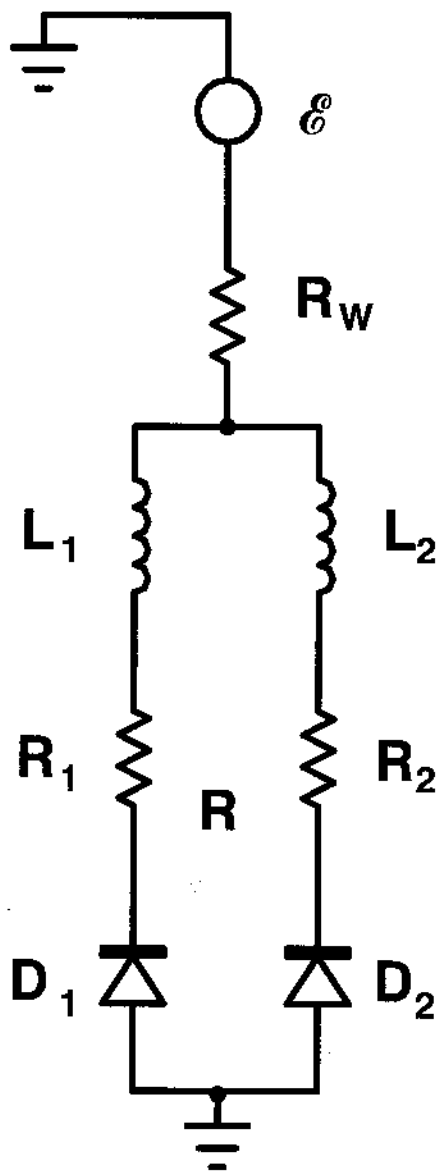


Figure 3.34 A Tunnel diode relaxation oscillator unit. L_1 and L_2 are inductors; R_1 , R_2 and R_w are resistors; D_1 and D_2 are tunnel diodes; \mathcal{E} is the power supply. The effective capacitors (C_1 and C_2) for two tunnel diodes and an extra coupling resistor (R) for another version of oscillator circuit are drawn in dashed lines.

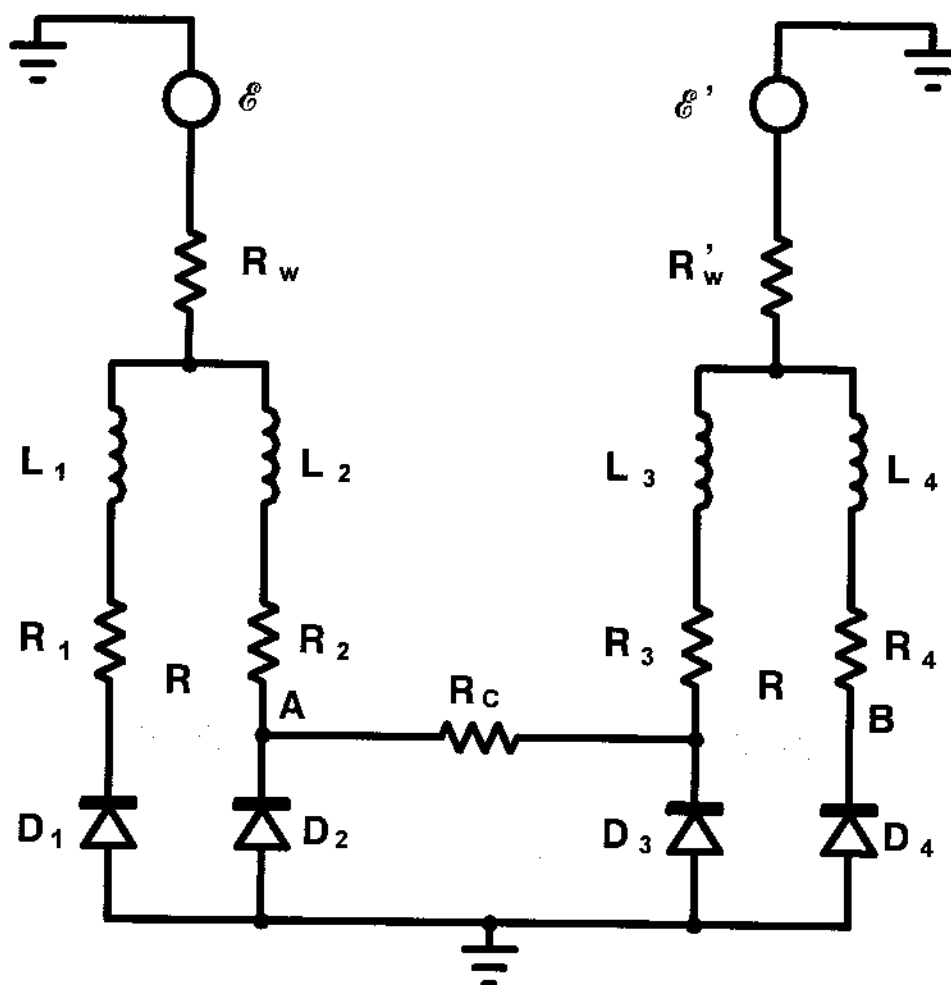
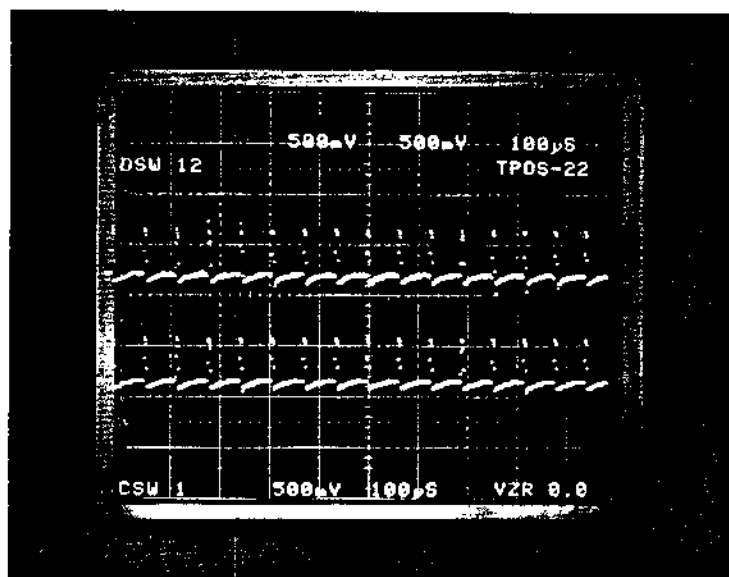


Figure 3.35 Two coupled relaxation oscillators. Voltages are measured at A and B. The values for elements in this circuit are listed in the Table 1.

(a)



(b)

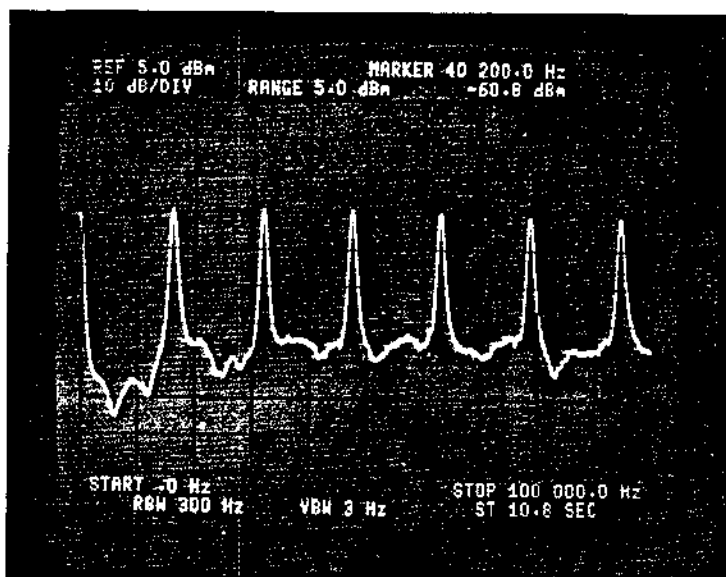
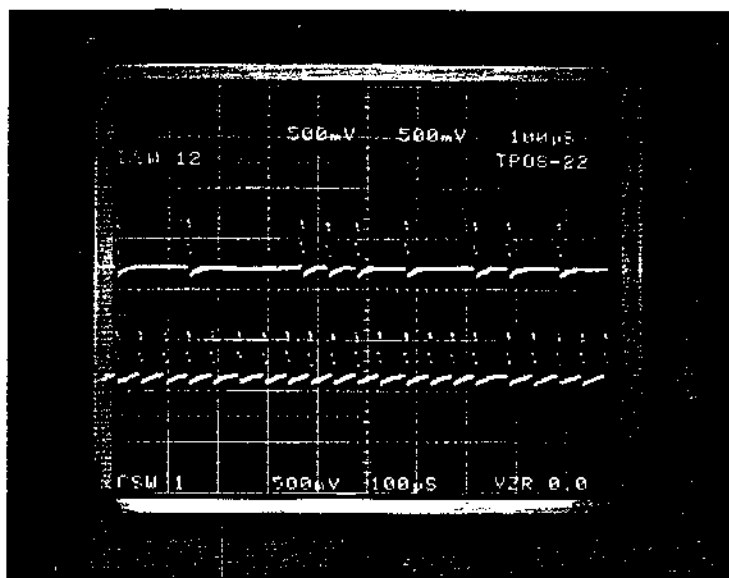


Figure 3.36 (a) Synchronized chaotic voltages. Top trace and bottom traces are measured at A and B respectively. (b) Corresponding power spectra.

(a)



(b)

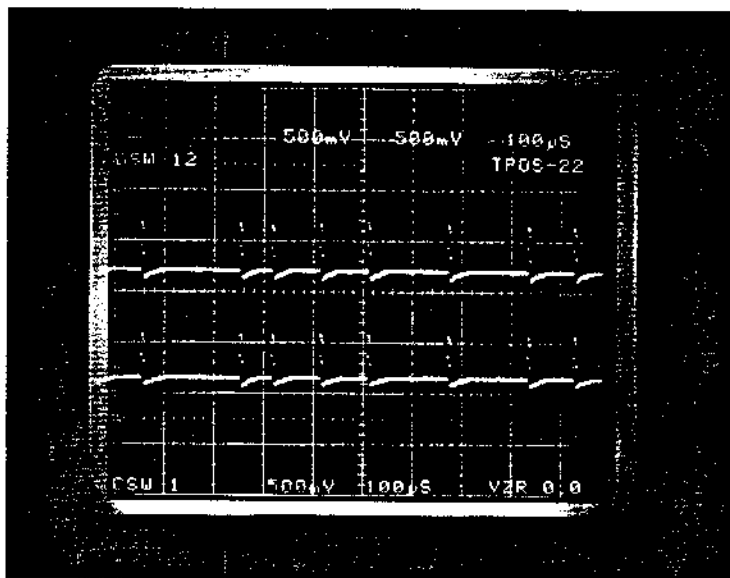


Figure 3.37 (a) Chaotic voltages before coupling (without R_C). (b) Synchronized chaotic voltages with coupling of R_C .

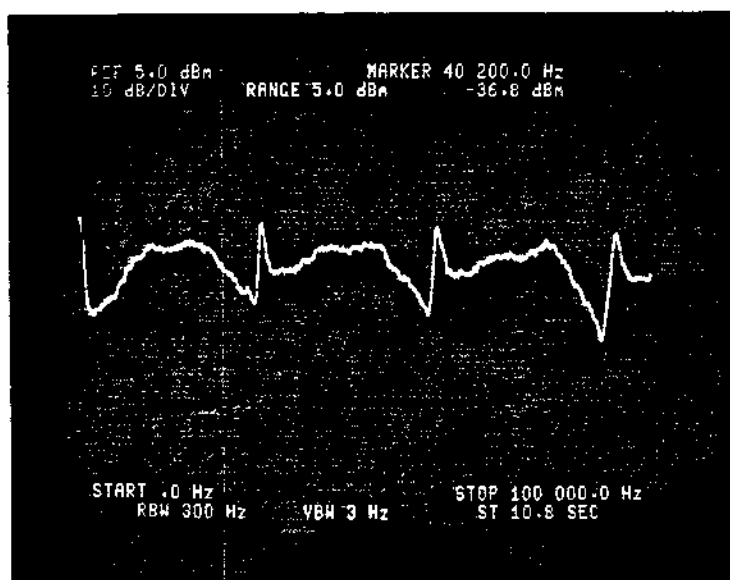
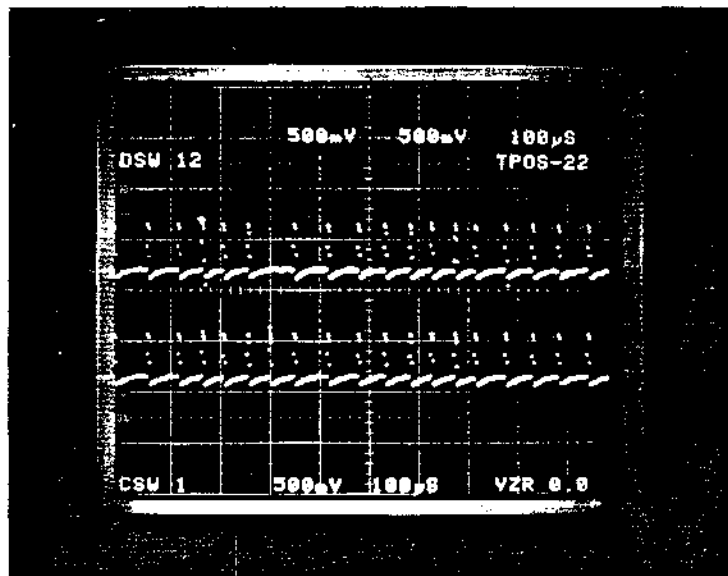


Figure 3.38 Power spectrum for synchronized voltages of Fig. 3.37(b).

(a)



(b)

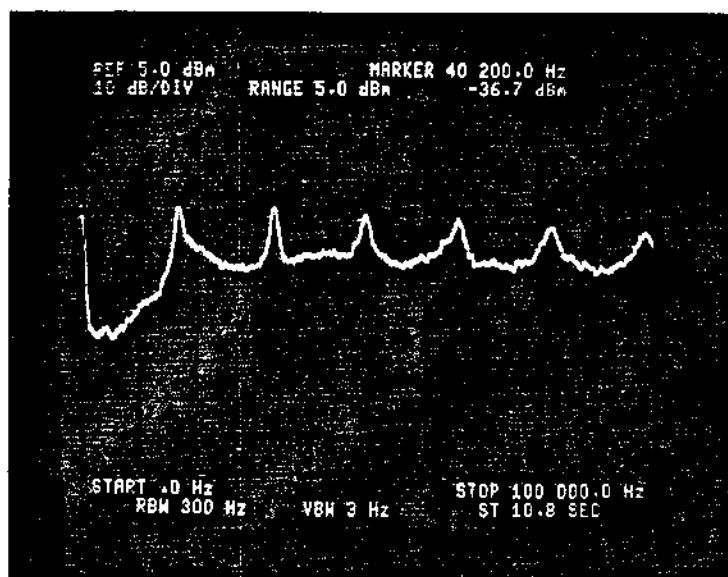
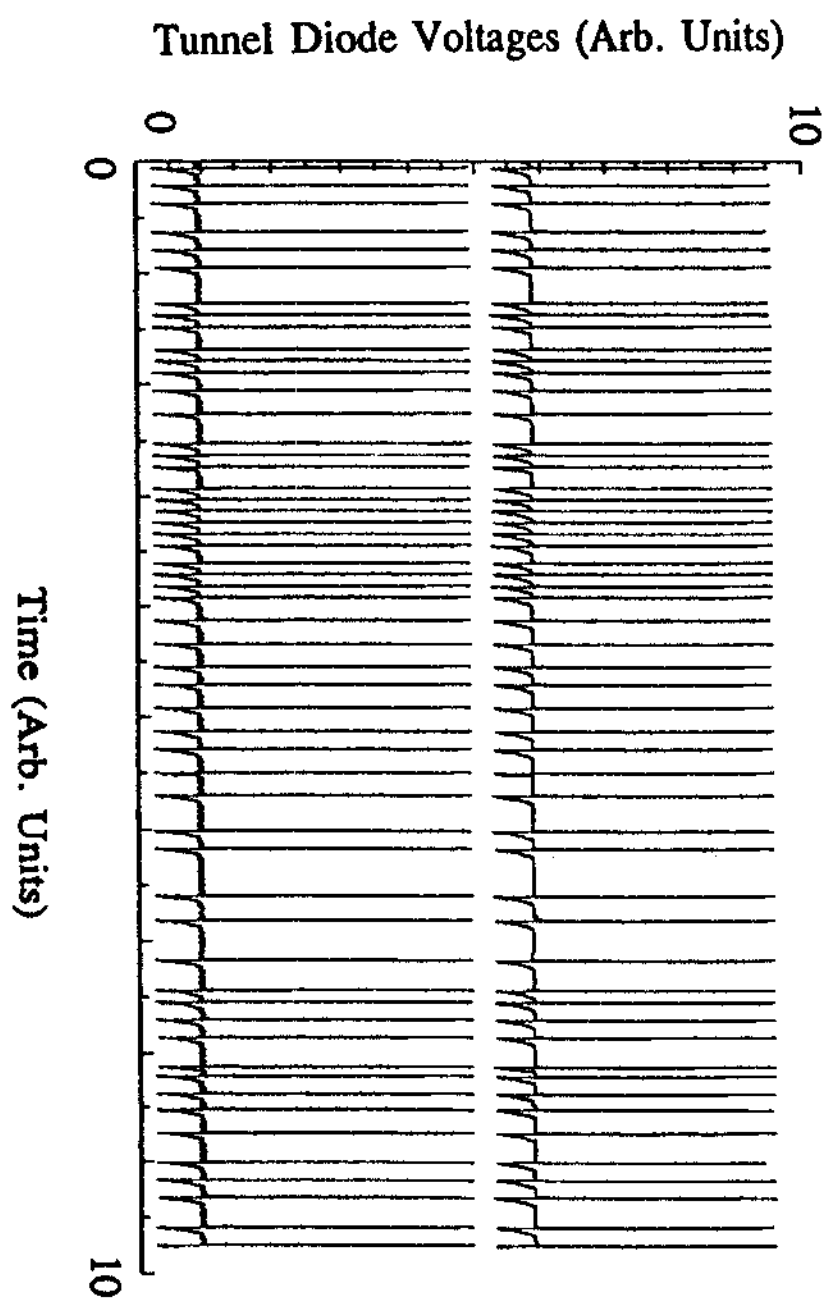
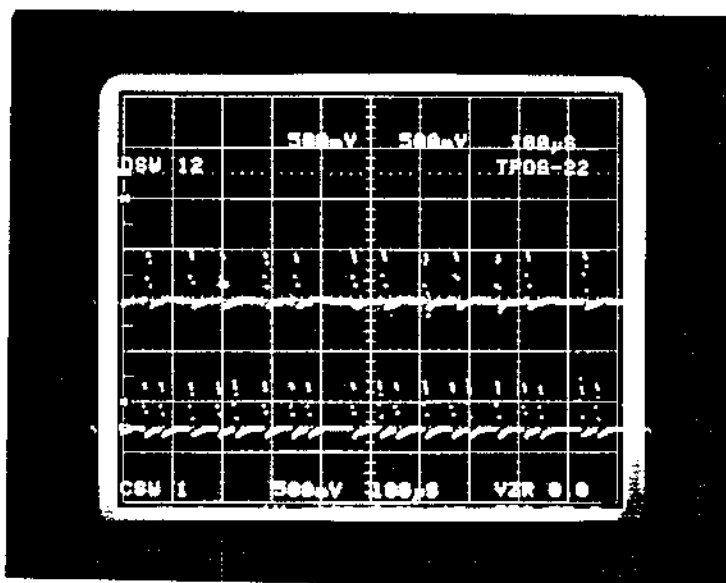


Figure 3.39 (a) Synchronized chaotic voltages. (b) Corresponding power spectrum.

Figure 3.40 Synchronized chaotic voltages for the same experimental conditions as Fig 3.37(b). The data were obtained by digitizing the signals at 8-bit resolution and 5Mhz speed.



(a)



(b)

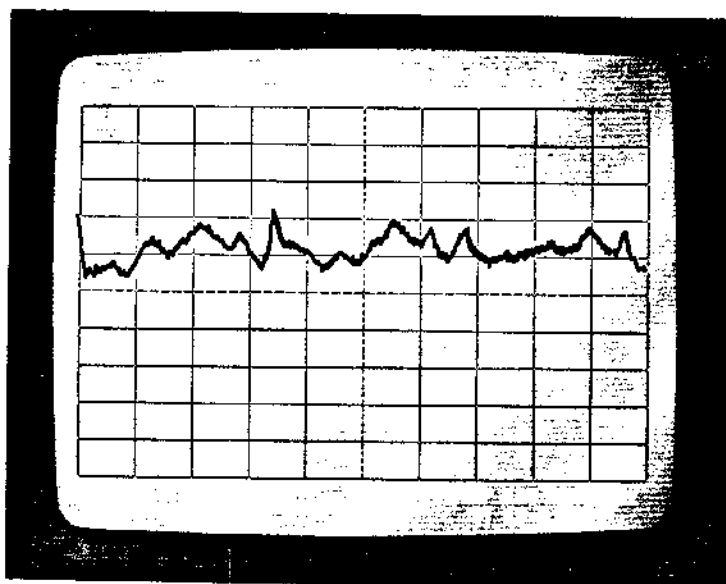
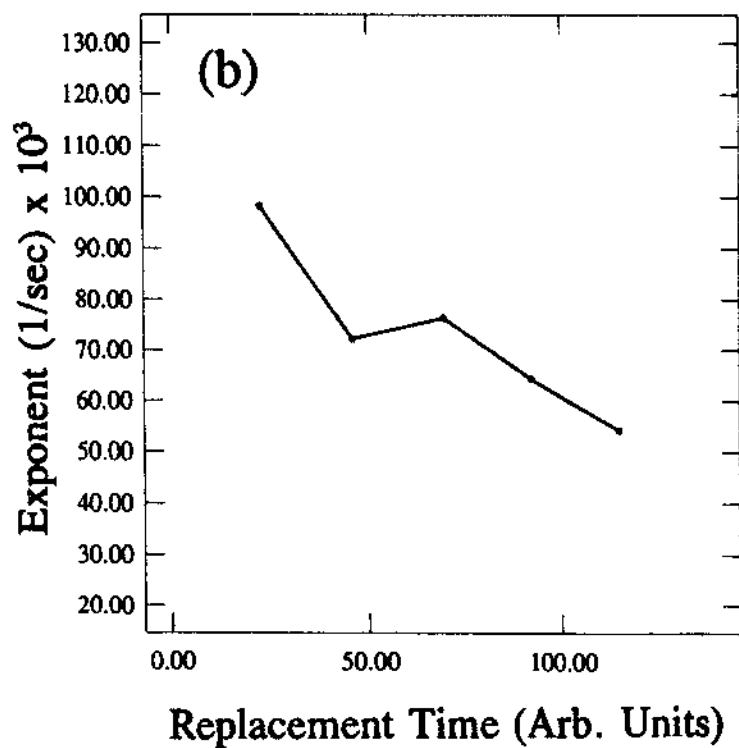
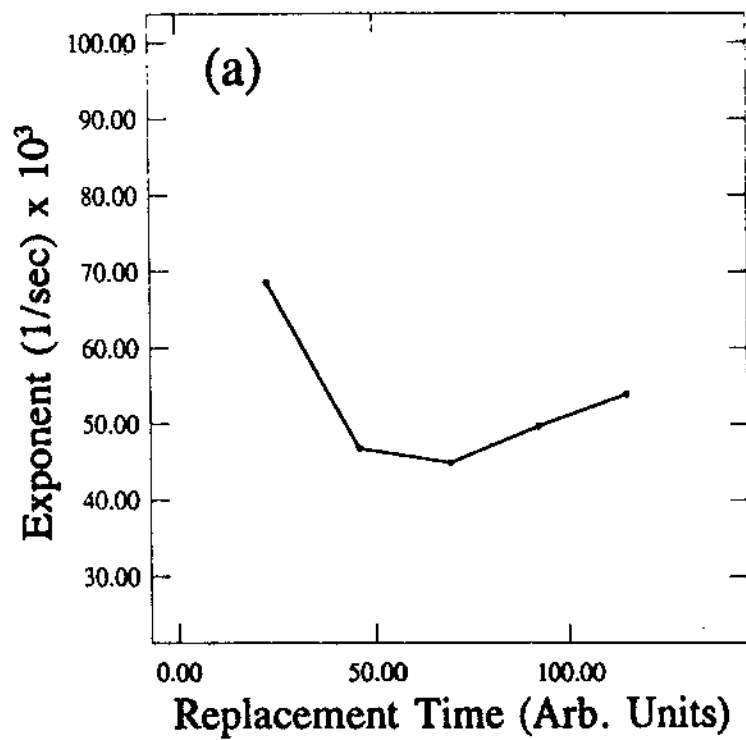


Figure 3.41 (a) Chaotic voltages entrained at $2/3$. (b) Corresponding power spectrum.

Figure 3.42 (a) Variation of the principal Lyapunov exponent with respect to replacement time for time series of Fig. 3.38(a). (b) Variation of the principal Lyapunov exponent with respect to replacement time for the time series of Fig. 3.39.



CHAPTER 4

AUTONOMOUS AND EXTERNALLY DRIVEN PERIODIC AND CHAOTIC OSCILLATIONS IN n-InSb

4.1 Introduction

Spontaneous and externally driven periodic and chaotic oscillations^[1] have been studied experimentally in a number of semiconductors: n-GaAs^[2-5], p-Ge^[6-10], high purity n-InSb^[11-13], and n-Si^[14]. Various types of periodic and chaotic oscillations were observed in these experiments including period-doubling bifurcation (Feigenbaum scenario), Hopf bifurcation to a simple periodic oscillation, and intermittency. In this chapter, further investigations on periodic and chaotic voltage oscillations in n-InSb at low temperature and under transverse magnetic field are presented.

4.2 Hüpfer and Schöll Model^[15]

The basic idea of this model is to consider both the applied field and the induced Hall field as dynamic variables whose time dependence is governed by dielectric relaxation. These two field components are linearly dependent on the carrier density. The field relaxation process combined with the generation-recombination (GR) kinetics of the carrier density yields oscillatory instabilities at a threshold value of the magnetic field.

In this theory quantum effects leading to the formation of Landau levels are neglected. The dynamics of the electric field E in this case is thus determined by :

$$\mathbf{j}_0 = \mathbf{j} + \epsilon \dot{\mathbf{E}} \quad (4.1)$$

where \mathbf{j} is the conduction current density vector, $\epsilon \dot{\mathbf{E}}$ is the displacement current density, the dot denotes the time derivative. When a magnetic field is applied perpendicular to the current density it will give rise to a Hall field E_z which leads to a spatially inhomogeneous transverse carrier density distribution. If the effect of these nonuniformities is neglected, the conduction current density can be given by^[16]

$$\mathbf{J} = en\mu\mu_B \mathbf{E} - en\mu\mu_B \mathbf{E} \times \mathbf{B} \quad (4.2)$$

where μ is the mobility of the carriers, e is the electric charge of carriers, n is the carrier density, and $\mu_B = \mu / (1 + \mu^2 B^2)$ is the mobility reduction factor due to magnetoresistance^[17]. Now choosing the coordinate system such that $\mathbf{j}_0 = (j_0, 0, 0)$ and $\mathbf{B} = (0, B, 0)$, from Eq. (4.1), Eq. (4.2) and the kinetic equation describing the generation-recombination processes one can obtain the following set of dynamic equations for the electric field components E_x , E_z , and carrier density n :

$$\begin{aligned} \epsilon \dot{E}_x &= j_0 - en\mu_B (E_x + \mu B E_z) \\ \epsilon \dot{E}_z &= en\mu_B E_z - en\mu\mu_B B E_x \\ \dot{n} &= f(n, E, B) \end{aligned} \quad (4.3)$$

Here $E = (E_x^2 + E_z^2)^{1/2}$. For a constant carrier density, Eq. (4.3) becomes a simple harmonic oscillator. However, if there exists a nonlinear dependence of n on the field \mathbf{E} , Eq. (4.3) form a three-dimensional nonlinear coupled differential system. Hüpper and Schöll showed^[15] that without the magnetic field in this system, oscillatory instabilities and chaos are found only if an AC drive is applied

or if an additional, excited impurity level is considered. But the presence of magnetic field changes this situation dramatically. Even in the case of constant mobility and a single impurity level, self-generated periodic and chaotic oscillations can be induced due to the coupling of longitudinal field with the dynamic Hall field.

To simplify the numerical simulation, one can assume that GR processes are related to a single (donor or acceptor) impurity level and restricted to thermal ionization, impact ionization, and trapping processes. Then n can be expressed as follows:

$$\dot{n} = f(n, E, B) = X_s(N_{eff,d} - n) - T_s n(n + N_a) + X_n n(N_{eff,d} - n) \quad (4.4)$$

where $N_{eff,d} = N_d - N_a$ is the effective concentrations of donors, N_a the concentration of acceptors, and X_s , T_s , and X_n are the field dependent rates for the thermal ionization, trapping, and impact ionization processes respectively.

Clearly this theory is not restricted to any particular semiconductor materials. Until now the oscillatory instabilities induced by transverse magnetic field have been experimentally found in p-Ge^[5], n-GaAs^[18], and n-InSb^[11-12]. The simulation of this Hüpper-Schöll theory based on p-Ge^{[15][19]} have shown that for some parameter values the system exhibits period doubling route to chaos. There exists a boundary that separates the oscillatory instability region with the static region in the control-parameter plane of magnetic field B versus current density j . For any fixed current density, increasing magnetic field yields a sequence of period doubling route to chaos.

4.3 Experimental Results and Discussion

Autonomous Oscillations: An overview of the autooscillatory behavior for n-InSb under transverse magnetic field is provided by the two parameter (B, j_0) phase diagram, a plot of the boundaries between oscillatory instability regimes and static regimes shown in Fig. 4.1. Increasing B upward along a line of constant current density yields a simple period-doubling sequence to chaotic regime. This result agrees very well with the theoretical simulations^{[15][19]}. (Compare the Fig. 4.1 with the Fig. 2(d) of Ref. [15]).

The experimental data were significantly contaminated with noise. Thus after obtaining time series with high speed digitizer, software filtering was used exclusively to smooth the data in the construction of wave form plots and phase plots. Fig. 4.2 shows a wave form before and after filtering. One can see that the significant portion of random noise are smoothed out while almost all components of signal itself are kept.

Typical changes induced by increasing the magnetic field B are presented in the autooscillatory time evolutions of $V_L(t)$ and $V_H(t)$ (Fig. 4.3), in their power spectra (Fig. 4.4), in their autocorrelation functions (Fig. 4.5), and in selected phase plots of $(V_L(t), V_L(t))$, $(V_H(t), V_H(t))$, and $(V_L(t), V_H(t))$ (Fig. 4.6). The DC current density supplied to the sample was held constant at $j_0 = 0.15 \text{ A/cm}^2$. The lattice temperature is kept at 1.8K.

For field close to $B = 0.5 \text{ T}$ a single periodic orbit of frequency $\approx 30 \text{ kHz}$ emerges. The time evolutions of the Hall voltage and longitudinal voltage in this regime are shown in Fig. 4.3(a) and 4.3(b) respectively. The power spectrum corresponding the time series of Fig. 4.3(a) is shown in Fig. 4.4(a), in which the first peak from left is the fundamental frequency ($\approx 30 \text{ kHz}$), and all other peaks are subharmonic oscillations. When increasing the magnetic field this

fundamental frequency will slowly increase. In the autocorrelation function Fig. 4.5(a) for the same time series as Fig. 4.4(a) one can see single periodic oscillations with very slow decay of amplitude. This decay is due to the inevitable system noise. In the phase plot Fig. 4.6(a) for the same time series of Fig. 4.3(a) the phase trajectory is approximately a single closed curve, which is the characteristic of period-1 limit cycle.

At $B = 0.55T$, a period doubling bifurcation occurs with a new frequency of $\approx 17\text{kHz}$ in addition to the fundamental frequency $\approx 34\text{kHz}$, which can be seen in power spectrum Fig. 4.4(b). Fig. 4.3(c) is the longitudinal voltage, and the signal is nearly repeated every other cycle. Fig. 4.5(b) shows its autocorrelation function; the function is oscillating with period-2 and slowly decay over time. Fig. 4.6(b) is the phase plot, in which one can see double closed curve corresponding the fundamental frequency oscillation and period-2 oscillation.

At $B = 0.4T$ a subsequent period-doubling bifurcation occurs. Now the fundamental frequency is around 72kHz , and other three peaks are located at around 18kHz , 36kHz , and 54kHz (Fig. 4.4(c)). The autocorrelation function corresponding to the same time series (Fig. 4.5(c)) has period-4, and its amplitude is decaying slowly due to the noise. Fig. 4.6(c) shows the phase plot for this period-4 oscillations, in which one can identify four closed curves.

At $B = 0.89 T$ the system is at the onset of a chaotic regime, and the wave form can be seen in Fig. 4.3(e). Its power spectrum, as shown in Fig. 4.4(d), is broad band. The correlation function of the same signal is seen to exponentially decay (see Fig. 4.5(d)). This means that the signal lose the correlation over a certain period of time, and this reflect the unpredictability

(sensitivity on initial conditions) of the chaotic system. Fig. 4.6(d) shows the phase plot in this regime. From the phase plot one can see features of converging, spreading, and folding of the system phase trajectory, which is a typical for a strange attractor.

The above sequence of transition phenomena can also be observed while one keeps magnetic field constant, and uses current density as control parameters^[20]. These results are consistent with the fact that in Hüpfer-Schöll system like n-InSb self-generated periodic and chaotic oscillations can be induced by magnetic field as predicted by Hüpfer and Schöll^[15].

Lyapunov Exponents Calculation: Stronger evidence for the existence of a chaotic regime can be provided by estimations of the Lyapunov spectrum obtained directly from the experimental time series. To accomplish this, the Wolf *et al.*^[21] algorithm (See Sec. 3.2 for details) was employed first. The sampling rate was selected as $\tau_s = 0.2\mu\text{s}$ to produce enough data points in the intervals of the rapid variation of the system relaxational signals (with typical duration of $5\mu\text{s}$), at the same time to have long enough time series for Lyapunov exponents calculations.

Data filtering allows one to show much more clearly the underlying structure of the attractor, as seen in Fig. 4.3 and 4.5. However, since heavy filtering may change the values of the Lyapunov spectrum, one has to use the unfiltered data for Lyapunov analysis. The Wolf algorithm is known to be quite sensitive to noise, consequently, the numerical stability of calculated exponents with the parameters of this routine is carefully checked. Assuming that one can build good embeddings from each of the two observed scalar signals (longitudinal and Hall voltages) one compares first the values for the maximal

Lyapunov exponents obtained from these two time series for a chaotic attractor corresponding to $B = 0.89\text{T}$ and $j_0 = 0.15\text{mA/cm}^2$. The Lyapunov exponent obtained from the longitudinal signal was estimated to be 9 (in units of the basic frequency, which was selected to be 10^5 Hz), and the best estimate for the same exponent from the Hall voltage was 2. In all of the measurements the Hall voltage was always considerably noisier than the longitudinal voltage. It is known^[21] that added noise typically lowers the value of the calculated principal exponent. This therefore explains the discrepancy of two exponents. Additionally, the numerical stability of each calculated exponent was only satisfactory when using the less noisy longitudinal signal. The positive exponent obtained indicates that the system is truly in a chaotic regime. In addition, the consistency of the order of magnitude between exponent from longitudinal voltage and that from Hall voltage provide a good example that Wolf *et al.*'s algorithm is stable for the largest Lyapunov exponent calculation.

AC-Driven system: To further investigate this dynamic system, one can added a periodic driving source to the original current source. Choosing a fixed driving amplitude and driving frequency ($f = 100\text{kHz}$), the following sequence of transitions as one increases the current density has been observed: (see Fig. 4.15 of Ref. 20) periodic oscillations with driving frequency $f_0 \rightarrow$ period doubling $f_0/2 \rightarrow$ chaos \rightarrow period $3 f_0/3$. (see Fig. 4.16 of Ref. 20) period $7 f_0/7 \rightarrow$ chaos \rightarrow periods-3 $f_0/3 \rightarrow$ chaos.

An additional interesting experiment on this system is to study the stability and the transitions from chaos to periodicity triggered by a harmonic drive of variable amplitude. It is well known that^[22] when a linear spring is driven by a harmonic driven source, the motion of the spring will oscillate with the same

frequency as the driving source, no matter what the initial condition the spring is. More importantly, the oscillating amplitude of driven spring, as well as its phase, will depend on the driving amplitude and its frequency. Suppose one was trying to obtain a fixed value oscillating amplitude A_0 for the spring. Then for any particular driving frequency f , one has to adjust the driving amplitude A_d to a certain value. Fig. 4.7 shows the dependence of this amplitude A_d versus the driving frequency f . One can see that it has a resonance minimum at the intrinsic frequency of the spring, which means that it is easier to drive the spring to a oscillation when the driving frequency is close to the intrinsic frequency of the system.

For a typical chaotic attractor, the different frequencies of the driving signals need to have different critical amplitude to make the transition from chaos to periodicity. There is a resonant frequency f_c , for which the transition from chaos to periodicity takes place at the smallest possible amplitude A_c of the driving signal. Fig. 4.8 shows the dependency of five different critical amplitudes upon their frequencies. In this case the initial fundamental frequency without the driving source is 63.5kHz, which is very close to the frequency of the minimal critical driving amplitude A_c . This stability is very similar to that of the driven harmonic oscillators shown in Fig. 4.7.

It has been conjectured^[23] that critical amplitude A_c as described above satisfies a scaling law $A_c = cK^x$, where K is the Kolmogorov entropy, c is the system dependent constant, and the exponent x is universal. Numerical experiments with several specific systems^[23] gave $x = 0.3 \pm 0.1$ with indications that x could be equal $1/3$. For a system that can be effectively described in a three dimensional state space, the Kolmogorov entropy coincides with the

positive Lyapunov exponent. To check this prediction on AC-driven n-InSb system, four different chaotic attractors were chosen by changing the magnetic field parameter, and their minimal critical driving amplitude A_c can be estimated by appropriately scanning the driving frequency. The Lyapunov exponents of the chaotic attractors were estimated by using Bryant's algorithm (See Sec. 3.1 for details). The results are summarized in Fig. 4.9, and gave $x = 0.4$. Thus the result is in excellent agreement with the numerical experiments just discussed and indicate the presence of the scaling law in these systems. Since the chaotic attractor has very few properties can be used to quantitatively characterize them, the existence of the universal scaling law as described above becomes extremely important.

4.4 Conclusions

In this chapter, the electrical oscillations in n-InSb at low temperatures under transverse magnetic field has been studied. The results are consistent with Hüpper and Schöll's theory in that there exists a boundary in the two parameter phase space (B, j_0) . This boundary separates oscillatory instability regimes from static regimes. By changing magnetic field B at a particular current density j_0 the system will follow the period doubling route to chaos. Lyapunov exponents were obtained by using Wolf *et al.*'s algorithm and found to be consistent with the observed phenomena. For the AC-driven system, the stability of a chaotic attractor was studied, and its stability to the harmonic driving source was found to be similar to that in a simple driven oscillator. The induced transitions from chaos to periodicity by AC-driving source agrees well with the conjectured scaling law for chaotic systems.

CHAPTER 4 REFERENCES

1. E. Schöll, *Nonequilibrium Phase Transitions in Semiconductors*, Springer Series in Synergetic, **Vol. 35**, Springer, Berlin, 1987.
2. G. N. Maracas, W. Porod, D. A. Jonson, and D. K. Ferry, *Physica* **134B**, 276 (1985).
3. K. Aoki, O. Ikezawa, N. Mugibayashi, and K. Yamamoto, *Physica* **134B**, 288 (1985).
4. W. Knap, M. Jezewski, J. Lusakowski, and W. Kuszko, *Solid-State Electron* **31**, 813(1988).
5. K. Aoki, Y. Kawase, K. Yamamoto, and N. Mugibayashi, *J. Phys. Soc. Jpn.* **59**, 20(1990).
6. S. W. Teitworth, R. M. Westervelt, *Phys. Rev. Lett.* **51**, 825(1983).
7. B. Rohricht, B. Wessely, J. Peinke, A. Muhlbach, J. Parisi, and R. P. Huebener, *Physica* **134B**, 281(1985).
8. J. Peinke, A. Muhlbach, B. Rohricht, B. Wessely, J. Mannhart, J. Parisi, and R. P. Huebener, *Physica* **23D**, 176(1986).
9. E. Schöll, J. Parisi, B. Rohricht, J. Peinke, and R. P. Huebener, *Phys. Lett.* **A119**, 419(1987).
10. U. Rau, J. Peinke, J. Parisi, R. P. Huebener, and E. Schöll, *Phys. Lett.* **A124**, 331(1987).
11. D. G. Seiler, C. L. Littler, R. J. Justice, and P. W. Milonni, *Phys. Lett.* **A108**, 462(1985).

12. X. N. Song, D. G. Seiler, and M. R. Loloee, *Appl. Phys.* **48**, 137(1989).
13. X.N. Song, Z. Yu, G. Albert, J.M. Kowalski, C.L. Littler and J.M. Perez. "Autonomous and Externally Driven Periodic and Chaotic Hall Voltage Oscillations in N-InSb", **Proceedings of the 1st Experimental Chaos Conference**, Arlington, VA, Oct. 1991 (World Scientific, Singapore, 1992).
14. K. Yamada, N. Takara, H. Imada, N. Miura, and C. Hamaguchi, *Solid-State Electron* **31**, 809 (1988).
15. G. Hüpper and E. Schöll, *Phys. Rev. Lett.* **66**, 2372(1991).
16. R. A. Smith, *Semiconductors* (Cambridge Univ. Press 1964), P. 129.
17. see e.g. K. Seeger, *Semiconductor Physics* (Springer 1985).
18. J. Peinke, U. Rau, W. Clauss, R. Richter, and J. Parisi, *Europhys. Lett.* **9**, 743(1989).
19. G. Albert, PhD Thesis, University of North Texas, Chapter 4, 1993
20. X.N. Song, "*Magneto-Optical and Chaotic Electrical Properties of n-InSb*", Thesis, University of North Texas, December, 1991.
21. A. Wolf, J. B. Swift, H. L. Swinney, and J. A. Vastano, *Physica* **16D**, 285(1985).
22. R. H. Abraham and C. D. Shaw, *Dynamics - The Geometry of Behavior, Part 1: periodic Behavior*, Chapter 4. (Aerial Press, Inc., 1982).
23. Yu. I. Kuznetsov, P. S. Landa, A. F. Olhovoi, S. M. Perminov, *Pokl. Akad. N. USSR*, 291 (1955) [in Russian].

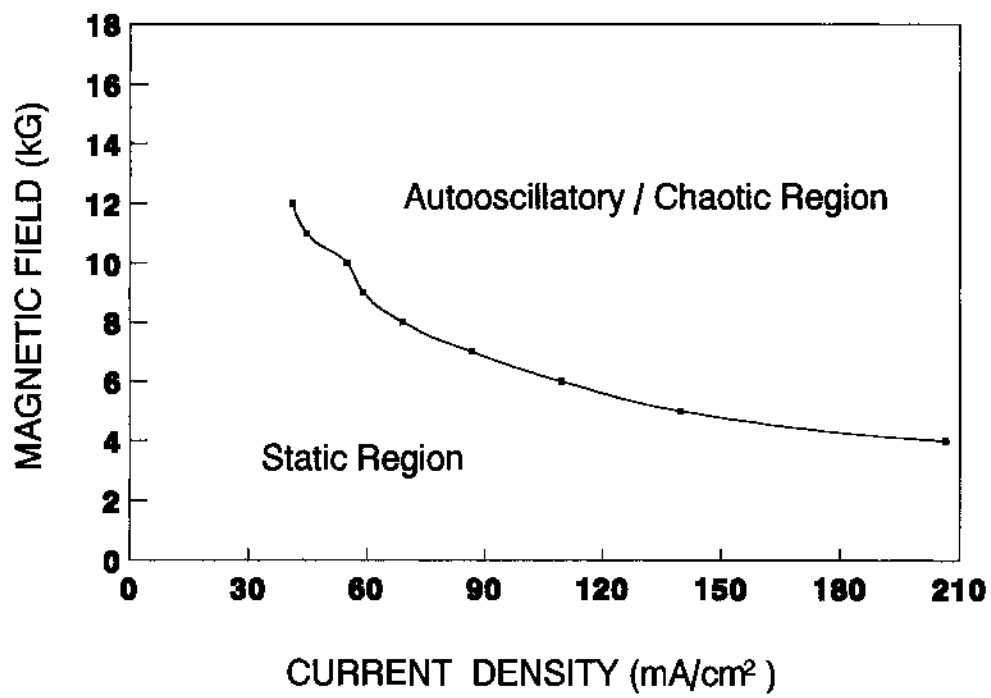
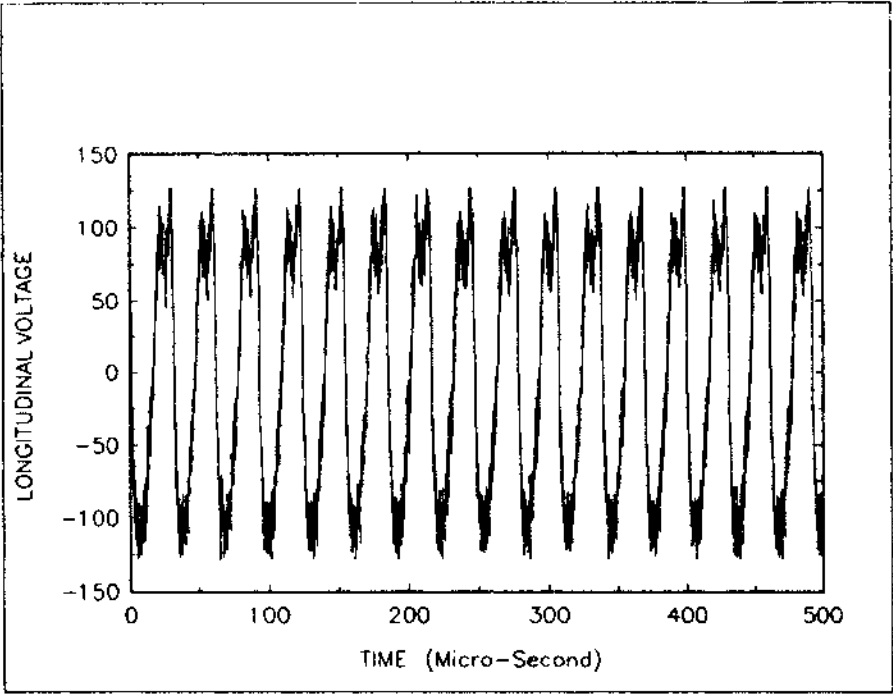
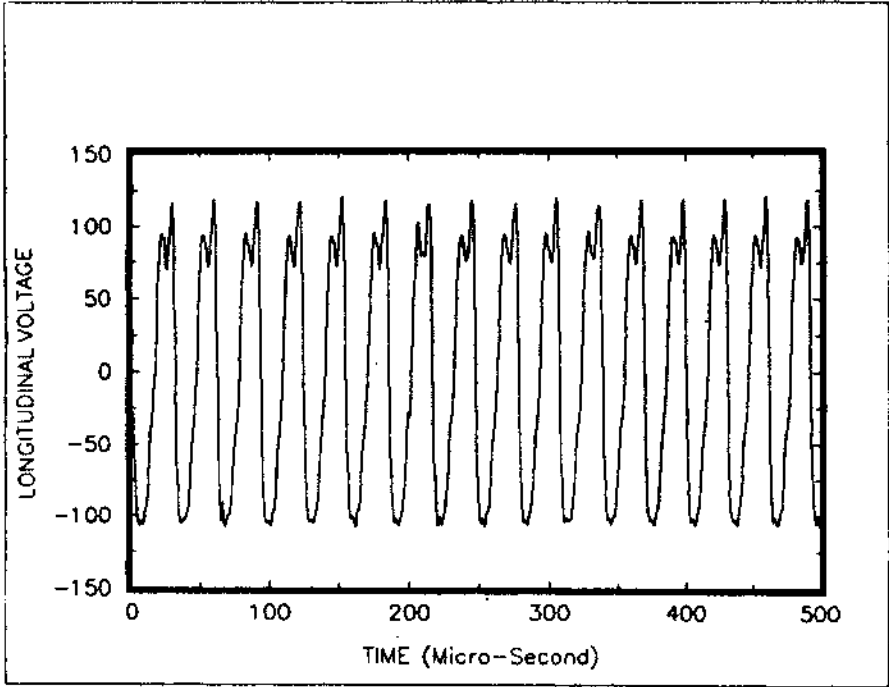


Figure 4.1 Parameter phase plot shows the boundaries between autooscillatory instability region and static region.

Figure 4.2 (a) Actual signal of longitudinal voltage taken by a high speed digitizer.
(b) The same wave form after software filtering.

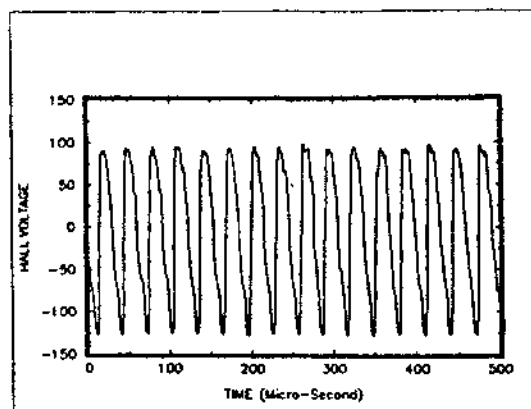


(a)

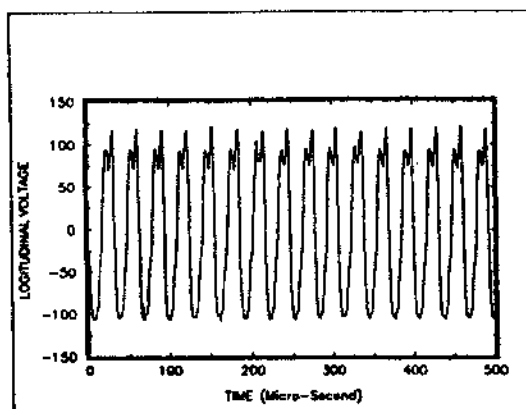


(b)

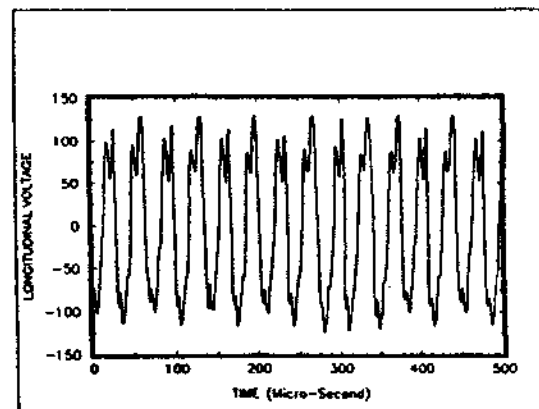
Figure 4.3 (a) Hall voltage signal for period-1 oscillation. (b) Longitudinal voltage signal for period-1 oscillation. (c) Wave form for period-2. (d) Wave form for period-4. (e). chaotic signal.



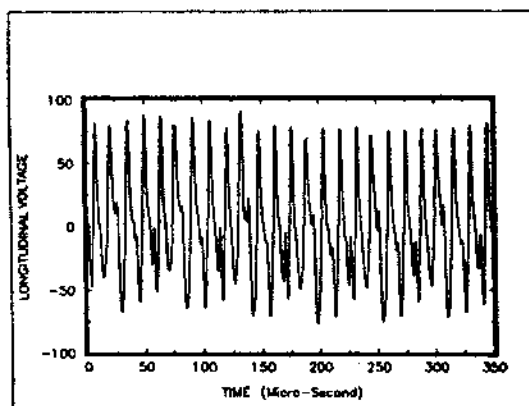
(a)



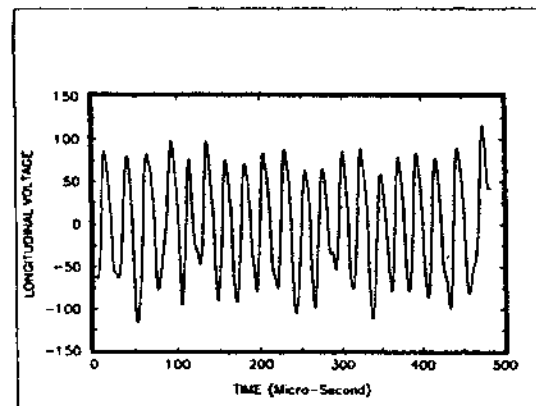
(b)



(c)



(d)



(e)

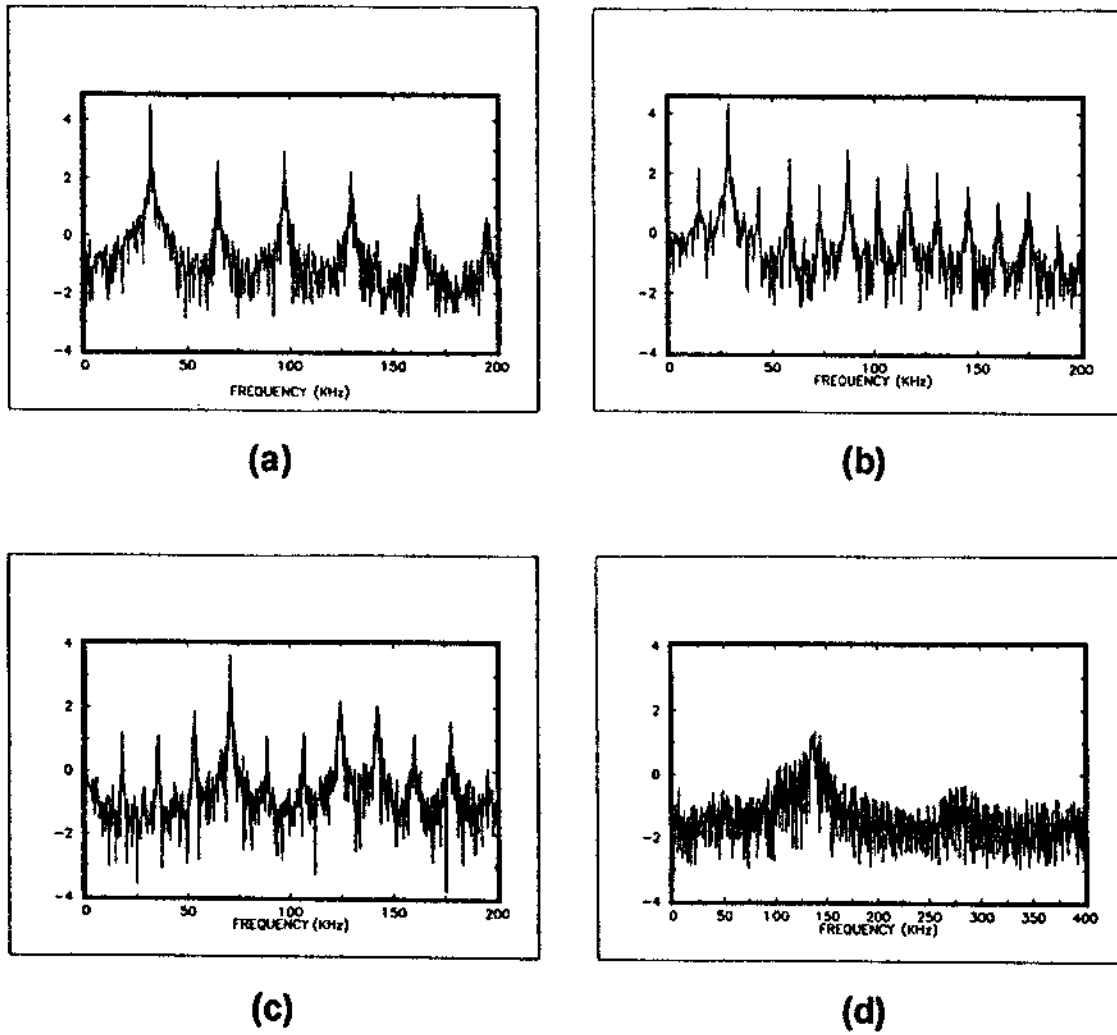


Figure 4.4 Power spectra of longitudinal or hall voltage signals for (a) period-1 oscillations, (b) period-2 oscillations, (c) period-4 oscillations, (d) chaotic regime.

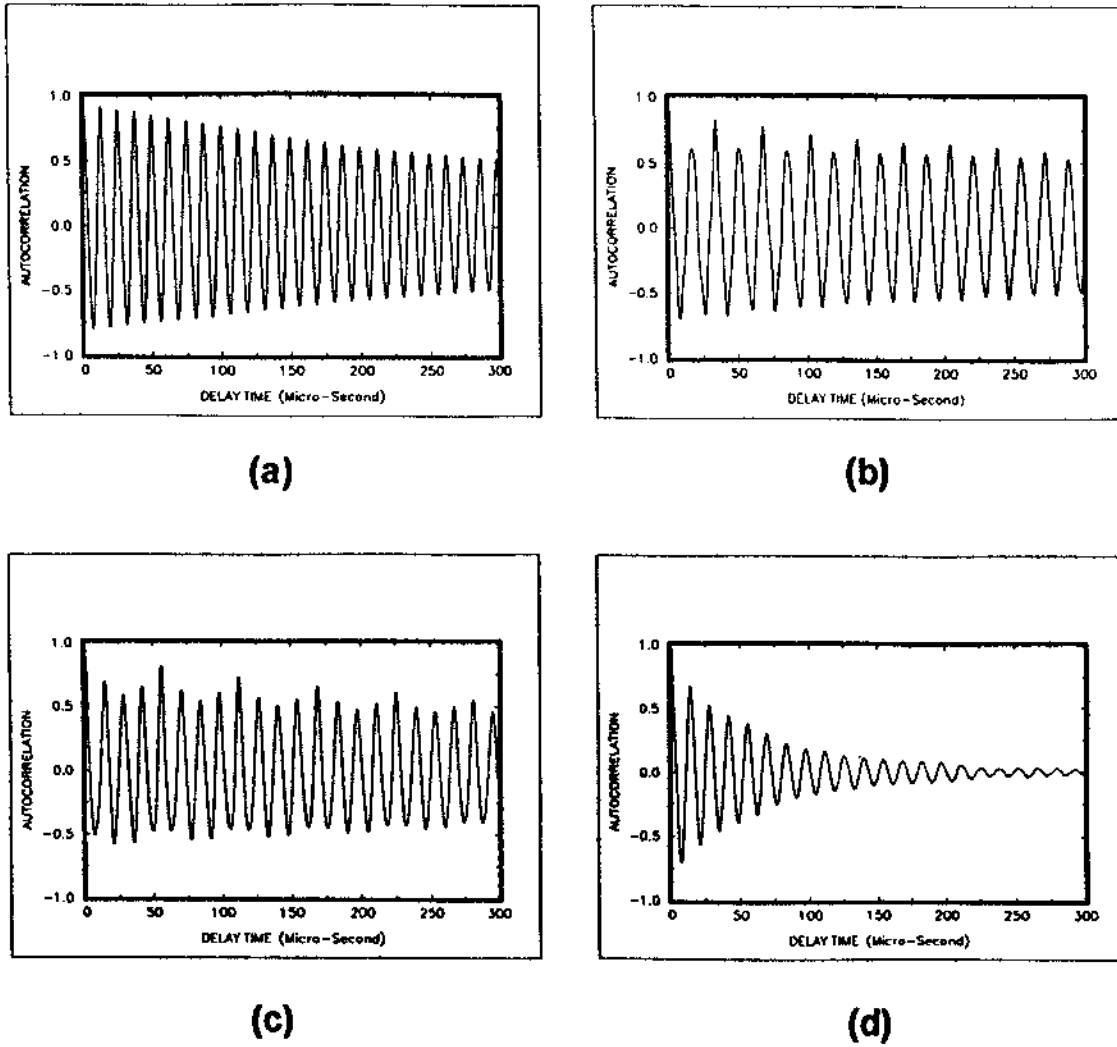


Figure 4.5 Autocorrelation functions of longitudinal or hall voltage signals for (a) period-1 oscillations, (b) period-2 oscillations, (c) period-4 oscillations, (d) chaotic regimes.

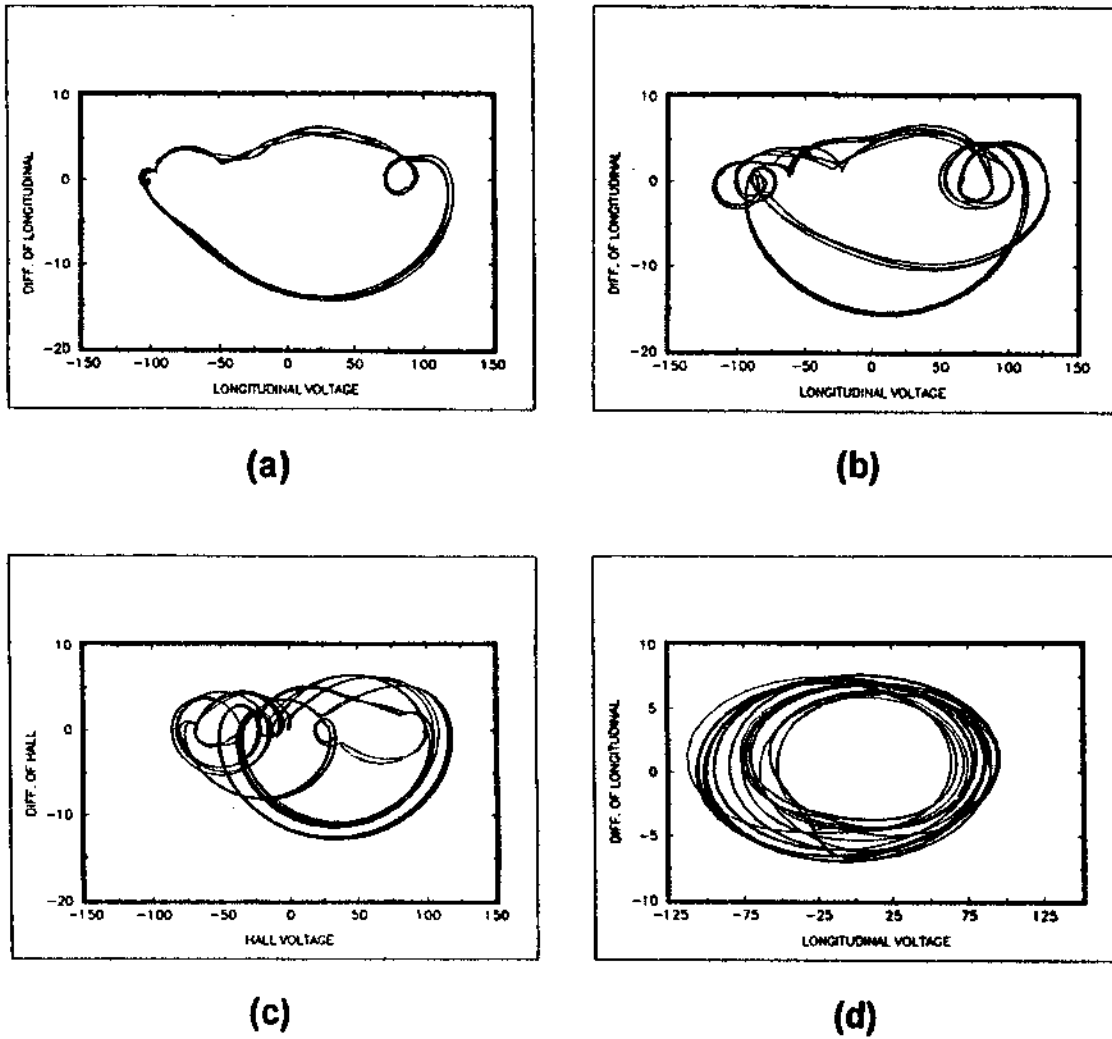


Figure 4.6 Phase portraits of longitudinal or hall voltage signals for (a) period-1 oscillations, (b) period-2 oscillations, (c) period-4 oscillations, (d) chaotic regimes.

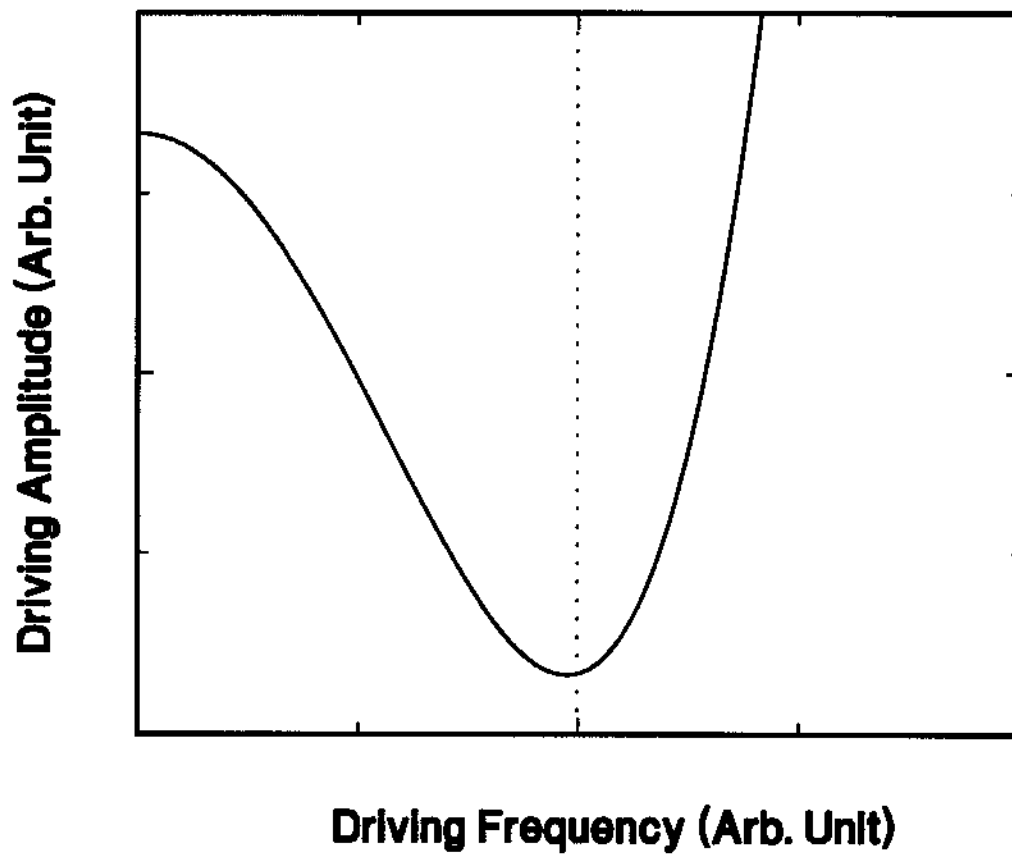


Figure 4.7 The plot of required driving amplitude A_d *versus* driving frequency f to drive a linear spring to a fixed amplitude oscillation. The dashed line represents the position of intrinsic frequency for the spring.

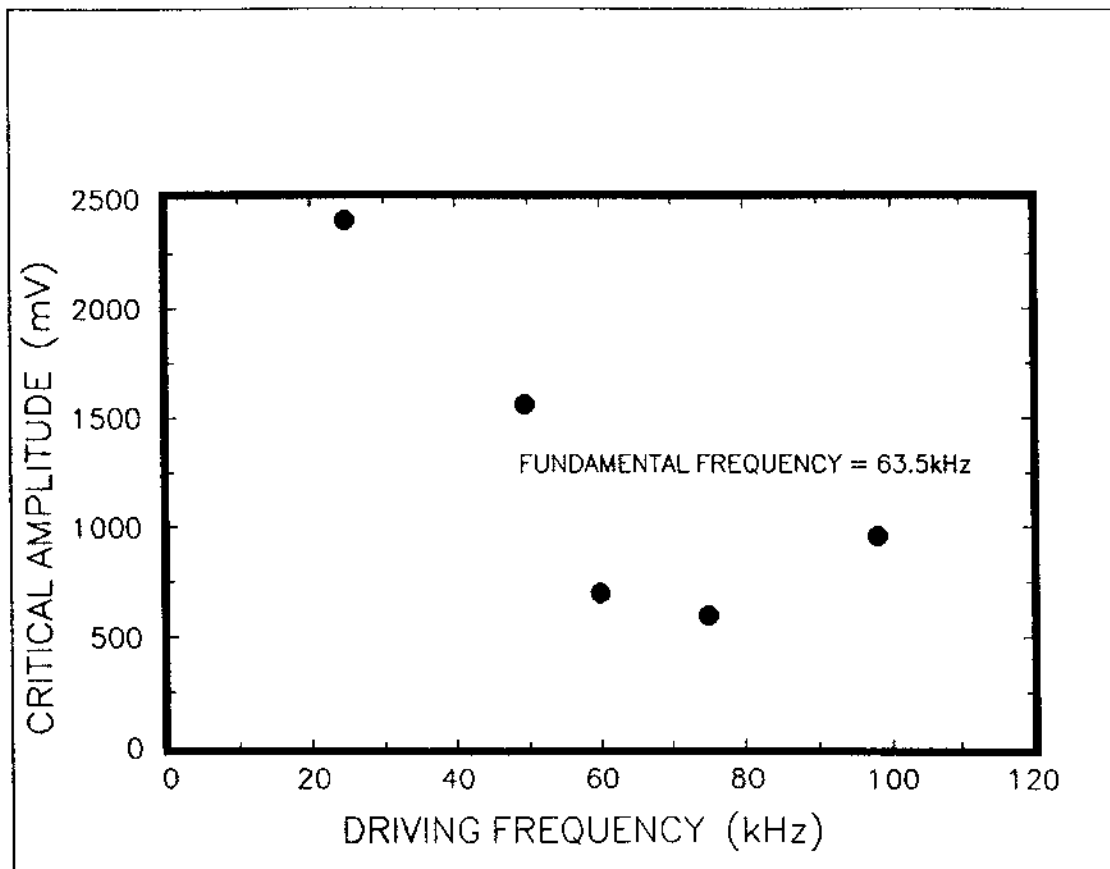


Figure 4.8 Plot of critical amplitude A_0 vs. driving frequency f_0 . Applying to the same chaotic attractor that has fundamental frequency 63.5kHz, driving source of amplitude A_0 and frequency f_0 will just destroy the chaos.

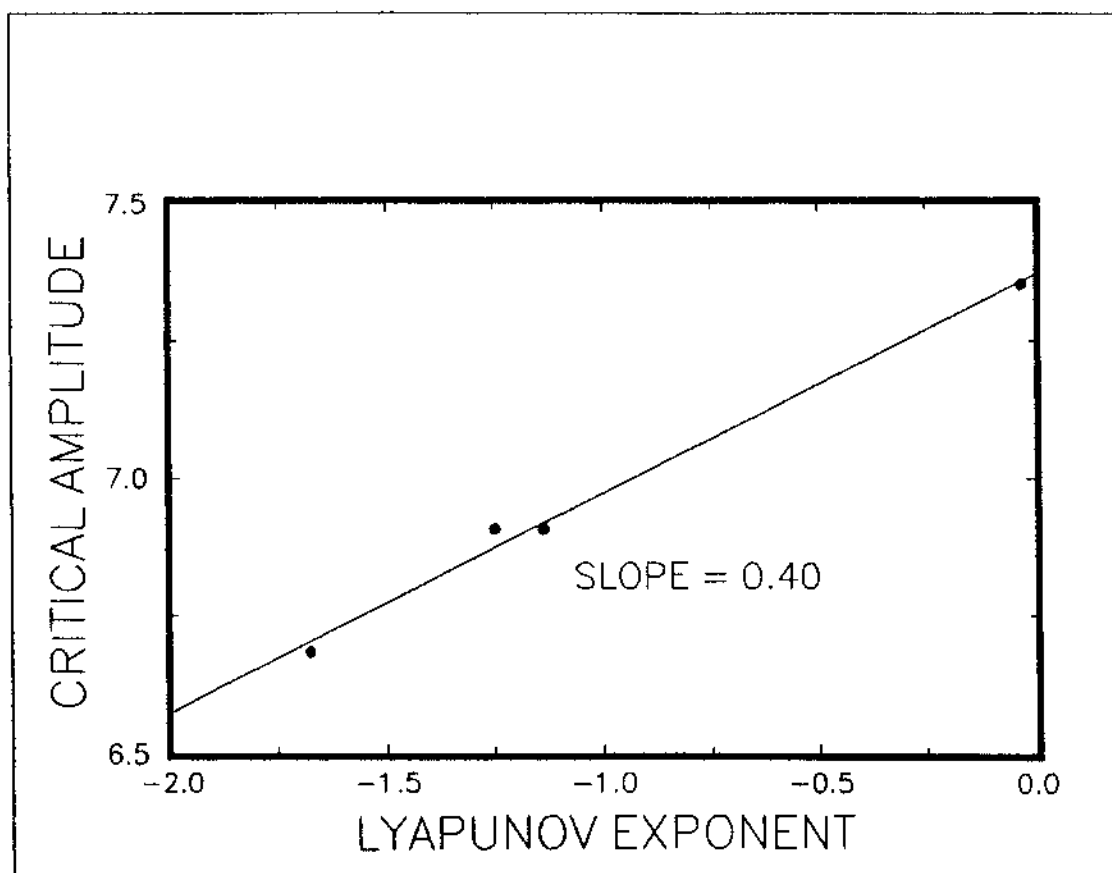


Figure 4.9 Plot of critical amplitude A_0 vs. largest Lyapunov exponent η_0 . Both axes are in log scales. Therefore $\chi = 0.4$.

CHAPTER 5

CHARACTERIZATION OF DEEP LEVELS IN $\text{Hg}_{1-x}\text{Cd}_x\text{Te}$ BY USING RESONANT IMPACT-IONIZATION SPECTROSCOPY

5.1 Introduction

For the last two decades, the ternary semiconductor $\text{Hg}_{1-x}\text{Cd}_x\text{Te}$ alloy has been used as the material of choice for the construction of the intrinsic infrared detectors in both military and commercial imaging systems. One important factor which affects the detector's response and quite often limits its performance is the presence of impurity or defect levels.^{[1][2][3]} Among these defects, those that lie deep in the forbidden gap region are very important since they can act as effective recombination centers controlling excess carrier lifetime. These deep levels can also act as centers that enhance interband tunneling, giving rise to the dark currents in intrinsic detectors based on p-n diode or metal-insulator-semiconductor (MIS) device concepts.

On the other hand, details concerning these deep level defects still remain poorly understood. In addition, these defects or impurities usually have very small absorption cross section, and they are of sufficiently low density that they are extremely difficult to detect. Deep level transient spectroscopy (DLTS) is one of the most popular techniques to study deep levels in silicon and III-V semiconductors^{[4][5][6]}. But for narrow gap semiconductors like $\text{Hg}_{1-x}\text{Cd}_x\text{Te}$, DLTS will not provide enough data points to accurately determine the energy levels. Other techniques include Thermally Stimulated Capacitance (TSC) and

Admittance Spectroscopy (AS). However, the TSC^[7] is limited by the background drift and noise due to leakage currents. Also the AS^[8] is appropriate only for majority carrier traps. It is therefore highly desirable to employ new, sensitive technique to characterize these deep level defects in $\text{Hg}_{1-x}\text{Cd}_x\text{Te}$.

The mercury (Hg) vacancy is a natural defect in HgCdTe due to the rather weakly bound nature of the Hg lattice atom and is commonly believed^[9] to act as an acceptor. The Hg vacancy concentration in HgCdTe is generally reduced from a large as-grown concentration by a post-anneal in a Hg-rich atmosphere. During this anneal, Hg atoms enter the lattice as interstitials and move through the crystal until they encounter and fill a vacancy site. Other methods such as ion-beam milling^{[10][11]} and the baking of an oxide surface exist to introduce Hg atoms as interstitials into the HgCdTe lattice and can be used to convert vacancy-doped p-HgCdTe to n-HgCdTe. Until now, a very limited amount of work has been done to study the electrical properties of Hg interstitials in HgCdTe^{[10][11]}. Recently, two methods of Hg interstitial production mentioned above (ion-beam milling and oxide baking) have been shown^[10] to produce a long-range, bias-dependent dark current in n-HgCdTe MIS devices.

A new method called RII spectroscopy was recently^{[11][12]} developed and used to investigate Hg interstitials in both bulk and LPE samples of HgCdTe with x value from 0.22 to 0.24. For $x \approx 0.22$ samples, Hg interstitials are found to be responsible for the formation of defect states near 45 meV and also appear to form states near 60 meV above the valence band edge. For $x \approx 0.24$, the Hg interstitials are found to form states near 60 meV above the valence band. These results are consistent with that obtained by using other techniques. Therefore, RII spectroscopy is a very

sensitive technique to study deep levels in HgCdTe.

In this chapter, extended investigations of Hg interstitials in both bulk and LPE samples are reported. After a theoretical discussion of RII mechanism (Sec. 5.2), the experimental results and data analysis are presented and discussed (Sec. 5.3). The final conclusions and remarks is included in Sec. 5.4.

5.2 Resonant Impact Ionization Mechanism

Resonant Impact Ionization (RII) spectroscopy is a new type of magneto-optical effect involving resonant oscillations in the photo-conductivity(PC) of semiconductor due to impact ionization of valence electrons. This form of spectroscopy has a unique magneto-optical signature, that is that the peak positions of PC response are independent of laser photon energy.

Fig 5.1 shows a typical wavelength dependence of both One Photon Magneto-Absorption (OPMA) and RII spectra for an $x = 0.24$ bulk sample. The RII resonances are those between 1.5T and 3.0T, and they do not shift with incident laser wavelength. On the other hand, the two peaks that appear at higher magnetic fields are due to OPMA and impurity-to-band magneto-optical transitions, and they are seen to shift rapidly with the laser wavelength. Note that if the photon energy is less than the separation between the highest Landau level in the valence band and the lowest in the conduction band, the PC signal becomes very small, the remaining signal due only to Impurity Magneto-Absorption(IMA) and Two Photon Magneto-Absorption(TPMA) processes.

The transition energies for OPMA, including the exciton corrections, can be calculated by using Pidgeon-Brown model^[13]. These calculations can be fitted

to the OPMA data from the experiment and used to determine the energy gap of the sample E_g .

In order to understand the resonance condition that lead to the RII oscillations, the electronic band structure of a semiconductor material under transverse magnetic field is schematically illustrated in Fig. 5.2. Electrons are photoexcited across the energy gap via strong one photon magneto-absorption(OPMA), creating a large photoexcited population of electrons in the conduction band. Some of these photoexcited electrons are then subsequently excited well into the conduction band by the absorption of a second photon. For a RII resonance, the transition energies ΔE_{LL} between conduction-band Landau levels must equal the transition energies ΔE_{II} between the highest Landau-valence-band Landau level and an impurity or trap level in the gap. Thus, the process involves the resonant relaxation of conduction-band electrons via impact ionization of a valence electron into a trap level. Landau levels that are more than a photon energy above the lowest conduction-band Landau level are not effectively populated and do not contribute. In the RII process, changes in mobility occur whenever the electron makes a resonant transition from higher-lying Landau level to a lower-lying one. Since the conduction band of these narrow-gap HgCdTe samples is highly nonparabolic, the mobility increases rapidly with increasing energy as measured from the bottom of the conduction band. Thus, resonant peaks in the PC response are seen whenever the RII mechanism is present, and it does not depend on the incident photon energies.

In order to calculate the magnetic field positions of RII resonances, a computer program was written to incorporate the code that calculate Landau level energies over magnetic field and to search for the impurity energy level and

field positions that satisfy the RII resonance condition. The sequence of the algorithm is illustrated as follows:

(1) Calculate both the conduction-band and valence-band Landau level energies for a wide range of quantum number n and over the appropriate magnetic field range.

(2) Input a range of impurity energy levels $[E_i, E_f]$ and energy incremental step ΔE .

(3) Input a range of magnetic field $[B_i, B_f]$ and magnetic field incremental step ΔB .

(4) Input the experimental magnetic field positions (B_1, B_2, \dots, B_k) for the RII resonances.

(5) Given a impurity energy level E , do the following: For every magnetic field B (start from B_i and increment by ΔB each time), compare the difference of E and highest ($n = 0$) valence-band Landau level energy (which is E_{ij}) with the difference of each pair of conduction-band Landau levels (which is E_{il}). If $|E_{ij} - E_{il}|$ is less than a predefined constant ϵ_E and the magnetic field B can match any of the input field positions b_i within a predefined uncertainty ϵ_B , a match is found and the energy E , the magnetic field B and the conduction band Landau level numbers are output as a candidate for the RII resonance. Otherwise, increment the magnetic field by ΔB and repeat the comparison again, until the magnetic field reaches B_f .

(6) Increment impurity energy E by ΔE . If this E is less than E_f , go back to (5), otherwise terminate the program.

Usually many matches can be found from this procedure for some uncertainty parameters ϵ_E and ϵ_B . Further confirmation of a particular level E

comes from searching the successive matching of a multitude of field positions yielding approximately the same energy E . Thus, the preciseness of individual matchings is not as important as the trend of matches to the same energy. In addition, since there are usually more than one trap level in each sample, the spectra represent a superposition of peaks which at lower fields become unresolved.

5.3 Experimental Results and Discussion

To study the effect of Hg interstitials, a control sample and a "doped" sample were prepared from a same piece of bulk crystal. The "doped" samples were prepared in such a manner to have a large Hg interstitial concentration as compared to control sample. Fig. 5.3 shows the spectra obtained from both the control and the "doped" $x \approx 0.22$ samples at a temperature of 5K. In spectra A (the control sample), the only resonances seen are due to OPMA, which would be expected for a sample with very low amounts of impurity or defects levels. The verification that this structure arises from OPMA processes is seen in Fig. 5.4 and Fig. 5.5. Fig. 5.4 shows the wavelength dependence of the observed structure. Fig. 5.5 shows the fit of this set of data to calculated OPMA transition energies resulting in an energy gap of 105 ± 2 meV for this sample.

In spectra B (Fig. 5.3), the structure seen is entirely different; the resonance peaks in the PC response do not shift with laser wavelength. These resonances are thus due to the RII process. In this figure, the RII structure dominates and obscures the OPMA resonances seen in the spectra A. In addition, the RII peaks seem to be superimposed on a broader resonance, centered about $B = 2.0T$. This broad resonance is similar to that seen by Ipposhi

et al^[14], and is possibly due to magnetophonon resonance trapping of excess carriers involving the emission of LO phonons by a Shockley-Read center.

The resonant field positions of the RII spectra can be used to estimate the deep trap levels, and the results are listed in Table 5.1. The trap levels responsible for spectra A, upon analysis, are found to be at ≈ 44 and ≈ 59 meV above the valence band, which is consistent with values obtained by using other technique^[15]. Therefore these results show that deliberately "doped" Hg interstitials in HgCdTe produce deep trap levels in $\text{Hg}_{1-x}\text{Cd}_x\text{Te}$.

In addition to the OPMA resonances seen in Fig. 5.4, an additional weak resonance is seen as a "shoulder" at the high-field end of most of the spectra. The transition energies versus magnetic field for this peak are represented by the open squares lying about 4 meV below the lowest OPMA transition shown in Fig. 5.5. These are due to the effect of bound excitons. Bound excitons are typically difficult to observe in narrow-gap semiconductors because of the extremely small binding energy of the complex. However, a similar transition has been seen in n-InSb^[16], and it corresponded to an exciton bound to a neutral acceptor level. One way^[17] that has been used to determine the nature of the bound-exciton complex is to compare the observed binding energy of the complex with simple theoretical estimates of the four possible complexes. The four cases and their binding energies are^[18] as follows:

$$D^+x \text{ (exciton bound to an ionized donor)} = 0.06E_d$$

$$D^0x \text{ (exciton bound to a neutral donor)} = 0.13E_d$$

$$A^0x \text{ (exciton bound to a neutral acceptor)} = 0.07E_a$$

$$A^+x \text{ (exciton bound to an ionized acceptor)} = 0.4E_a$$

For RII model to be valid the complex center must be able to receive electrons,

i.e., an ionized donor, therefore the bound excitons can't be A^+x . Also, D^0x and A^0x can also be ruled out from energy considerations. Thus, using 59 meV as donor energy E_d , then the D^+x bound-exciton has energy of ≈ 3.5 meV, which is in good agreement with the observed ≈ 4 meV binding energy. Presumably, the donor level in this case is ionized by the intense laser irradiation which produces transitions from the ≈ 59 meV level to the conduction band.

Rll structure is also seen in another bulk sample of $x \approx 0.24$ as shown in Fig. 5.6(a). This structure is presumably due to residual Hg interstitials that were introduced during the recrystallization step of this sample's growth. For the purpose of this investigation Hg interstitials were deliberately added to one of the pieces of this sample to study how additional Hg interstitials would effect the Rll resonances. In Fig. 5.6 (b), the Rll spectra for this "doped" sample was plotted to compare with the control spectra (Fig. 5.6(a)). Note that for the field range shown in the Fig. 5.6, the peaks in both spectra occur at essentially the same magnetic field positions, but the resonances appear stronger in the "doped" sample. Fig. 5.7 shows the same spectra with monotonic background for each sample remove by fitting approximate Gaussian peaks to the original spectra. Clearly, the resonances are stronger (by about a factor of 2) in the Hg 'doped' sample, indicating that the introduction of Hg interstitials increases the population of the trap levels responsible for the peaks shown (or Rll structure).

Fig. 5.8 shows a comparison of TPMA resonances obtained from the same control and "doped" sample as discussed above ($x \approx 0.24$). The TPMA lifetimes were also determined by examining the PC decay and were seen to be $\approx 250\mu s$ for the control and $\approx 150\mu s$ for the "doped" sample. It is clearly seen that the TPMA resonance (spectra B) for the "doped" sample is substantially

stronger than the control sample (spectra A). It is well known^[19] that the two-photon absorption constant $\beta(\omega)$ is proportional to a second-order matrix element $r_{cv}^{kk'}$ in the perturbation theory:

$$r_{cv}^{kk'} = \sum_n \frac{p_{cn}^k p_{nv}^{k'}}{h\omega - (\epsilon^c(\mathbf{k}) - \epsilon_n)} \quad (5.1)$$

where ϵ_n is the energy of an intermediate level n and $\epsilon^c(\mathbf{k})$ is the energy of electron in the conduction band (all the energies are measured from the bottom of the conduction band); p_{cn}^k and $p_{nv}^{k'}$ are the matrix elements of the electron momentum operator. From the above equation (Eq. 5.1) one can see that the absorption constant $\beta(\omega)$ should rise strongly near the absorption edge in the presence of an impurity level located near the middle of the forbidden energy gap, *i.e.*, these intermediate states are provided by the impurity level, and these deep levels are located at $\epsilon_n \approx -E_g/2$. Thus, the addition of trap levels at approximately mid-gap has effectively increased the TPMA transition strength by providing more near-resonant intermediate states for the TPMA transitions. Therefore the enhancement of TPMA for "doped" sample in Fig. 5.8 is consistent with the results from RII spectra that the addition of Hg interstitials increased the concentration of deep trap levels.

The RII peak positions from the complete spectra were obtained by using magnetic-modulation and lock-in-amplifier techniques, which yields more RII positions. The results for both control sample and "doped" sample are tabulated in Table 5.2. For the control sample, two levels were obtained by a best fit: one at ≈ 16 meV and one at ≈ 61 meV. The 16 meV activation energy corresponds closely with that of the lowest Hg vacancy level^[20], and the 61 meV level lies

close to the middle of the gap for this $x \approx 0.24$ sample. However, upon analysis of the "doped" sample, only 61 meV level can be found from the spectra. Since the introduction of additional Hg interstitials should not only create additional trap levels but also fill some of the remaining Hg vacancies in the sample, one would expect to see both an increase in the trap concentration and a decrease in vacancy concentration, resulting in the observed spectral feature shown in Fig. 5.6 and the absence of the vacancy level in the doped sample in Table 5.2.

RIL resonances have also been observed in LPE samples. Fig. 5.9 and Fig. 5.10 shows wavelength dependence of the spectra obtained from a $x \approx 0.22$ sample of LPE $\text{Hg}_{1-x}\text{Cd}_x\text{Te}$. This sample was subjected to numerous damaging fabrication steps, e.g., devices were fabricated on this film and then removed, and anodic oxides were grown, baked and then removed. Finally, for this study, anodic oxide was grown, Hall bars were delineated and metalization deposited. Note that the spectra seen in Fig. 5.9 and Fig. 5.10 are almost identical to that of spectra B of Fig. 5.3, a bulk $x \approx 0.22$ sample. Fig. 5.11 shows the theoretically calculated transition energies for OPMA and experimental absorption peaks for the same LPE sample as Fig. 5.9 and Fig. 5.10. It can be seen that some of the peaks are possibly OPMA, while other peaks fall on five different vertical lines, *i.e.* they do not depend on photon energy. So they are due to the RIL mechanism. In addition, the energy gap of this sample is 99.5 meV from the calculation, thus the x -value is ≈ 0.22 . This energy gap and x -value is confirmed by FTIR measurements performed at Texas Instruments, Inc.

Again, the impurity levels responsible for the RIL peaks were estimated, and the result is listed in Table 5.3. One can see that there are three deep levels: 40 meV, 45 meV and 59 meV. These results are consistent with those

for the bulk samples. It is important to note that in Table 5.3, any one of the deep levels are responsible for multiple resonance field positions; e.g., 2.53T, 3.08T, 5.50T, and 8.31T are all caused by 40 meV level. On the other hand, each resonance position might contributed by several resonances from different deep levels, e.g., all three deep levels can contribute to the resonance position of 3.08T.

This LPE sample was also subjected to a 140°C bake to "dope" the sample with additional Hg interstitials. Fig. 5.12 shows the comparison of spectra before and after a bake. It can be seen that the RII resonances are larger in the baked sample. This result is similar to the results from the bulk sample, where additional Hg interstitials were shown to provide more deep trap levels and enhance the RII transition strengths.

Another LPE sample of $x \approx 0.22$ was passivated with a sulfide rather than an oxide in order to investigate the effects resulting from the introduction of the Hg vacancies rather than Hg interstitials. Since the passivation layer is a sulfide rather than an oxide, no Hg interstitials will be created by a high temperature bake. Fig. 5.13 shows the resonance peak positions obtained from magneto-optical spectra for unbaked LPE sample. It also shows the calculated OPMA transition energies calculated. One can see some of the peaks are fitted with OPMA transitions. But there are clearly some other peaks caused by RII transitions. From the data fit, the energy band gap for this sample is determined as around 89.5 meV.

Similarly, the experimental peaks and calculated OPMA transition energies for the same sample after a bake at 220°C are shown in Fig. 5.14. Now, all of the peak positions are described well by OPMA, and there are no RII structures.

The energy gap for this baked sample is around 88.2 meV, which is slightly less than that before the sample was baked.

Fig. 5.15 shows the spectra obtained from an $x \approx 0.23$ sample of LPE $\text{Hg}_{1-x}\text{Cd}_x\text{Te}$. This sample was obtained from a sample which was grown from a melt in which indium was included as a dopant at a concentration of $\approx 5 \times 10^{14} \text{cm}^{-3}$. The broad set of OPMA resonances are seen to shift with laser wavelength. The results of a band-model analysis, shown in Fig. 5.16, yield two distinct energy gaps: one at ≈ 111 meV and the other at ≈ 120 meV. It is known that in LPE HgCdTe there sometimes exists a graded energy gap near the CdZnTe substrate interface. Thus the resonances which yield the higher gap presumably come from OPMA in the region near the interface, whereas the lower energy gap resonances are representative of the bulk of the remaining sample region.

Fig. 5.17 shows spectra from an $x \approx 0.24$ LPE sample which was not doped with indium. Note that the resonances resemble that of the RII spectra; *i.e.* the resonances positions do not shift with laser wavelength. The results of an RII analysis on these peaks yields a trap level of approximately 58 meV for this sample (the energy gap for this sample $E_g = 126$ meV at 5K). Indium incorporation in LPE HgCdTe is known^[21] to improve device or detector properties; therefore the above experimental results provide evidence for the reduction of the trap levels via incorporation of indium in the melt.

5.4 Conclusions and Final Remarks

RII spectroscopy has been used to investigate impurity and defect (trap) levels that presumably are caused by Hg interstitials in both bulk and LPE

crystals of $\text{Hg}_{1-x}\text{Cd}_x\text{Te}$. Hg interstitials were deliberately introduced into bulk samples with $x \approx 0.22$ and $x \approx 0.24$. RII spectroscopy provide direct evidence for the formation of trap levels near 45 and 60 meV above the valence band edge for the $x \approx 0.22$ sample, and near 60 meV for the $x \approx 0.24$ sample. The 60 meV level in the $x \approx 0.24$ ($E_g = 121$ meV at 5K) sample is seen to enhance the transition strength of resonant TPMA observed at high fields by acting as a near-resonant intermediate state for the two-photon transition process. In addition, the weak resonance peaks in most of the spectra for $x \approx 0.22$ bulk samples were identified as due to the effect of excitons are bound to ionized donors.

For the LPE samples that have Hg interstitials introduced during the post-anneal in Hg-rich atmosphere, their RII spectra show that there are three deep levels: 40 meV, 45 meV and 59 meV. Baking the LPE sample with a oxide layer introduces more Hg into the samples and produces stronger RII resonances. On the other hand, baking the sample that does not have a oxide layer, causing the Hg interstitials to either fill some vacancies or be drive out of the sample, make the RII structures disappeared. All these results consistently show that Hg interstitials in both bulk and LPE $\text{Hg}_{1-x}\text{Cd}_x\text{Te}$ create deep trap levels in these materials. Thus, RII spectroscopy is a very sensitive technique to investigate deep energy levels caused by Hg interstitials in $\text{Hg}_{1-x}\text{Cd}_x\text{Te}$. This technique is generally applicable to the investigation of other defects and impurities in HgCdTe as long as the trap levels created are accessible via the RII mechanism.

$B^{\text{expt}}(\text{T})$ ($\pm 0.02\text{T}$)	$B^{\text{theory}}(\text{T})$	Transitions	$\Delta E_{\parallel}(\text{meV})$
1.26	1.20	$7 \rightarrow 2$	43.4
1.39	1.36	$8 \rightarrow 3 ; 5 \rightarrow 1$	43.5
	1.52	$3 \rightarrow 0$	43.5
1.65	1.62	$9 \rightarrow 4 ; 6 \rightarrow 2$	43.5
1.93	1.94	$7 \rightarrow 3 ; 4 \rightarrow 1$	43.6
2.30	2.25	$8 \rightarrow 4 ; 2 \rightarrow 0$	43.7
	2.47	$5 \rightarrow 2$	43.8
2.84	2.89	$6 \rightarrow 2 ; 4 \rightarrow 1$	58.0
	3.02	$6 \rightarrow 3$	44.0
3.57	3.47	$3 \rightarrow 1$	44.2
	3.59	$2 \rightarrow 0$	58.2
4.73	4.76	$4 \rightarrow 2$	44.6
5.83	5.73	$3 \rightarrow 1$	58.9
8.20	8.37	$4 \rightarrow 2 ; 1 \rightarrow 0$	59.8

Table 5.1 Comparison of experimental B^{expt} and theoretical B^{theory} magnetic field positions for the $x \approx 0.22$ bulk sample, along with the transitions and the impact-ionization energies ΔE_{\parallel} .

	$B^{\text{expt}}(\text{T})$ (± 0.02)	$B^{\text{theory}}(\text{T})$	Transitions	$\Delta E_{\parallel}(\text{meV})$
Control Sample	0.49	0.52	$3 \rightarrow 0$	16.7
	0.78	0.80	$2 \rightarrow 0$	16.8
	1.36	1.44	$9 \rightarrow 2$	61.5
	1.69	1.70	$1 \rightarrow 0 ; 8 \rightarrow 2$	17.1 ; 61.5
	1.90	1.91	$6 \rightarrow 1$	61.6
	2.11	2.02	$4 \rightarrow 0 ; 9 \rightarrow 3$	61.7
	2.34	2.26	$7 \rightarrow 2$	61.8
	2.75	2.74	$3 \rightarrow 0$	61.9
Doped Sample	1.42	1.44	$9 \rightarrow 2$	61.5
	1.50	1.55	$5 \rightarrow 0 ; 7 \rightarrow 1$	61.5
	1.66	1.69	$8 \rightarrow 2$	61.5
	1.83	1.91	$6 \rightarrow 1$	61.6
	2.01	2.02	$4 \rightarrow 0 ; 9 \rightarrow 3$	61.7
	2.30	2.26	$7 \rightarrow 2$	61.8
	2.63	2.57	$5 \rightarrow 1 ; 8 \rightarrow 3$	61.9
	2.78	2.74	$3 \rightarrow 0$	61.9
	3.13	3.12	$6 \rightarrow 2 ; 9 \rightarrow 4$	62.0
	3.60	3.72	$4 \rightarrow 1 ; 7 \rightarrow 3$	62.2

Table 5.2 Comparison of experimental B^{expt} and theoretical B^{theory} magnetic field positions for the $x \approx 0.22$ bulk control and "doped" sample, along with the transitions and the impact-ionization energies ΔE_{\parallel} .

B^{expt}	B^{theory}	Trnasitions	$\Delta E_{\parallel}(\text{meV})$
2.53	2.54	$10 \rightarrow 6$	40.0
3.08	3.07	$3 \rightarrow 1; 7 \rightarrow 4$	40.0
5.50	5.50	$5 \rightarrow 3$	40.0
8.31	8.30	$7 \rightarrow 5$	40.0
2.53	2.53	$2 \rightarrow 0$	45.0
3.08	3.08	$10 \rightarrow 6$	45.0
3.98	3.98	$7 \rightarrow 4$	45.0
5.50	5.51	$9 \rightarrow 6$	45.0
3.08	3.07	$10 \rightarrow 5$	58.0
3.98	3.99	$8 \rightarrow 4$	58.0
5.50	5.51	$6 \rightarrow 3; 10 \rightarrow 6$	59.0
8.31	8.30	$8 \rightarrow 5$	59.0

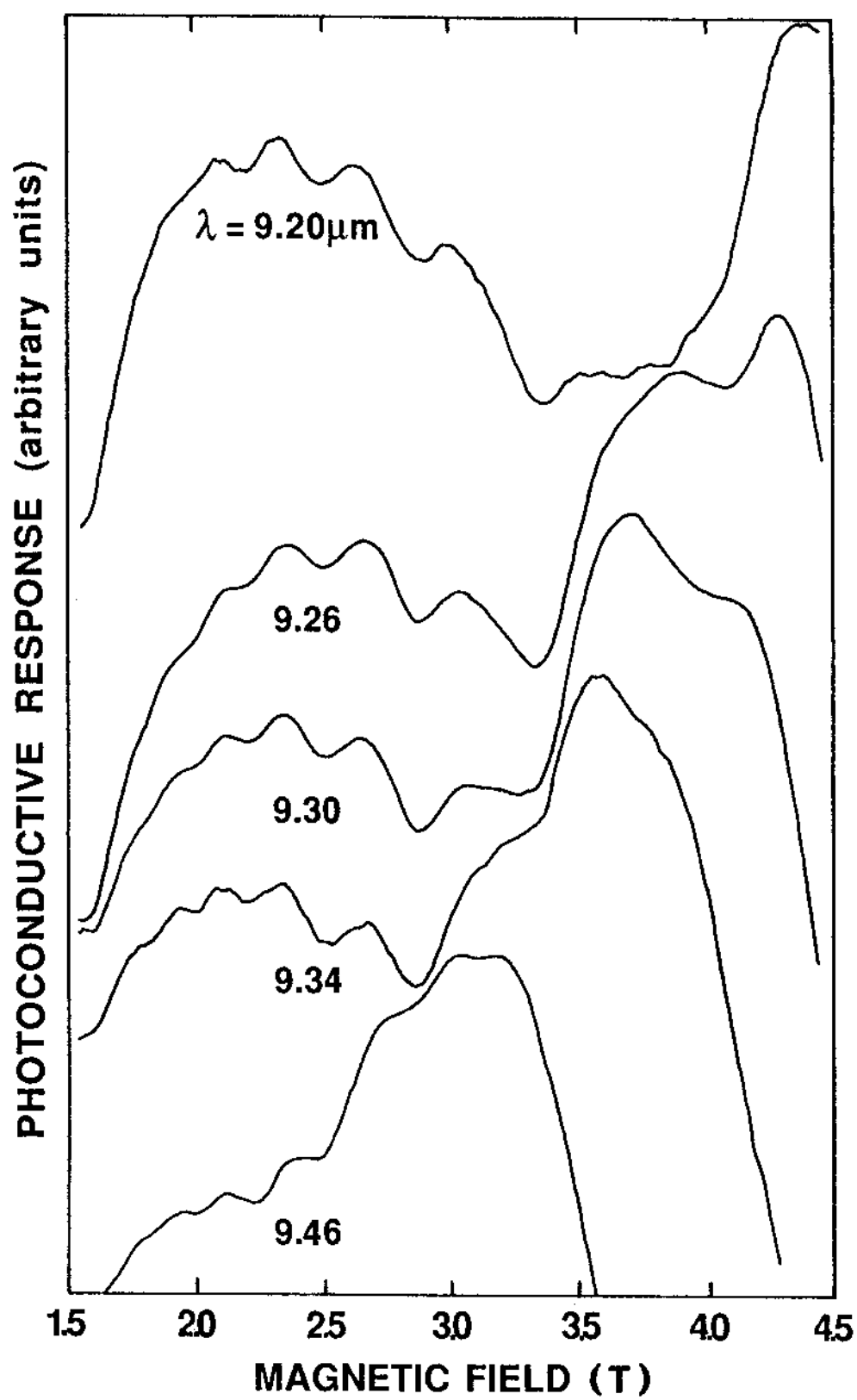
Table 5.3 Comparison of experimental B^{expt} and theoretical B^{theory} magnetic field positions for the $x \approx 0.22$ LPE sample, along with the transitions and the impact-ionization energies ΔE_{\parallel} .

CHAPTER 5 REFERENCES

1. D.L. Polla and C.E. Jones, Solid State Commun. **36**, 809(1980).
2. A.T. Hunter, D.L. Smith, and T.C. McGill, Appl. Phys. Lett. **37**, 200(1980).
3. C.E. Jones, V. Nair, and D.L. Polla, Appl. Phys. Lett. **39**, 248(1981).
4. D.V. Lang and R.A. Logan, J. Electron Mater. **4**, 1053(1975).
5. B.L. Smith, T.J. Hayes, A.R. Peaker, and D.R. Wright, Appl. Phys. Lett. **26**, 122(1975).
6. G.L. Miller, D.V. Lang, and L.C. Kimerling, Ann. Rev. Mater. Sci. 377-448(1977).
7. D.L Polla and C.E. Jones, J. Appl. Phys. **51**, 12(1980).
8. C.T. Sah, Solid State Electron. **19**, 975(1977).
9. W. Scott, E.L. Stelzer and R.J. Hager, J. Appl. Phys. **47**, 1408(1976).
10. J. L. Elkind J. Vac. Sci. Technol. **B10**, 1460(1992).
11. C.L. Littler, X.N. Song, Z. Yu, J.L. Elkind, D.J. Seiler, and J.R. Lowney, J. Vac. Sci. Technol. **B10**, 1466(1992).
12. C.L. Littler, X.N. Song, Z. Yu, J.L. Elkind, J.R. Lowney, Semicond. Sci. Technol. s317(1993).
13. M.H. Weiler, R.L. Aggarwal, and B. Lax, Phys. Rev. **B17**, 3269(1978).
14. T. Ipposhi, K. Takita and K Masada, J. Phys. Soc. Japan, **57** 1013(1988).
15. C.L. Littler, To be published in *Proceedings of SPIE*, 1993.
16. D.G. Seiler, K.H. Littler, and C.L. Littler, Semicond. Sci. Technol. **1**, 383(1986).

17. R.E. Halsted, in *Physics and Chemistry of II-VI compounds*, edit by M. Aven and J.S. Prener (Wiley, New York, 1967), p. 385.
18. E.W. Williams and H. Barry Bebb, in *Semiconductor and Semimetals*, edited by R.K. Willardson and A. Beer (Academic, New York, 1972), Vol. 8, p. 321.
19. A.Z. Grasyuk, I.G. Zubarev, A.B. Mironov, and I.A. Poluéktov, *Sov. Phys. Semicond.*, Vol. 10, 159(159).
20. W. Scott, E.L. Stelzer, and R.J. Hager, *J. Appl. Phys.* **47**, 1408(1976).
21. I.T. Yoon, "*Anisotropy of Conduction Electrons in n-InSb and Extrinsic and Intrinsic Properties of HgCdTe*", Thesis, University of North Texas, August, 1991.

Figure 5.1 Wavelength dependence of both OPMA and RII spectra obtained from an $x \approx 0.24$ sample at 5.0K. The RII resonances are those between 1.5T and 3.0T, and do not shift with laser wavelength. The two peaks that appear at higher magnetic fields are due to OPMA and impurity-to-band magneto-optical transitions and are seen to shift with laser wavelength.



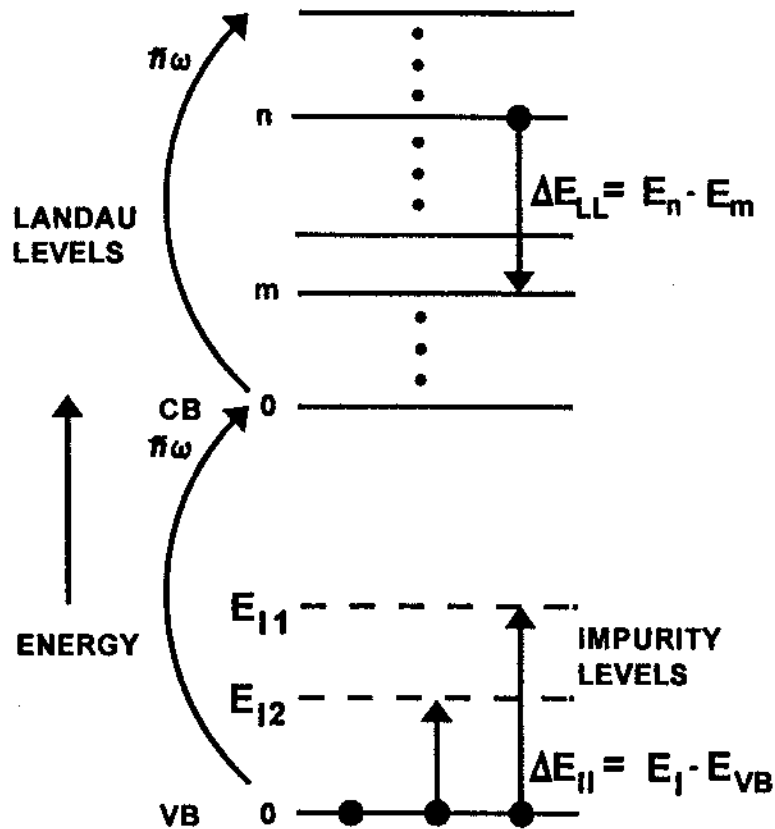


Figure 5.2 Schematic diagram of the electronic transitions that lead to the observed resonances. ΔE_{LL} is the energy difference between the initial and final conduction-band Landau levels, and ΔE_{II} is the difference between the energy of the trap level and the highest-lying valence-band Landau level. RII resonances occur when $\Delta E_{LL} = \Delta E_{II}$.

Figure 5.3 Photoconductive response versus magnetic field of the spectra obtained at 5.0K from control (A) and interstitially "doped" (B) samples with $x \approx 0.22$. Note that only OPMA is seen in the control sample, and only RII is seen in the "doped" sample.

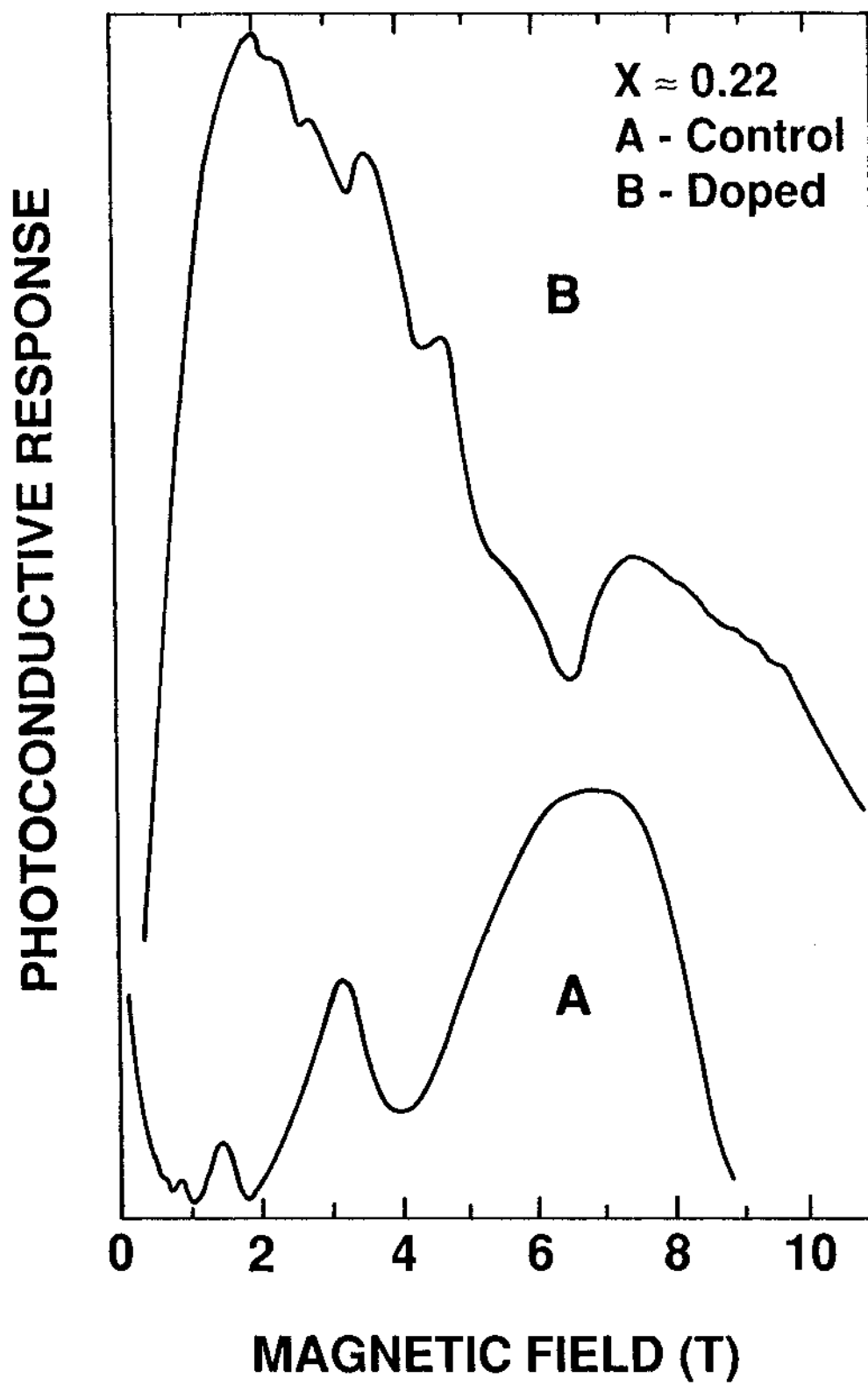


Figure 5.4 Wavelength dependence of the OPMA photoconductive response of the $x \approx 0.22$ control sample. The broad peaks in the higher field region for all the spectra are due to the bound excitons.

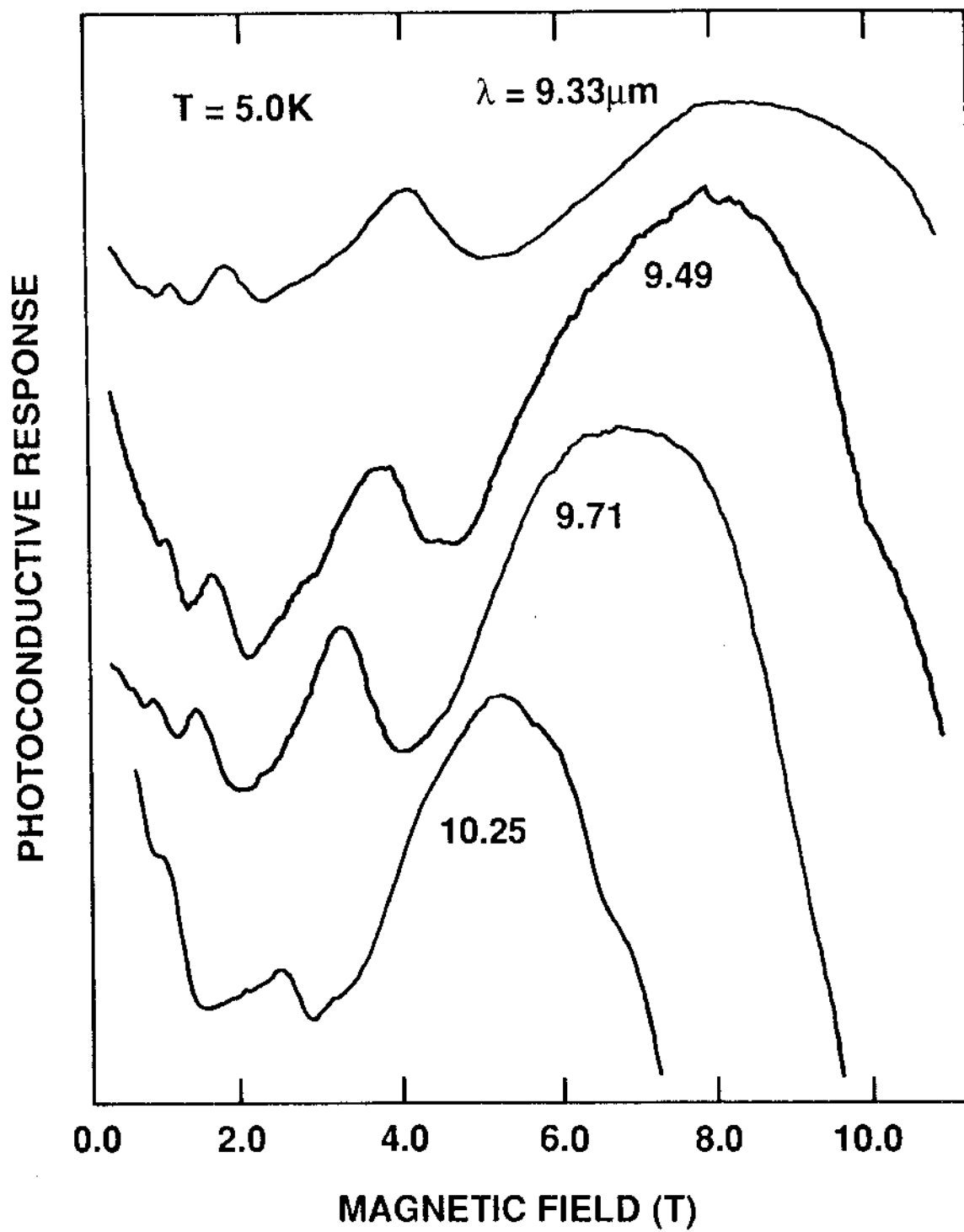


Figure 5.5 Fan chart of transition energies for the $x \approx 0.22$ control bulk sample. The solid dots represent the magnetic-field positions of OPMA, and the solid lines the calculated OPMA transition energies. The open squares represent the observed bound-exciton transition energies.

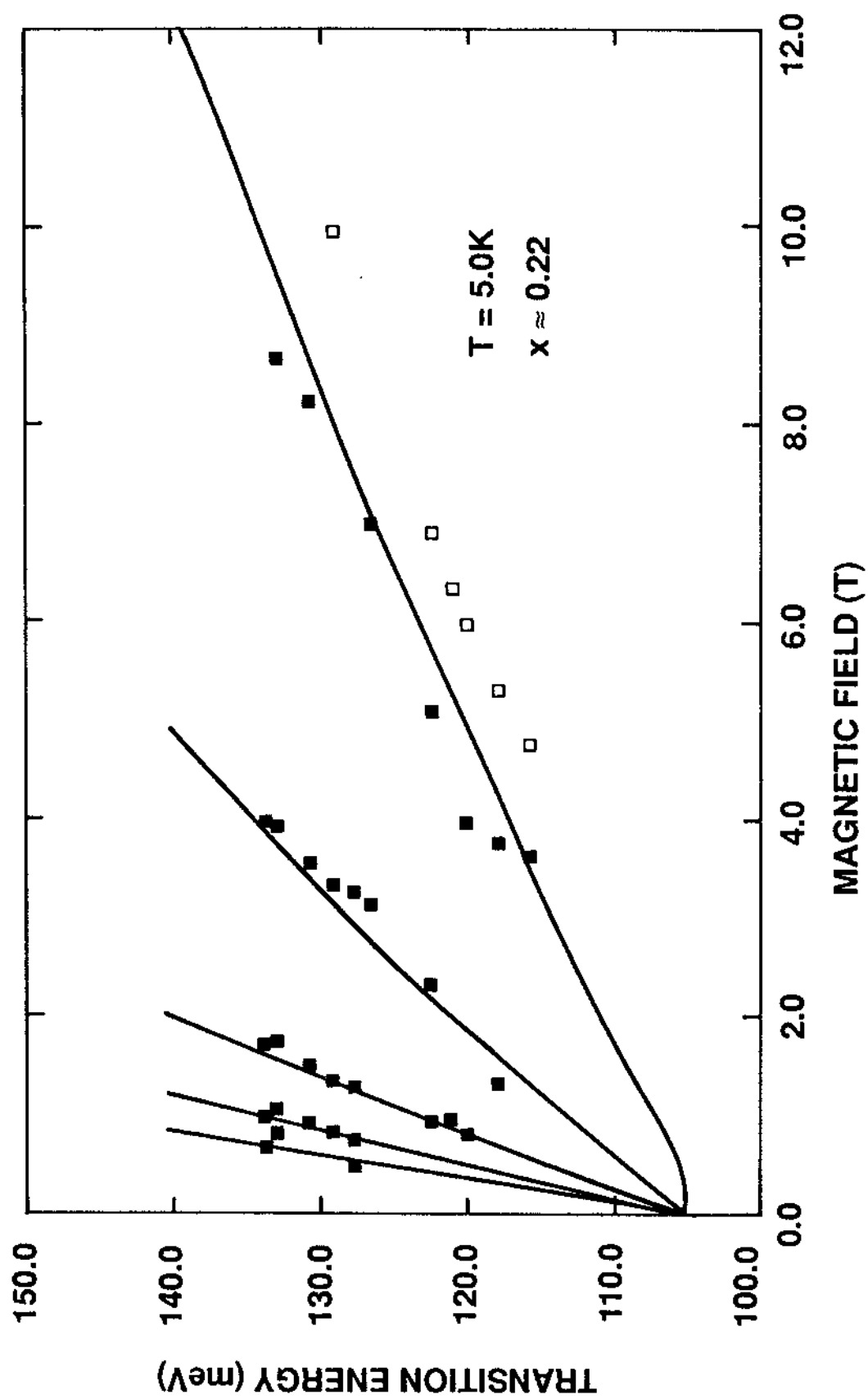


Figure 5.6 Comparison of RII spectra of control (A) sample and "doped" (B) sample with x value around 0.24. The control sample is a bulk sample which contains a residual concentration of Hg interstitials; the doped sample which was obtained by introducing more Hg interstitials into a piece of the control sample via an oxide bake.

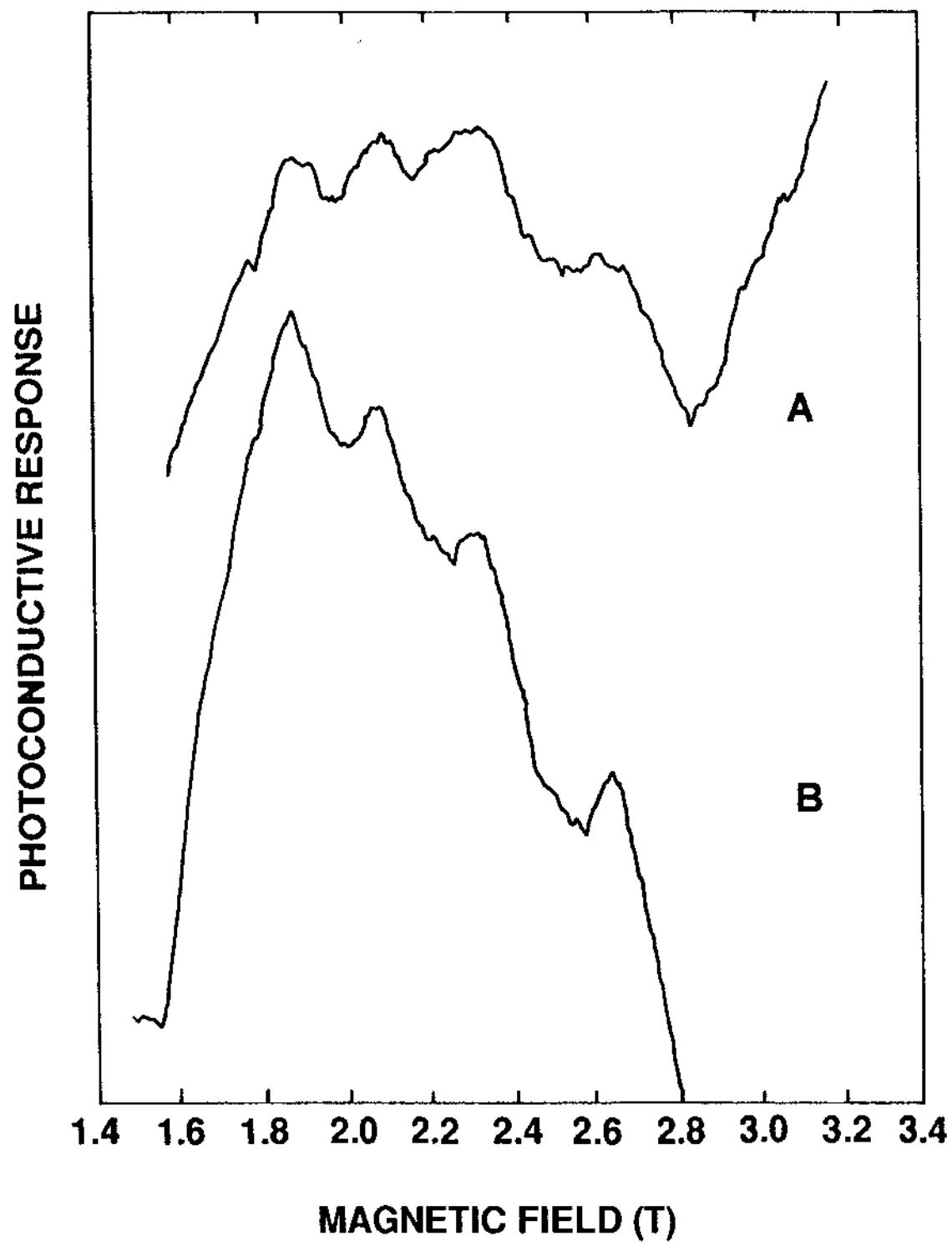


Figure 5.7 The same comparison of control (A) and "doped" (B) RII spectra as that of Figure 5.6, but the monotonic background of each spectrum has been removed for better comparison of the transition amplitudes. Clearly the transition amplitudes of the RII resonances from the "doped" sample are two to three times larger than those from the control sample.

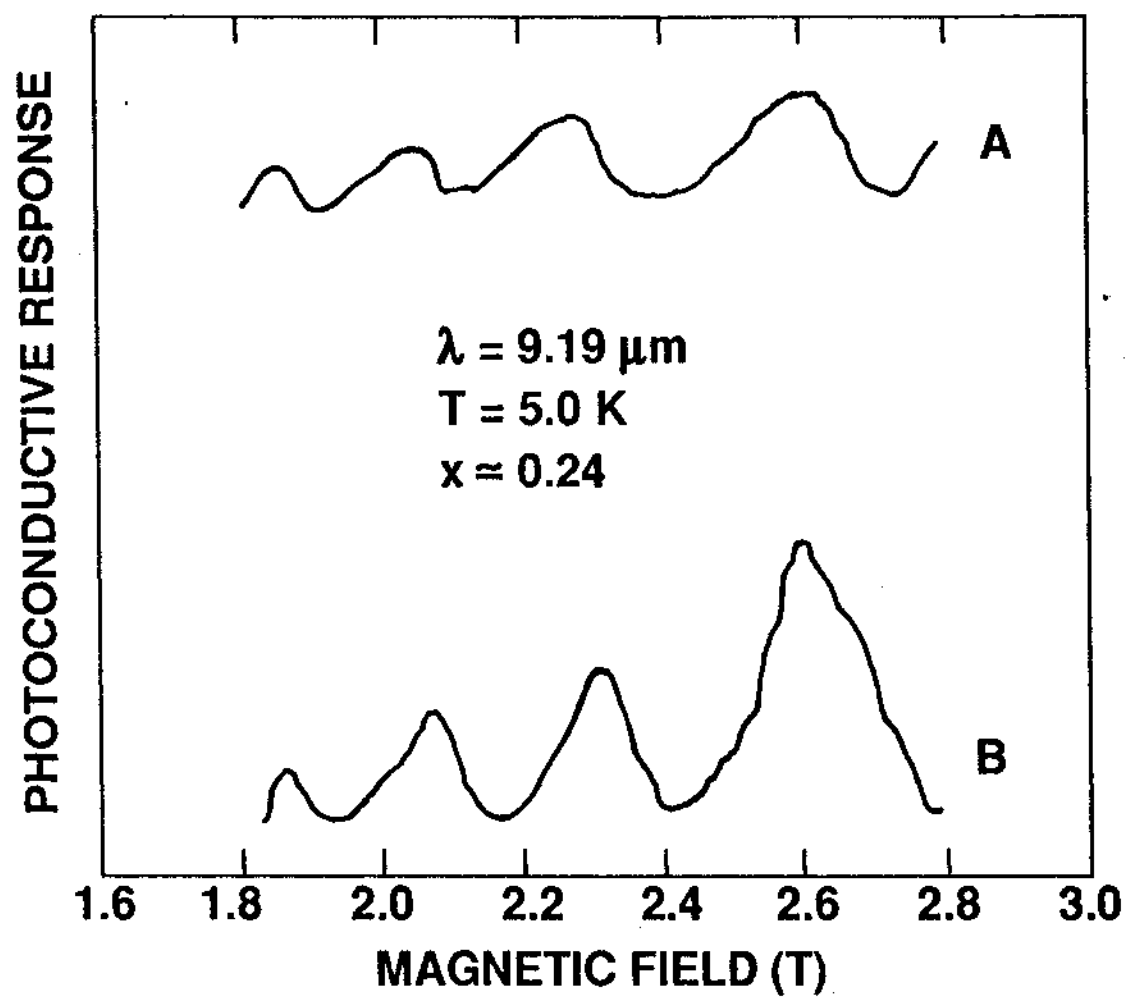
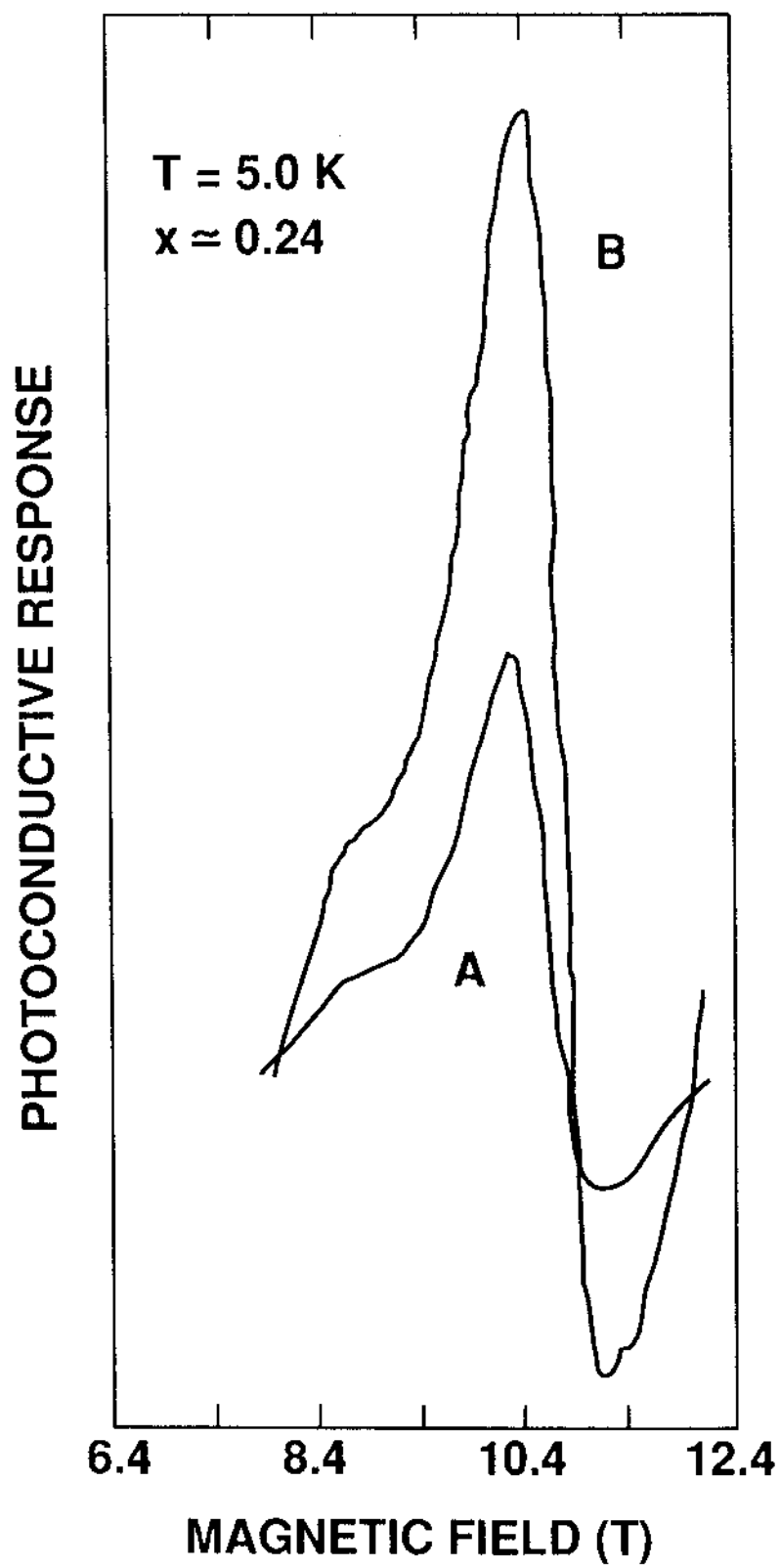


Figure 5.8 Comparison of TPMA resonances at $\lambda = 10.32\mu\text{m}$ and 5.0K from the control (A) and "doped" (B) samples, which are the same samples as discussed in Fig. 5.6 and Fig. 5.7. The TPMA transition corresponding to the observed resonance is $b^*(-1) \rightarrow b^c(1)$. The TPMA transition amplitudes from the "doped" samples are seen to be two to three times larger than those from the control sample.



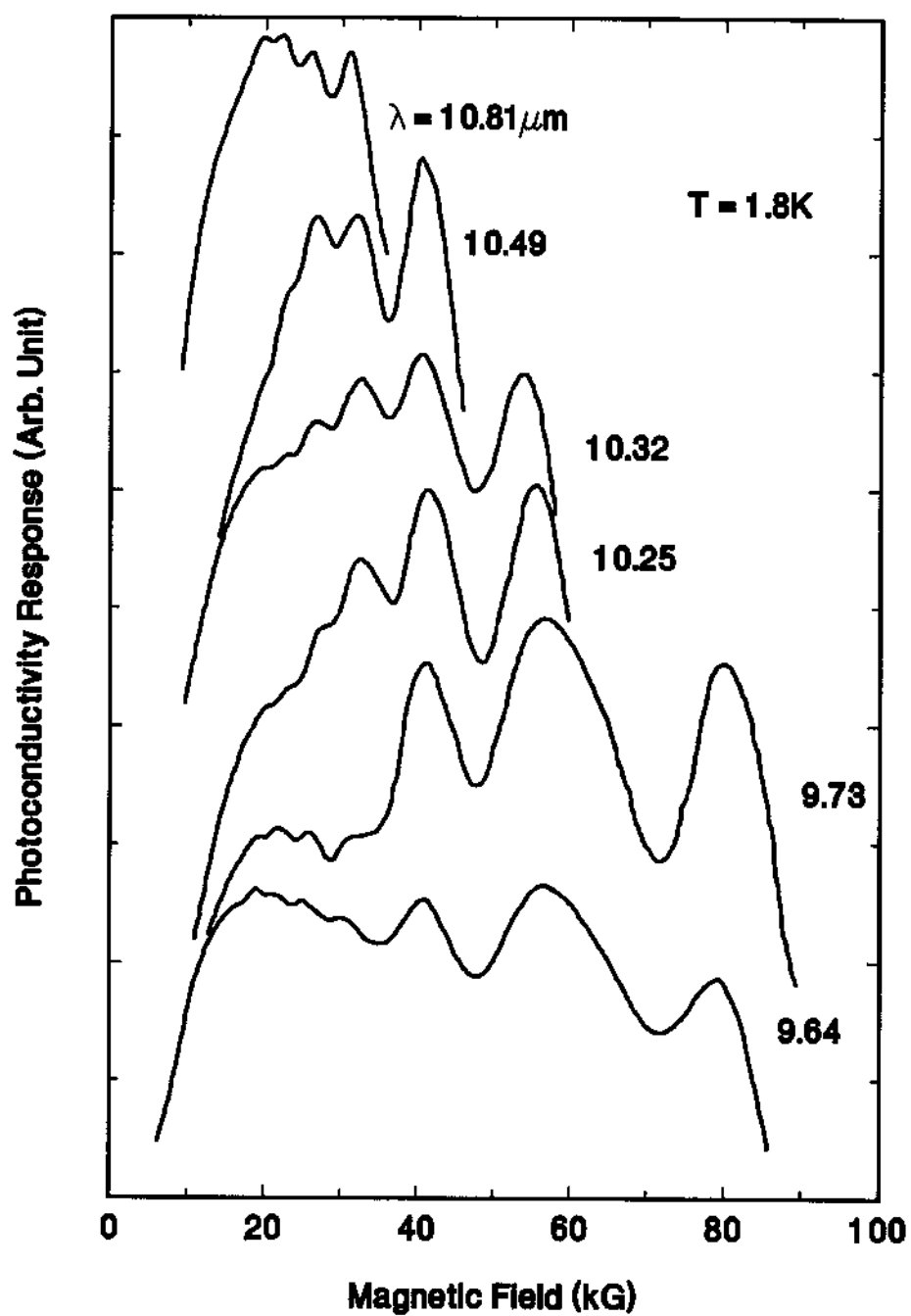


Figure 5.9 Wavelength dependence of RII spectra for a $x \approx 0.22$ LPE sample. The wavelength is from $9.64\mu\text{m}$ to $10.81\mu\text{m}$.

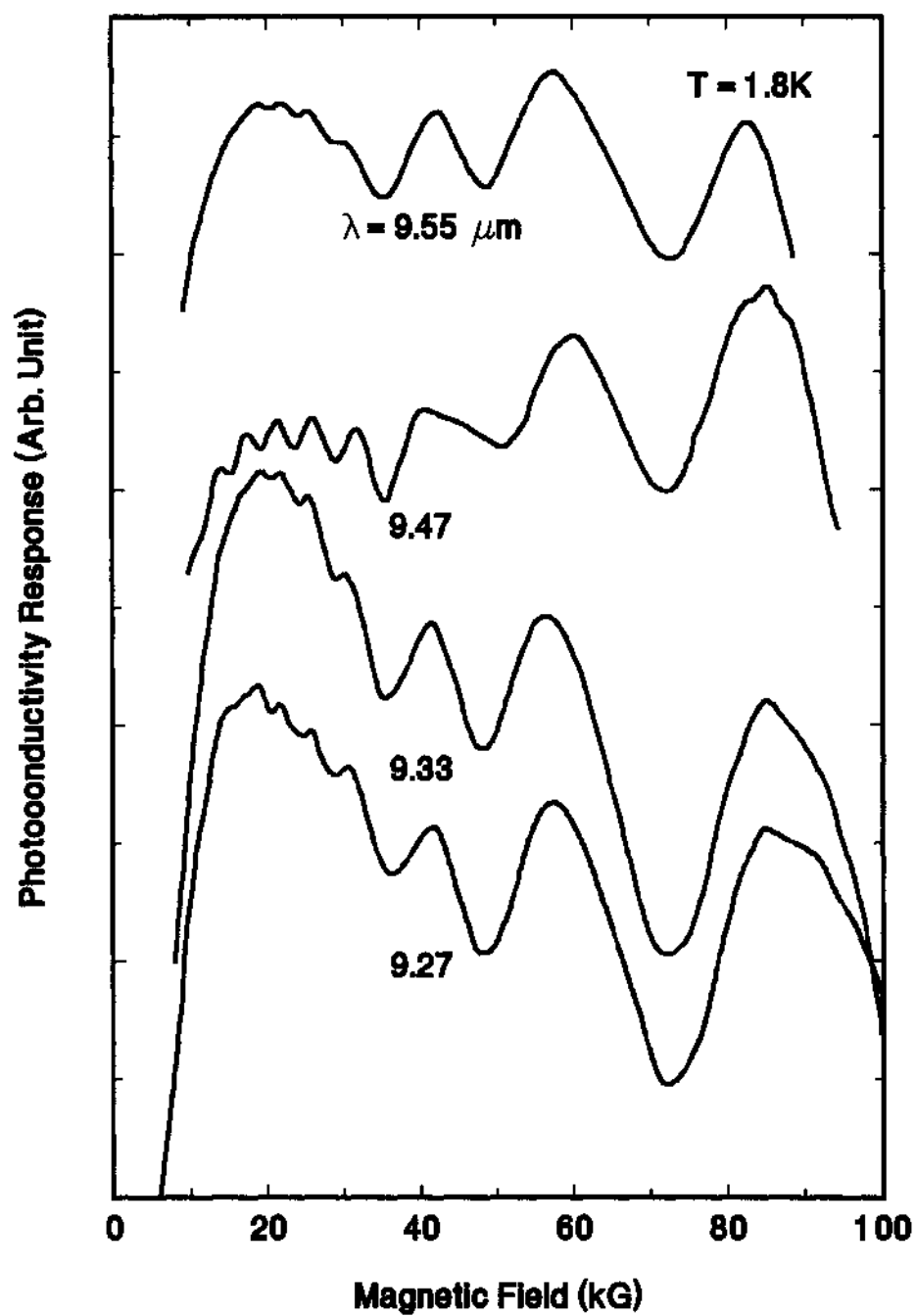


Figure 5.10 Wavelength dependence of RII spectra for a $x \approx 0.22$ LPE sample. The wavelength is from $9.27\mu\text{m}$ to $9.55\mu\text{m}$.

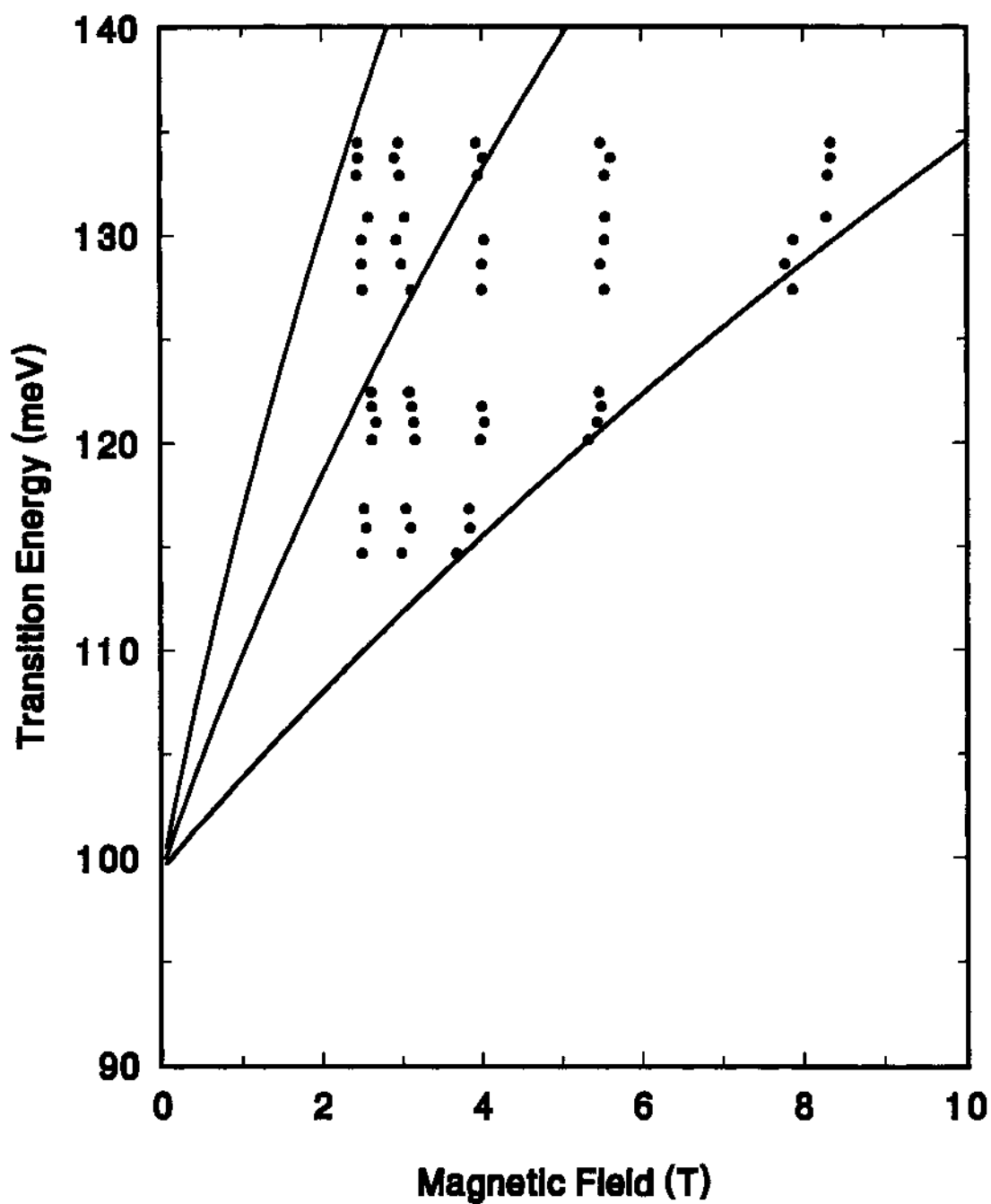


Figure 5.11 Fan chart of transition energies of OPMA for the $x \approx 0.22$ of $\text{Hg}_{1-x}\text{Cd}_x\text{Te}$ (lines) and magnetic field positions of resonance peaks from the magneto-optical spectra (solid dots).

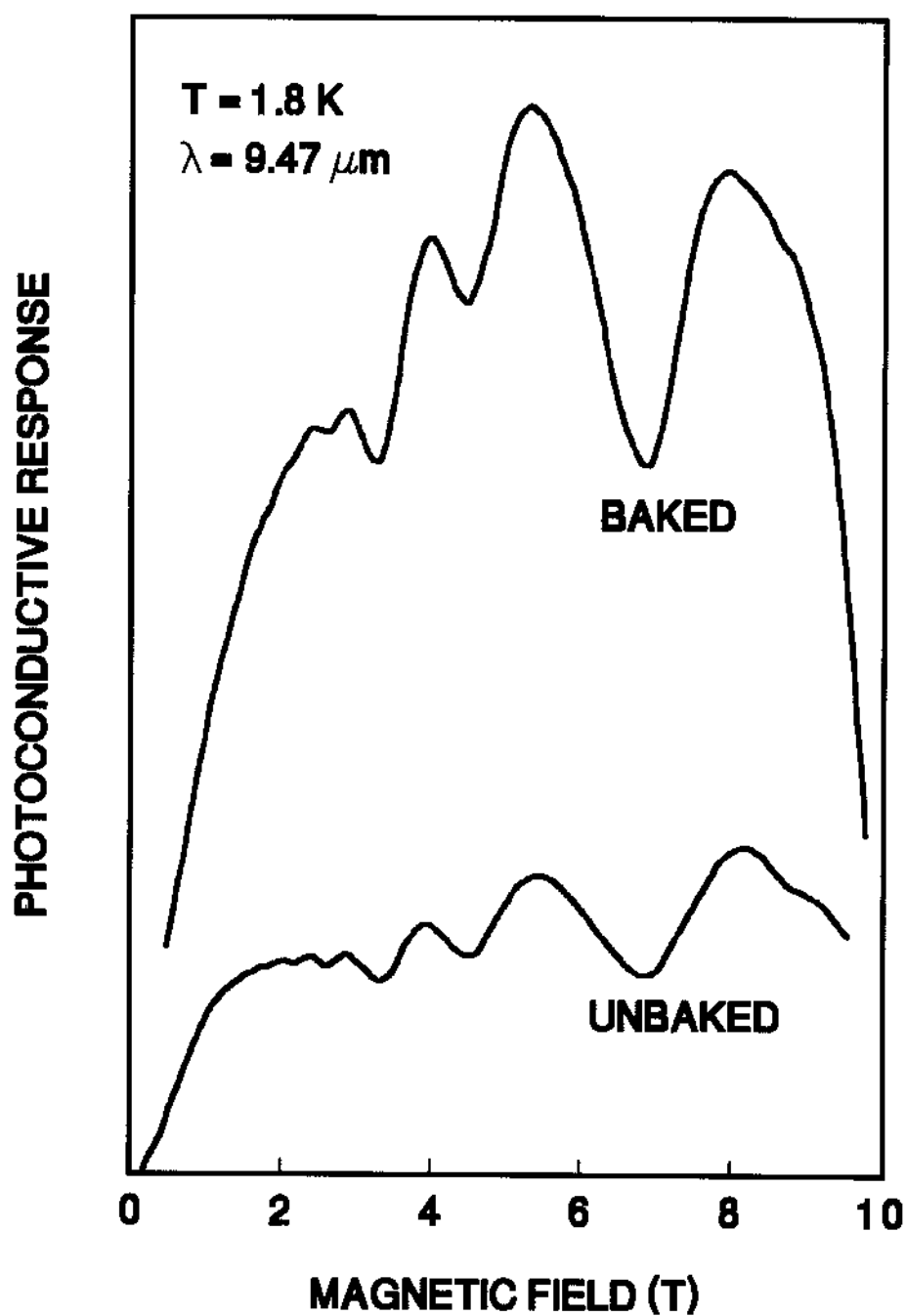


Figure 5.12 Comparison of RII spectra before and after the 140 °C bake for the $x \approx 0.22$ LPE sample passivated with an oxide layer.

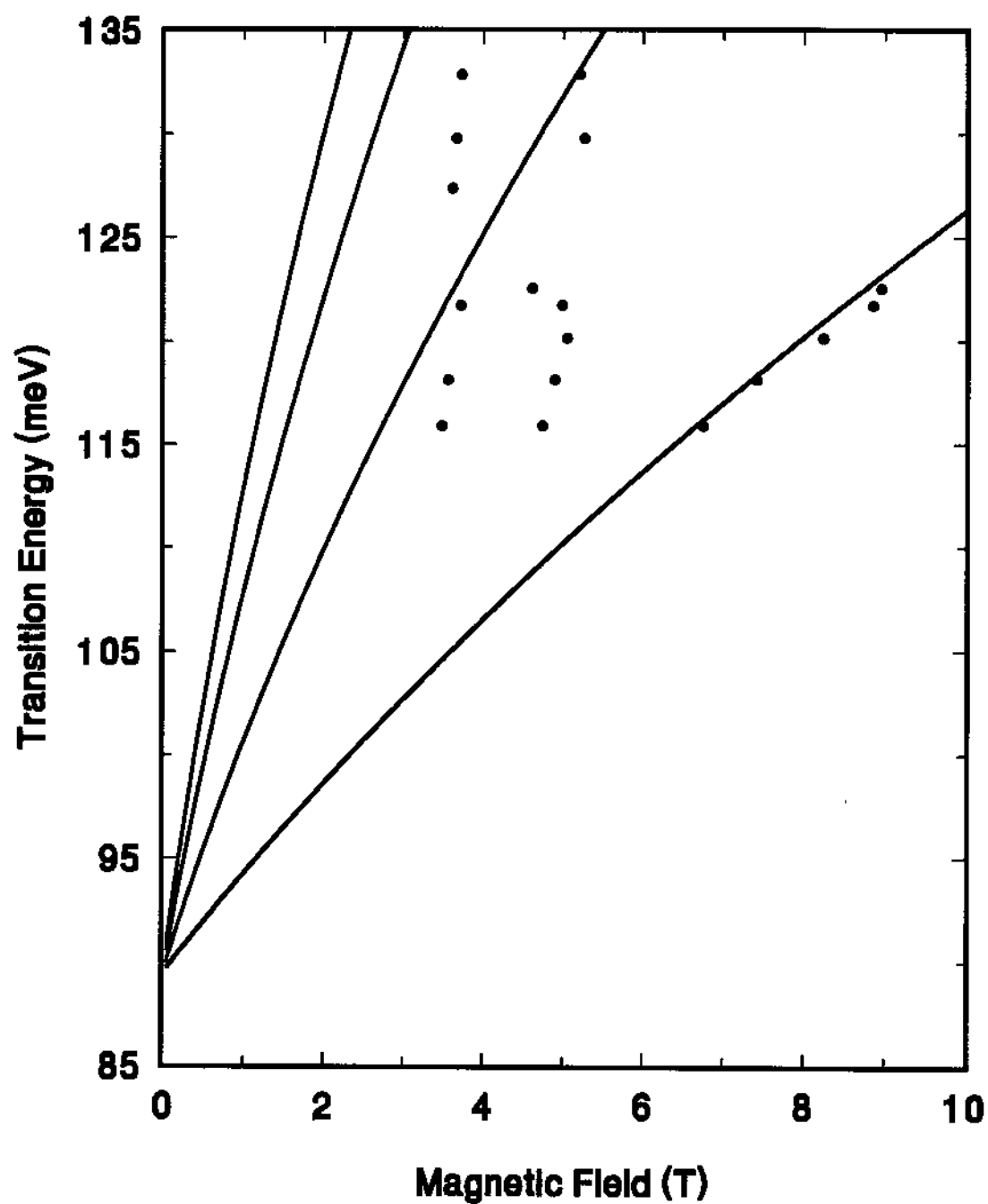


Figure 5.13 Transition energies of OPMA for the $x \approx 0.22$ of $\text{Hg}_{1-x}\text{Cd}_x\text{Te}$ (lines) and magnetic field positions of resonance peaks from the magneto-optical spectra (solid dots) for the unbaked $x \approx 0.22$ LPE sample passivated with ZnS.

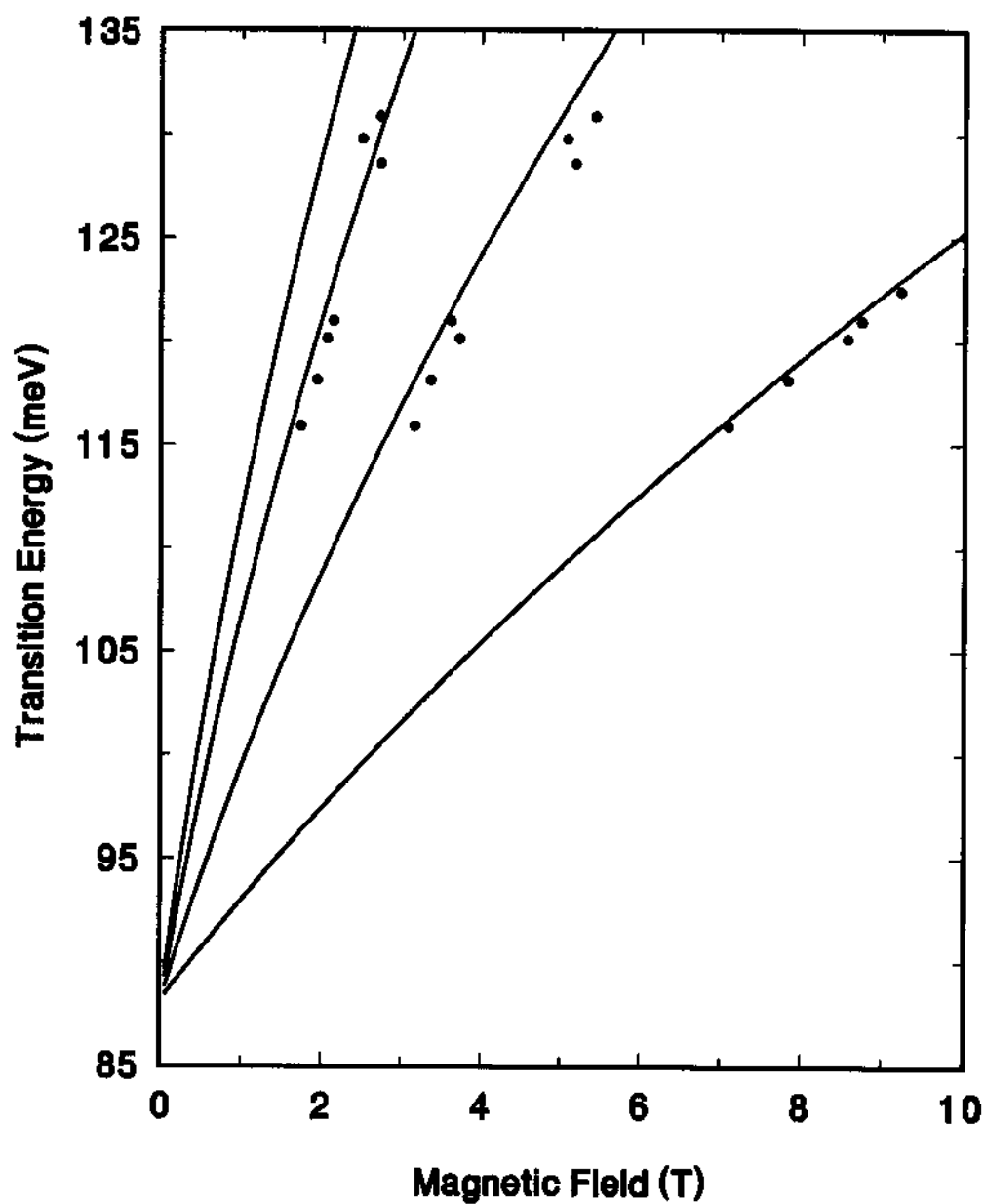


Figure 5.14 Transition energies of OPMA for the $x \approx 0.22$ of $\text{Hg}_{1-x}\text{Cd}_x\text{Te}$ (lines) and magnetic field positions of resonance peaks from the magneto-optical spectra (solid dots) for the $x \approx 0.22$ LPE sample passivated with ZnS after 220°C bake.

Figure 5.15 Wavelength dependence of the OPMA photoconductive response of the LPE $x \approx 0.23$ sample. The two peaks seen corresponding to the OPMA transitions $K_1(a^+(-1) \rightarrow a^c(1))$ and $K_2(b^+(-1) \rightarrow b^c(1))$. The energy gap is around 111meV.

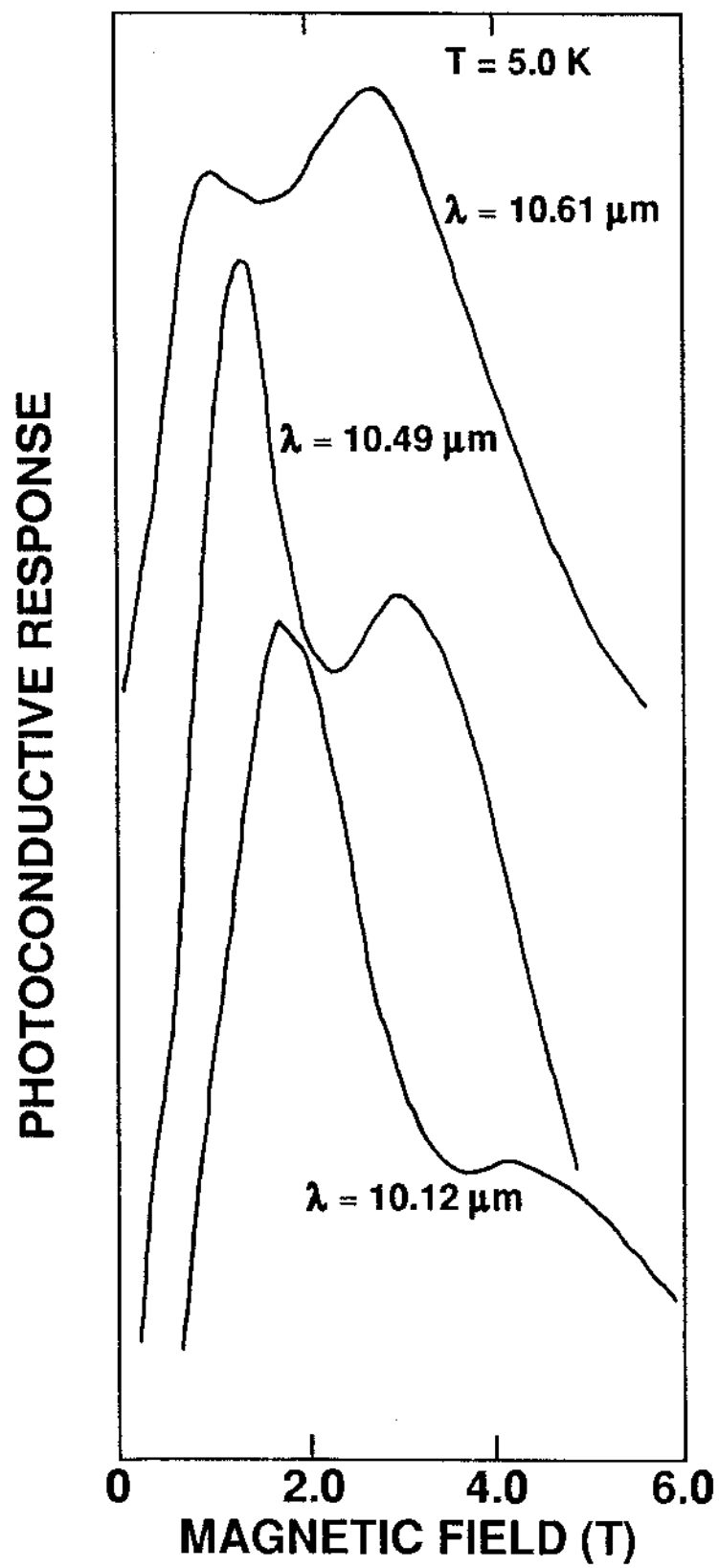


Figure 5.16 Fan chart of transition energies from the OPMA fit with the resonance peak positions for a $x \approx 0.23$ LPE sample. Two distinct energy gaps are determined from this fit of theory (lines) to experimental data (solid dots): $E_g \approx 111\text{meV}$ and $E_g \approx 120\text{meV}$. The spectra are shown in Fig. 5.15.

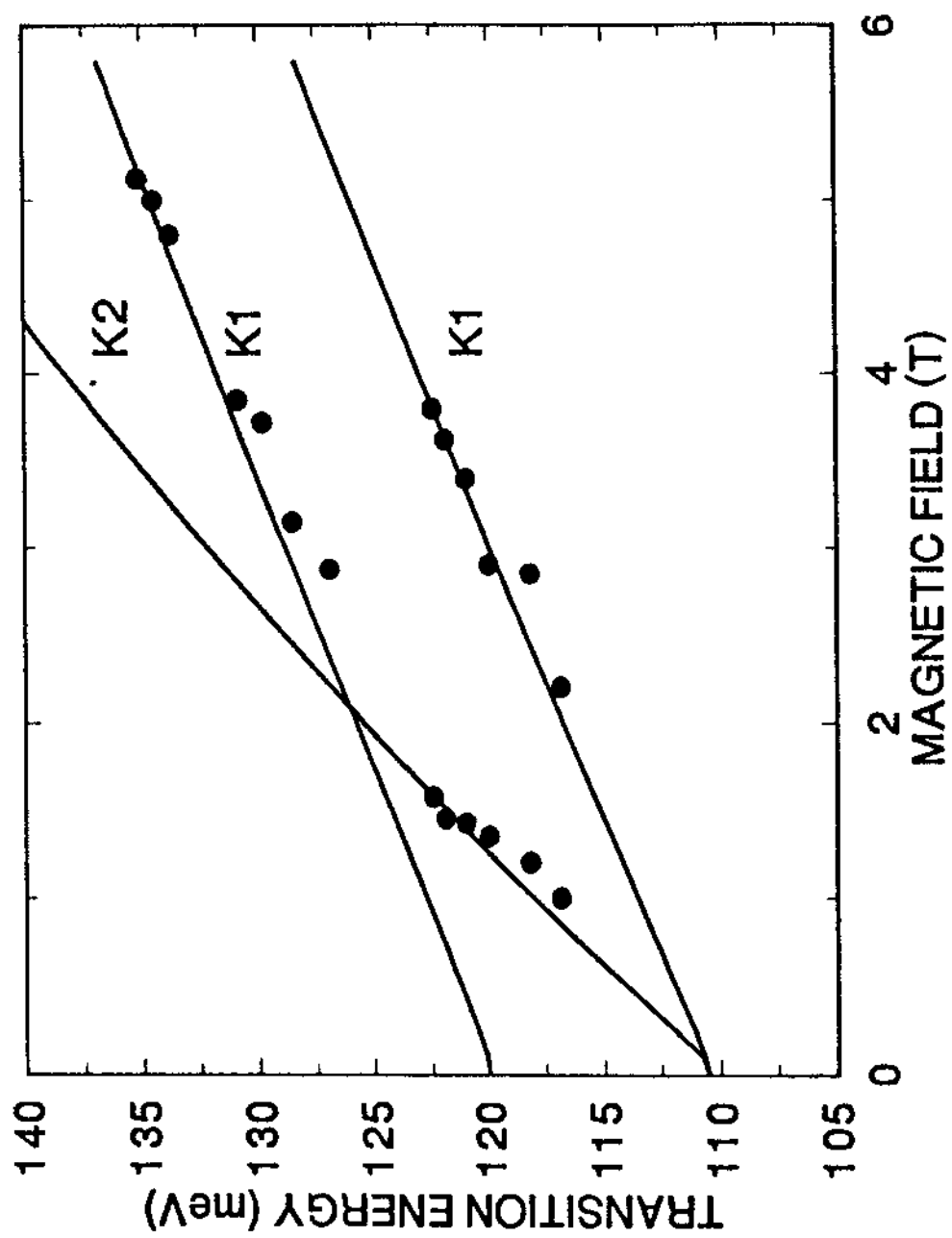
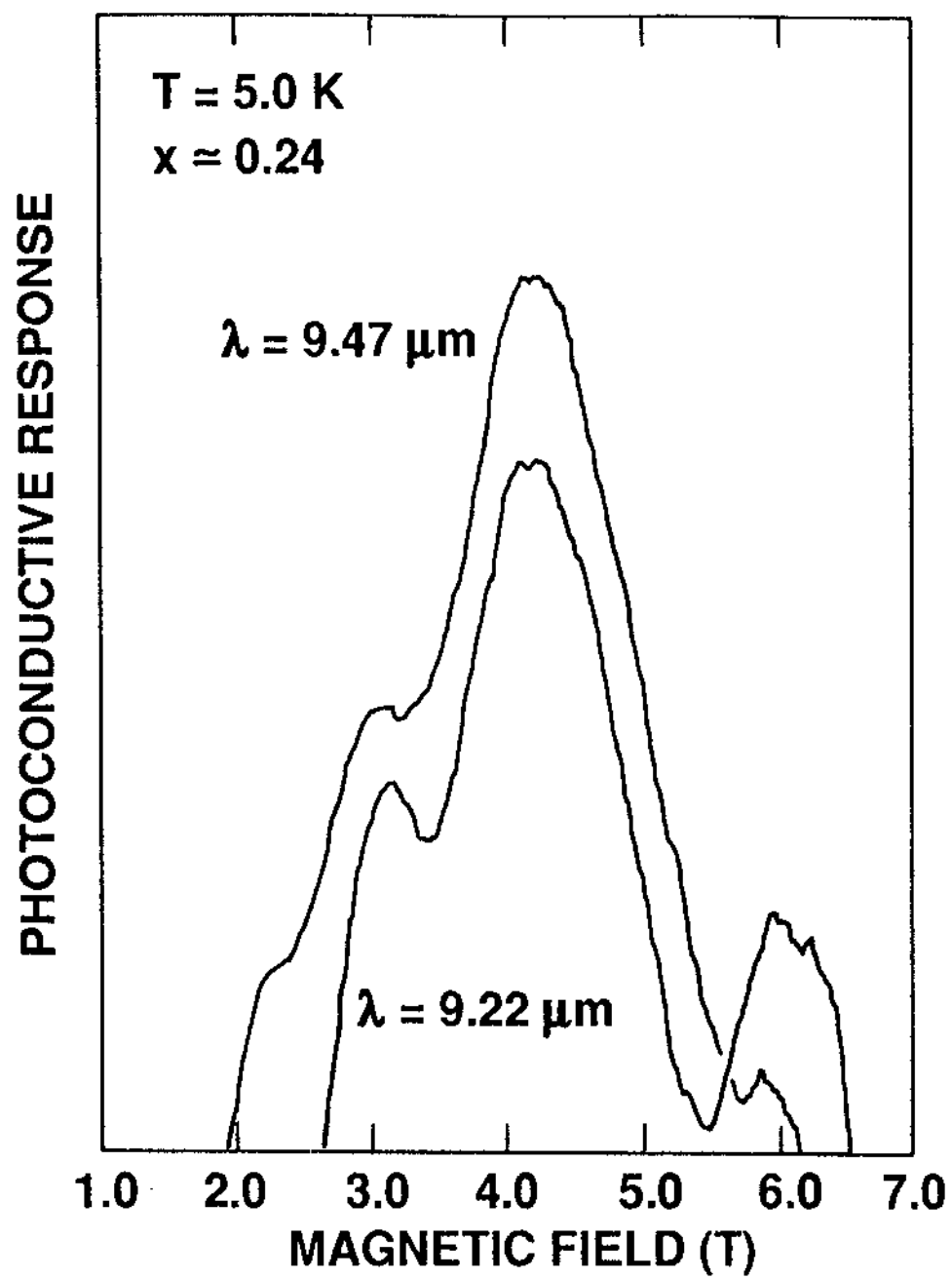


Figure 5.17 Wavelength dependence of RII spectra obtained from an $x \approx 0.24$ LPE sample.



CHAPTER 6

CONCLUSIONS

The nonlinear dynamics of driven diode resonator systems has been investigated. A varieties of interesting features have been observed: period doubling route to chaos, band merging, windows of period 3 and period 5, hysteresis, quasiperiodic states, periodic locking states, and Hopf bifurcation to chaos. The last three features are found only in line-coupled diode resonator systems.

The model for the single diode resonator system derived from *SPICE* program can simulate the dynamics very well, as illustrated by good agreement for the experimental observables: wave form, phase portrait, power spectra, bifurcation diagram. In addition, the Lyapunov exponents calculated from the experimental time series agrees very well with that obtained from the *SPICE* model.

For the line-coupled diode resonator system, experiments show that it can follow a quasiperiodic route to chaos. More specifically, the transitions to chaos for these systems agree with Curry-Yorke model very well, that is: periodic states $P \rightarrow$ quasiperiodic states with two frequencies $T^2 \rightarrow$ periodic locking states $L \rightarrow$ chaos. The simulation model for line-coupled system derived from *SPICE* gives consistent results. In addition, Lyapunov exponents calculated from both experimental time series and the simulated system are in good agreement for both quasiperiodic regimes and chaotic regimes.

OGY's stabilization technique is employed to control the chaos in both single and line-coupled diode resonator systems. For the single diode system, periodic orbits up to period 17 can be obtained from a typical chaotic attractor. As for line-coupled diode resonator systems, the stabilization can not only yields high periodic orbits very easily, but also produce quasiperiodic orbits. This is the first time that quasiperiodic states have been stabilized. This phenomenon has raised a serious question: Does there exist any unstable quasiperiodic orbits in addition to the well-known unstable periodic orbits in a chaotic attractor? On the other hand, the experimental techniques and results obtained have directly assisted the investigation of the stabilization of laser systems, which will certainly have practical applications.

The synchronization of chaos is obtained by weakly coupling two coupled tunnel diode relaxation oscillators. In addition, the frequency-locked entrainment states of two chaotic attractor are found by appropriate couplings. This clearly is a interesting phenomenon falling in between synchronization with strong coupling and nonsynchronization with weak coupling. As pointed by Ditto and Pecora (1993), the synchronization of chaos may well be applied for the construction of secure private communication systems. The further investigation on the synchronization of chaos in the coupled tunnel diode relaxation oscillators clearly will help to explore this possibility.

The electrical oscillations in n-InSb under transverse magnetic field at low temperature are further investigated. The experimental results are consistent with Hüpper and Schöll's theory in that there exists a boundary in the two parameter (Magnetic field B versus Current density j) phase space. This boundary separates oscillatory instability region from static region. By changing magnetic

field B at a fixed current density j , the system will yield a period doubling cascade to chaos. Lyapunov exponents were calculated and found to be consistent with the observed phenomena. The stability of chaotic attractor in this system was studied against AC-driven source, and the result show that this stability is similar to that in a simple driven oscillator. In addition, the induced transitions from chaos to periodicity by AC-driving source agrees well with the conjectured scaling law for chaotic systems.

Finally, RII spectroscopy has been used to investigate impurity and defect (trap) levels that presumably are caused by Hg interstitials in both bulk and LPE crystals of $\text{Hg}_{1-x}\text{Cd}_x\text{Te}$ with x values of ≈ 0.22 to ≈ 0.24 . For the bulk samples, deliberately introductions of Hg interstitials have provide direct evidence for the formation of trap levels near 45 and 60meV above the valence band edge. The 60meV level in the $x \approx 0.24$ ($E_g = 121\text{meV}$ at 5K) sample is seen to enhance the transition strength of resonant TPMA observed at high fields by acting as a near-resonant intermediate state for the two-photon transition process, which further supports the formation of deep trap levels by Hg interstitials. LPE samples with different processing conditions have been investigated by RII spectroscopy. Like the bulk samples, the Hg interstitials are found to form trap levels near 40meV, 45meV, and 59meV. The RII spectroscopy clearly is a very sensitive technique to investigate deep energy levels caused by Hg interstitials in $\text{Hg}_{1-x}\text{Cd}_x\text{Te}$. This technique is generally applicable to the investigation of other defects and impurities in HgCdTe as long as the trap levels created are accessible via RII mechanism.

BIBLIOGRAPHY

- Abraham R. H. and Shaw C. D. *Dynamics - The Geometry of Behavior, Part 1: periodic Behavior*, Chapter 4. (Aerial Press, Inc., 1982).
- Ahlers G. and Behringer R. Phys. rev. Lett. **40**, 712(1978).
- Albert G.L. *Thesis*, University of North Texas, Chapter 4, 1993
- Antognetti P. and Massobrio G. *Semiconductor Device Modelling with SPICE*. (McGraw-Hill, New York, 1988).
- Aoki K., Ikezawa O., Mugibayashi N., and Yamamoto K. Physica 134B, 288 (1985).
- Aoki K., Kawase Y., Yamamoto K., and Mugibayashi N. J. Phys. Soc. Jpn. 59, 20(1990).
- Arecchi F.T., Giacomelli G., Lapucci A. and Meucci R. Phys. Rev. **A49**, 4997(1991).
- Arecchi F.T. and Harison R.G. *Instabilities and Chaos in Quantum Optics*, Vol. 34 of Springer Series in Synergetics, (Springer-Verlag, Berlin, 1987).
- Bahir G. and Finkman E. J. Vac. Sci. Technol. **A 7**, 348(1989).
- Benettin G., Galgani L., Giorgilli A. and Strelcyn J.-M. Meccania **15** 9(1980).
- Bergé P., Dubois M., Manneville P. and Pomeau Y. J. Phys. Lett. **41**, L341(1980).
- Bergé P., Pomeau Y., and Vidal C. *Order within Chaos: Towards a deterministic approach to turbulence*. (John Wiley & Sons 1984).
- Bielawski S., Derozier D. and Glorieux P. Phys. Rev. **A47**, 2492(1993).

- Broomhead D.S. and King G.P. *Physica* **D20** 217(1986).
- Buskirk R. and Jefferies C. *Phys. Rev. A* **31**, 3332(1985)
- Bryant P. and Brown R. *Phys. Rev. Lett.* **65**, 1523(1990).
- Curry J. and Yorke J.A., "A transition from Hopf bifurcation to chaos: computer experiments with map in \mathbf{R}_2 " in *The Structure of attractors in dynamical systems, Springer Notes in Mathematics*, **668**, p. 48, Springer-Verlag (1977).
- Ditto W.L. and Pecora L.M., *Scientific American*, 78, August, 1993.
- Ditto W.L., Rauseo S.N. and Spano M.L., *Phys. Rev. Lett.* **65**, 3211 (1990).
- Eckmann J.-P., Kamphorst S.O., Ruelle D. and Ciliberto S., *Phys. Rev. A* **34**, 4971(1986).
- Elkind J.L., *J. Vac. Sci. Technol. B***10**, 1460(1992).
- Farmer J.D., Ott E. and Yorke J.A., "The Dimension of Chaotic Attractors," *Physica* **7D**(1983)153.
- Fitzhugh R., *Mathematical Models of Excitation and propagation in Nerve*, in *Biological Engineering*, eds H.P. Schwan, (McGraw-Hill, New York, 1968).
- Fraser A.M., *Physica* **D34** 391(1989).
- Giglio M., Musazzi S. and Perini U., *Phys. Rev. Lett.* **47**, 243(1981).
- Gollub J.P., Romer E.J. and Socolar J.E., *J. Stat. Phys.* **23**, 321(1980).
- Gollub J.P. and Benson S.V., *J. Fluid. Mech.* **100**, 449(1980).
- Grebogi C., Ott E. and Yorke J., *Phys. rev. A* **37**. 1711(1988).
- Grasyuk A.Z., Zubarev I.G., Mironov A.B. and Poluéktov I.A., *Sov. Phys. Semicond.*, Vol. **10**, 159(1975).
- Gunarante G.H., Linsay P.S. and Vinson M.J., *Phys. Rev. Lett.* **63** 1(1989).

- Halsted R.E., in *Physics and Chemistry of II-VI compounds*, edit by M. Aven and J.S. Prener (Wiley, New York, 1967), p. 385.
- Hudson J.L., Hart M. and Marinko D., J. Chem. Phys. **71**, 1601(1979).
- Hunt E.R., Phys. Rev. Lett. **49**, 1054(1982).
- Hunt E.R., Phys. Rev. Lett. **67**, 1953 (1991).
- Hunter A.T., Smith D.L., and McGill T.C., Appl. Phys. Lett. **37**, 200(1980).
- Hüpper G. and Schöll E., Phys. Rev. Lett. **66**, 2372(1991).
- Ipposhi T., Takita K. and Masada K., J. Phys. Soc. Japan, **57** 1013(1988).
- Jones C.E., Nair V., and Polla D.L., Appl. Phys. Lett. **39**, 248(1981).
- Kahaner D., Moler C. and Nash S., *Numerical Methods and Software*, Chap. 8, (Prentice Hall, 1989).
- Kalhert H. and Seiler D.G., Rev. Sci. Instruments **48**, 1017(1977).
- Kaneko K., Phys. Rev. Lett. **63**, 219(1989); **65**, 1391(1990); Physica **D41**, 139(1990).
- Kaplan J. and Yorke J., "Chaotic behavior of multi-dimension difference equations." in: Functional Differential Equations and the Approximation of Fixed Points. *Lecture Notes in Mathematics*, Vol. 730. H.O. Peitgen and H.O. Walther. eds. (Springer, Berlin). p. 228
- Knap W., Jezewski M., Lusakowski J. and Kuszko W., Solid-State Electron **31**, 813(1988).
- Kowalski J.M., Albert G.L. and Gross G.W., Phys. Rev. **A42**, 6260(1990).
- Kowalski J.M., Albert G.L., Roades B.K. and Gross G.W., Neural Networks **5**, 805(1992).
- Kruel Th.-M., Eiswirth M. and Schneider F.W., Physica **63D**, 117(1993).

- Kuznetsov Yu. I., Landa P. S., Olhovoi A. F. and Perminov S. M., *Pokl. Akad. N. USSR*, 291 (1955) [in Russian].
- Lang D.V. and Logan R.A., *J. Electron Mater.* **4**, 1053(1975)
- Libchaber A. and Maurer J., *J. Phys. Lett. (Paris)* **39**, L369(1978).
- Littler C.L., To be published in *Proceedings of SPIE*, 1993.
- Littler C.L., Song X.N., Yu Z., Elkind J.L., Seiler D.G., and Lowney J.R., *J. Vac. Sci. Technol.* **B10**, 1466(1992).
- Littler C.L., Song X.N., Yu Z., Elkind J.L., Lowney J.R., *Semicond. Technol.* **8**, s317(1993).
- Linsay P.S., *Phys. Rev. Lett.* **47**, 1349(1981).
- Landa P.S. and Rosenblum M.G., *Physica* **48D** 232(1991).
- Miller G.L., Lang D.V., and Kimerling K.C., *Ann. Rev. Mater. Sci.* 377-448(1977).
- Maracas G.N., Porod W., Jonson D.A., and Ferry D.K., *Physica* **134B**, 276 (1985).
- Miller, G.L., Lang, D.V. and Kimerling, L.C. *Ann. Rev. Mater. Sci.* 377-448(1977).
- Moore B.T., Seiler D.G., and Kahlert H., *Solid State Elec.* **21**, 247(1978).
- Newhouse S., Ruelle D. and Takens T., "Occurrence of strange axiom-A attractors near quasiperiodic flows on T^m , $m \geq 3$ ", *Communications in Mathematical Physics*, **64**, p.35(1978).
- J. Opt. Soc. Am. **B2**, No.1, (1985). Special Issue On the Instabilities in Optical Media
- Oseledec, V. I., *Trans. Moscow Math. Soc.* **19**, 197(1968).
- Ott, E. Grebogi, C. and Yorke, James, *Phys. Rev. Lett.* **64**. 1196 (1990).
- Peinke J., Muhlbach A., Rohricht B., Wessely B., Mannhart J., Parisi J., and Huebener R.P., *Physica* **23D**, 176(1986).

- Perez J.M., *"Chaotic Behavior of a Driven P-N Junction"* PhD Thesis, UC Berkeley.
- Perez J.M., Yu Z., Kowalski J.M., Albert G., Littler C.L. and Song X.N., "Synchronization of Chaos in Coupled Tunnel Diode Relaxation Oscillators", **Proceedings of the 1st Experimental Chaos Conference**, Arlington, VA, Oct. 1991 (*World Scientific, Singapore, 1992*).
- Peroca L.M., Carroll R.L., Phys. Rev. Lett. **64**, 821(1990).
- Phillips C. and Cornelius B., *Computational Numerical Methods*, (Ellis Horwood Limited, 1986) p.174
- Polla D.L. and Jones C.E., Solid State Commun. **36**, 809(1980)
- Polla D.L. and Jones C.E., J. Appl. Phys. **51**, 12(1980).
- Rashband S.N., *Chaotic Dynamics of Nonlinear Systems* (John Wiley, 1990).
- Rau U., Peinke J., Parisi J., Huebener R.P., and Schöll E., Phys. Lett. A124, 331(1987).
- Rohricht B., Wessely B., Peinke J., Muhlbach A., Parisi J., and Huebener R.P., Physica **134B**, 281(1985).
- Rollins R.W. and Hunt E.R., Phys. Rev. Lett. **49**, 1295(1982).
- Roux J.C., Rossi A., Bachelart S. and Vidal C., Physica, **2D**, 395(1981).
- Roy R., Murphy T.W.Jr., Maier T.D., Gills Z., and Hunt E.R., Phys. Rev. Lett. **68**, 1295(1992).
- Russel D.A., Hanson J.D., and Ott E., Phys. Rev. Lett. **45** (1980)1175.
- Sah C.T., Solid State Electron. **19**, 975(1977)
- Sano M. and Sawada Y., Phys. Rev. Lett. **55**, 1082(1985).
- Schöll E., *Nonequilibrium Phase Transitions in Semiconductors*, Springer Series in Synergetic, Vol. 35, Springer, Berlin, 1987.

- Schöll E., Parisi J., Rohricht B., Peinke J., and Huebener R.P., Phys. Lett. A119, 419(1987).
- Scott W., Stelzer and Hager R.J., J. Appl. Phys. **47**, 1408(1976)
- Seeger, *Semiconductor Physics* (Springer 1985).
- Seiler D.G., Littler K.H., and littler C.L., Semicond. Sci. Technol. **1**, 383(1986).
- Seiler D.G., Littler C.L., Justice R.J., and Milonni P.W., Phys. Lett. A108, 462(1985).
- Seiler D.G., Lowney J.R., Littler C.L., Yoon I.T., and Loloee M.R., J. Vac. Sci. Technol. **B9**, 1847(1991).
- Shaw R.. "Strange Attractors, Chaotic Behavior, and Information Flow." Z. Naturforsch. **36A**(1981)80.
- Shaw R., Andereck C.D., Reith L.A. and Swinney H.L., Phys. Rev. Lett. **48**, 1172(1982).
- Simoyi R.H., Wolf A.and Swenny H.L., Phys. Rev. Lett. **49**, 245(1982).
- Singer J., Wang Y-Z., and Bau H.H., Phys. Rev. Lett. **66**, 1123 (1991),
- Smith R.A., Semiconductors (Cambridge Univ. Press 1964), P. 129.
- Smith B.L., Hayes T.J., Peaker A.R., and Wright D.R., Appl. Phys. Lett. **26**, 122(1975).
- Song X.N., *"Magneto-Optical and Chaotic Electrical Properties of n-InSb"*, Thesis, University of North Texas, December, 1991.
- Song X.N., Seiler D.G., and Loloee M.R., Appl. Phys. **48**, 137(1989).
- Song X.N., Yu Z., Albert G.L., Kowalski J.M., Littler C.L. and Perez J.M., "Autonomous and Externally Driven Periodic and Chaotic Hall Voltage Oscillations in N-InSb", **Proceedings of the 1st Experimental Chaos Conference**, Arlington, VA, Oct. 1991 (World Scientific, Singapore, 1992).

- Su Z., Rollins R.W. and Hunt E.R., Phys. Rev. **A40**, 2698(1989).
- Swinney H.L. and Gallub J.P., Physics Today **31**, No.8, 41(August 1978).
- Takens F., "Detecting Strange Attractors in Turbulence." in: Lecture Notes in Mathematics No. 898, (Springer, Berlin, 1981) p. 366.
- Teitworth S.W., Westervelt R.M., Phys. Rev. Lett. **51**, 825(1983).
- Testa J., Perez J.M., Jefferies C., Phys. Rev. Lett. **48**, 714(1982).
- Testa J., Perez J.M., Jefferies C., Phys. Rev. Lett. **49**, 1055(1982).
- Vohra S., Spano M., Shlesinger M., Pecora L., and Ditto W., **Proceedings of the 1st Experimental Chaos Conference**, Arlington, VA, Oct. 1991.
- Proceedings of the 2nd Experimental Chaos Conference**, Arlington, VA, Oct. 1993.
- Weiler M.H., Aggarwal R.L., and Lax B., Phys. Rev. **B17**, 3269(1978).
- Williams E.W. and Bebb H.B., in *Semiconductor and Semimetals*, edited by Willardson R.K. and Beer A.C., (Academic, New York, 1972), Vol. 8.
- Wolf A., Swift J.B., Swinney H.L., and Vastano J.A., Physica **16D**, 285(1985).
- Yamada K., Takara N., Imada H., Miura N., and Hamaguchi C., Solid-State Electron **31**, 809 (1988).
- Yoon I.T. , "*Anisotropy of Conduction Electrons in n-InSb and Extrinsic and Intrinsic Properties of HgCdTe*", Thesis, University of North Texas, August, 1991.
- Yu Z., Steinshnider J., Littler C.L., Perez J.M., Kowalski J.M., Phys. Rev. **E 49**, 220(1994).